

Earth Explorer 10 Candidate Mission Harmony Report for Assessment



Reference	ESA-EOPSM-HARM-RP-3784
Issue/Revision	1.0
Date of Issue	13/11/2020
Status	Issued

ACKNOWLEDGEMENTS

This report is based on contributions from the Harmony Mission Advisory Group (MAG):

Juliet Biggs (COMET, University of Bristol, UK)

Bruno Buongiorno Nardelli (ISMAR-CNR, IT)

Bertrand Chapron (IFREMER, FR)

Andrew Hooper (COMET, University of Leeds, UK)

Andreas Kääb (University of Oslo, NO)

Paco López-Dekker (Delft University of Technology, NL)

Simona Masina (Euro-Mediterranean Center on Climate Change, IT)

Jeremie Mougnot (CNRS Institut des Geosciences de l'Environnement, FR)

Claudia Pasquero (University of Milan Bicocca, IT)

Pau Prats-Iraola (German Aerospace Center (DLR), DE)

Pierre Rampal (CNRS Institut des Geosciences de l'Environnement, FR)

Julienne Stroeve (University of Manitoba, CA)

The scientific content of the report was compiled by Björn Rommen (Scientific Coordinator) based on inputs derived from the MAG, supporting scientific studies and campaign activities, with contributions from Ad Stoffelen, Jan-Peter Muller, Helmut Rott, Thomas Nagler, Gerd-Jan Zadelhoff and Julia Kubanek (campaign coordinator). Additional contributions were made by Anton Korosov, Thomas Newman, Marcel Kleinherenbrink, Einar Ólason, Alexis Mouche, Fabien Desbiolles, Gianluigi Liberti, Daniele Ciani, Andreas Theodosiou, Gert Mulder, Yan Yuan and Rui Song, via supporting science studies.

The technical content of the report was compiled by Erik De Witte (Technical Coordinator) with contributions from Bernardo Carnicero Domínguez, Flavio Mariani, Martin Suess, and Michel Tossaint, based on inputs derived from the industrial Phase 0 system and technical activities under the responsibility of the Future Missions and Instruments Division. Special thanks go to the industrial teams who have supported ESA to bring this report together in a very short time after the Mission Architecture Review.

Recommended citation:

ESA(2020). Report for Assessment: Earth Explorer 10 Candidate Mission Harmony, European Space Agency, Noordwijk, The Netherlands, ESA-EOPSM-HARM-RP-3784, 133pp.

Cover image design: Earth Observation Graphics Bureau (EOGB)

Copyright: 2020 European Space Agency

Contents

Acknowledgments	2
Executive Summary	6
1 Introduction	8
2 Background and Justification	10
2.1 Multi-scale processes in a dynamic Earth	10
2.2 Oceans and Air-Sea Interactions	10
2.2.1 Coupling Air-sea Boundaries	11
2.2.1.1 Relevance and scientific impact	14
2.2.2 Tropical and extra-tropical storms	14
2.2.2.1 Relevance and scientific impact	18
2.2.3 Mesoscale and submesoscales	18
2.2.3.1 Relevance and scientific impact	19
2.3 Cryosphere	20
2.3.1 Elevation changes on glaciers and ice sheets	20
2.3.1.1 Relevance and scientific impact	20
2.3.2 Flow dynamics of glaciers and ice sheets	22
2.3.2.1 Relevance and scientific impact	23
2.3.3 Sea ice deformation	23
2.3.3.1 Relevance and scientific impact	24
2.3.4 Subsidence and erosion in permafrost areas	24
2.3.4.1 Relevance and scientific impact	25
2.4 Solid Earth	25
2.4.1 Earthquakes and Volcanoes	25
2.4.1.1 Relevance and scientific impact	27
3 Mission Objectives	29
3.1 Scientific goals	29
3.2 Mission objectives	31
4 Mission Requirements	34
4.1 Mission requirements at system level	34
4.2 Mission requirement flow-down approach	35
4.3 Ocean and air-sea interaction	36
4.4 Cryosphere	44
4.5 Solid Earth	47
5 Preliminary System Concept(s)	50
5.1 Description of Mission Architecture	50
5.1.1 Objectives and Driving Requirements	50
5.1.2 Mission Architecture	51
5.2 Mission Analysis	53
5.2.1 Assumptions on Sentinel-1	53

5.2.2	Coverage and Revisit	54
5.2.3	Orbit and formation flying	54
5.2.3.1	Stereo phase	55
5.2.3.2	XTI phase	56
5.2.3.3	Transfer phase	56
5.3	Space Segment	57
5.3.1	SAR Instrument	57
5.3.1.1	SAR Antenna Subsystem (SAS)	57
5.3.1.2	SAR Electronic Subsystem (SES)	59
5.3.1.3	Synchronisation with Sentinel-1	60
5.3.2	Optical Instrument	62
5.3.3	Platform Architecture	63
5.3.3.1	Structure and mechanisms	63
5.3.3.2	Thermal control	64
5.3.3.3	Power and energy storage	64
5.3.3.4	Payload Data Handling and Transmission (PDHT)	64
5.3.3.5	Telemetry, tracking and command	64
5.3.3.6	Attitude and orbit control	65
5.3.3.7	Propulsion	65
5.3.4	Satellite Configuration and Budgets	65
5.4	Mission Performance	67
5.4.1	SLC performance	67
5.4.2	USV performance	68
5.4.3	TOC performance	68
5.4.4	TDV performance	70
5.4.5	Top of Atmosphere Radiances (TAR) performance	71
5.5	Ground Segment and Operations	72
5.5.1	Ground segment architecture and options	72
5.5.2	FOS functionality and interfaces	73
5.5.3	PDGS functionality and interfaces	74
5.5.4	Data downlink strategy	75
5.5.5	Mission timeline and disposal	76
6	Data Products and Usage	77
6.1	Data Processing	79
6.1.1	Ocean product data flow	80
6.1.2	Land Ice / Solid Earth product data flow	80
6.2	Data product validation	81
6.3	Data user communities	82
7	Synergies and International Context	83
7.1	Oceans and air-sea interactions: quantify and calibrate multi-scale processes	83
7.2	Cryosphere	86
7.3	Solid Earth	87
A	Mission Performance	88



A.1	Oceans surface products	88
A.1.1	Retrieval Approach	88
A.1.2	Performance Estimation	89
A.2	Cloud-top motion and height	93
A.2.1	Retrieval Approach	93
A.2.2	Performance Estimation	95
A.3	Topography Change (TOC)	97
A.3.1	Retrieval Approach	97
A.3.2	Performance Estimation	98
A.4	3D Velocity vectors (TDV)	100
A.4.1	Retrieval Approach	100
A.4.2	Performance Estimation	102
B	Relevance to Evaluation Criteria	106
	Relevance to ESA Research Objectives for Earth Observation	106
	Need, Usefulness and Excellence	106
	Uniqueness and Complementarity	107
	Degree of Innovation and Contribution to the Advancement of European Earth Ob- servation Capabilities	107
	Feasibility and Level of Maturity	108
	Timeliness	111
	Programmatics	112
	References	114
	Acronyms	129

EXECUTIVE SUMMARY

The Earth is a highly dynamic system where transport and exchanges of energy and matter are regulated by a multitude of processes and feedback mechanisms. The non-linear nature of the governing physics results in couplings between processes happening at a wide range of spatial and temporal scales, with cascades of energy flowing from the larger to the smaller scales and vice-versa. For example, seismic stress induced by large-scale plate tectonics is typically released in highly localized earthquakes, with analogous processes playing out in sea ice. Glacier flow instabilities driven by local sub-glacial mechanics can release large masses of ice to lowlands or the ocean, within a few months or even just seconds. Replenishing these masses takes then many decades and depends on regional-scale climatic conditions. Likewise, tropical cyclones act as a balance-restoring mechanism, transporting massive amounts of energy accumulated in meridional regions to higher latitudes. In this inherently coupled Earth System, ocean heat uptake processes determine the Earth's energy budget and up to one third of the global sea level rise, while Sea Surface Temperature (SST) gradients in turn affect atmospheric dynamics and circulation. Upper ocean temperatures and circulation further influence sea ice properties and dynamics, feeding back onto the ocean circulation via freshwater inputs. Between the atmospheric boundary layer and the oceanic mixed layer, kilometre and sub-kilometre scale coupled processes are responsible for the bulk of the vertical transport of energy and gasses, including fluxes across the air-sea interface, and between the upper ocean and the deep ocean. The wind relative to the moving ocean, local and remotely generated waves, and the state of the coupled Marine Atmospheric Boundary Layer (MABL), all contribute to regulate horizontal and vertical fluxes.

The Earth System cannot be understood or modeled without adequately accounting for small-scale processes. Indeed, the parameterisation of the unresolved, sub-grid physical processes in global or regional models remains one of the main sources of uncertainty in climate projections, in particular with respect to air-sea coupling, cryosphere and clouds. Hence, it remains essential to rely on high-quality observations to sample and identify small-scale processes, to help emulate and calibrate advanced parameterisations of the small unresolved scales. High-resolution observations of the Earth System will thus play an increasingly central role in next generations of fully coupled Earth System Models (or Digital Twins of Earth).

Addressing these needs, Harmony is dedicated to the observation and quantification of small-scale motion and deformation (velocity gradient) fields, primarily, at the air-sea interface (winds, waves, and surface currents, including measurements over extreme events), of the solid Earth (tectonic strain), and in the cryosphere (glacier flows and surface height changes).

The retrieval of kilometre and sub-kilometre scale motion vectors requires concurrent observations of its components. In Harmony, this is achieved by flying two relatively light-weight satellites as companions to a Sentinel-1 mission spacecraft, with a receive-only radar as main payload. The resulting line-of-sight diversity will be exploited in combination with repeat-pass Synthetic Aperture Radar (SAR) interferometry to estimate tiny deformation rates in the solid Earth, and for land ice processes. It will also be used in combination with Doppler estimation techniques for the retrieval of instantaneous ocean and sea ice surface velocities. Over oceans, geometry-diverse measurements of the radar backscatter will further allow the retrieval of surface (wind) stress and wave-spectra. The Harmony spacecraft will also carry a multi-beam thermal-infrared payload, which in the presence of clouds will allow the retrieval



of height-resolved motion vectors. The combination of surface currents, surface wind-stress, along with Thermal Infra-Red (TIR) derived cloud-top height and cloud-top motion vectors will provide an unprecedented view of the MABL. In absence of clouds, the TIR payload will provide simultaneous observations of the sea surface thermal differences, which, in combination with the radar observables, provide a unique window to look at upper-ocean processes and air-sea interactions on the small ocean scales.

The fractionated architecture of Harmony enables the unique capability to reconfigure its flight formation so that instead of being optimised for the measurement of motion vectors, it is optimised for the measurement of time-series of surface topography. This will, among other outcomes, result in a globally consistent and highly resolved view of multi-annual glacier volume changes between well defined epochs, needed to better quantify the climatic response of glaciers. At the same time, Harmony will allow studying the seasonal and sub-seasonal processes from space that play a role in such responses, for instance by measuring variations in lateral ice flow and associated elevation changes simultaneously over large areas for the first time.

Technically the Harmony mission is considered relatively mature for the stage of the project. The observation concept leverages the high performing Sentinel-1 satellite to implement new capabilities. This approach allows it to address its science goals that would otherwise be much more difficult to accomplish within the constraints of an Earth Explorer.

The Harmony mission will result in a significant advance in several scientific domains. Each of the domains have clearly formulated scientific objectives that are organised as primary and secondary objectives. The mission has been designed so that the primary objectives can be fully met by the mission without the need for compromise between them. This report focuses on the primary mission objectives:

1. Air-sea interaction, tropical and extra-tropical cyclones, and ocean mesoscale and sub-mesoscale processes;
2. Tectonic strain; and
3. Glacier and ice-sheet mass balance and glacier dynamics.

Harmony will make significant contributions to other science domains, including volcanoes, permafrost, land-slides and several sea-ice objectives. These have been captured as secondary mission objectives and have been studied in some depth in the Phase 0 science studies.

1 INTRODUCTION

ESA Research missions drive the Earth science agenda, technical innovation in Earth observing capabilities and future applications perspective within the Future Earth Observation (FutureEO) Programme. Earth Explorer missions focus on the atmosphere, biosphere, hydrosphere, cryosphere and the Earth's interior with emphasis on the interactions between these components and on the impact that human activities have on the Earth's processes. ESA's Earth Observation Science Strategy aims to cover all areas of science to which Earth observation missions can contribute. ESA's Earth Observation Science Strategy ([SP-1329/1](#)) provides key elements and scientific direction for the future progress of ESA's Living Planet Programme. The context and specific scientific challenges to increase knowledge and capabilities in the five Earth science disciplines – atmosphere, cryosphere, land surface, ocean and solid Earth – are identified in the complementary volume ([SP-1329/2](#)).

The Call for Earth Explorer 10 (EE10) Mission Ideas was released in October 2017 and three mission candidates were selected for a Phase 0 study out of 21 proposals in July 2018. The three candidate missions selected for assessment phase study activities are:

- **Daedalus:** A low flying spacecraft for the exploration of the lower thermosphere-ionosphere – a mission to quantify key electrodynamic processes that embrace the transition region between the upper atmosphere and the near-earth region of space;
- **Harmony:** Stereo thermo-optically enhanced radar for Earth, ocean, ice and land dynamics – a mission dedicated to the observation and quantification of small-scale motion and deformation fields to allow data-driven representations of processes in Earth System models;
- **Hydroterra:** A radar in geosynchronous orbit over Africa and Europe to observe and understand key processes of the daily water cycle, to improve prediction capability of intense rainfall and related flooding and landslides, and to enable the near real time prediction of ground motion.

At the end of the Phase 0 study activities a down-selection will be performed. Up to two candidate mission(s) compatible with the scientific, technical and programmatic boundary conditions will be selected to proceed to Phase A study.

The Reports for Assessment capture the status of the respective mission idea at the end of Phase 0 activities. The three volumes will be provided to the Advisory Committee for Earth Observation as a basis for a subsequent recommendation for up to two mission candidates to enter Phase A.

Each Report for Assessment follows a common format and logic. Each identifies the scientific questions and related key societal issues motivating the mission and its objectives. After establishing the scientific basis and rationale, the specific mission objectives are outlined and traced to a set of requirements used for system concept definition.

Each report comprises this introductory first chapter and eight subsequent chapters as follows:

Chapter 2 identifies the background and scientific issues to be addressed by the mission. It provides justification for the mission and includes a review of the current scientific under-

standing of the issue in question while identifying the potential advances in knowledge that the mission could provide.

Chapter 3 draws on arguments presented in Chapter 2, and summarises specific scientific goals and related mission objectives.

Chapter 4 outlines the mission requirements, through providing quantitative descriptions and justification, including prioritisation, of the Level 2 geophysical requirements that would allow to fulfil the mission objectives.

Chapter 5 provides an overview of the preliminary mission architecture and the system elements, including the space segment, ground segment, and operations.

Chapter 6 gives a qualitative description of the data products at Level 1 and Level 2, the operational data processing and how the data acquired by this mission would be used – and includes a description of the data user communities.

Chapter 7 describes the synergies and international context of the mission.

Appendix A briefly presents the retrieval approach, performance estimation with simulated and/or experimental data, and the validation concept.

Appendix B documents the relevance of the mission to the evaluation criteria.

This volume deals with the result of the Harmony mission at the end of Phase o.

2 BACKGROUND AND JUSTIFICATION

2.1 Multi-scale processes in a dynamic Earth

The Earth is a highly dynamic system where transport and exchanges of energy and matter are regulated by a multitude of processes and feedback mechanisms. The non-linear nature of the governing physics results in couplings between processes happening at a wide range of spatial and temporal scales, with cascades of energy flowing from the larger to the smaller scales and vice-versa. For example, seismic stress induced by large-scale plate tectonics is typically released in highly localized earthquakes, with analogous processes playing out in sea ice. Glacier flow instabilities driven by local sub-glacial mechanics can release large masses of ice to lowlands or the ocean, within a few months or even just seconds. Replenishing these masses takes then many decades and depends on regional-scale climatic conditions. Likewise, tropical cyclones act as a balance-restoring mechanism, transporting massive amounts of energy accumulated in meridional regions to higher latitudes. In this inherently coupled Earth System, ocean heat uptake processes determine the Earth's energy budget and about one third global sea level rise, while SST in turn affect atmospheric dynamics and circulation. Upper ocean temperatures and circulation further influence sea ice properties and dynamics, feeding back onto the ocean circulation via freshwater inputs. Between the atmospheric boundary layer and the oceanic mixed layer, kilometer and sub-kilometer scale coupled processes are responsible for the bulk of the vertical transport of energy and gasses, including fluxes across the air-sea interface, and between the upper ocean and the deep ocean. The wind relative to the moving ocean, local and remotely generated waves, and the state of the coupled MABL, all contribute to regulate horizontal and vertical fluxes.

The Earth System cannot be understood or modeled without adequately accounting for small-scale processes. Indeed, the parameterisation of the unresolved, sub-grid physical processes in global or regional models remains one of the main sources of uncertainty in climate projections, in particular with respect to air-sea coupling, cryosphere and clouds. This will be partially addressed by future full Earth System Models, or Digital Twins of Earth (DTEs). However, the development and subsequent validation of these models requires high-quality observations to sample, identify and quantify small-scale processes. These observations are needed, for example, to develop and calibrate data-driven parameterisations of the remaining unresolved scales.

2.2 Oceans and Air-Sea Interactions

The interactions between oceans and atmosphere over 70% of the Earth surface shape the environment where humanity lives, by regulating heat, freshwater, gas, and momentum transfer at the surface. For example, the recent increase of carbon dioxide and heat into the atmosphere is largely buffered by the absorption from the oceans, which now contain about 25% of the anthropogenic CO₂ (Le Quéré et al., 2018) and about 90% of the excess heat with respect to the mid 20th century (IPCC, 2014). Small ocean eddy scale air-sea feedbacks drive wind adjustment over SST fronts, convective processes, low-level cloud formations, and secondary marine atmospheric boundary layer (MABL) circulations, impacting on the atmosphere-ocean exchanges which vary by orders of magnitude depending on the local unbalance between air and water. They are also likely to drive changes in the incidence and intensity of extreme weather events (Hirons et al., 2018; Yu, 2019), and certainly modulate marine ecosystems functioning and related services.

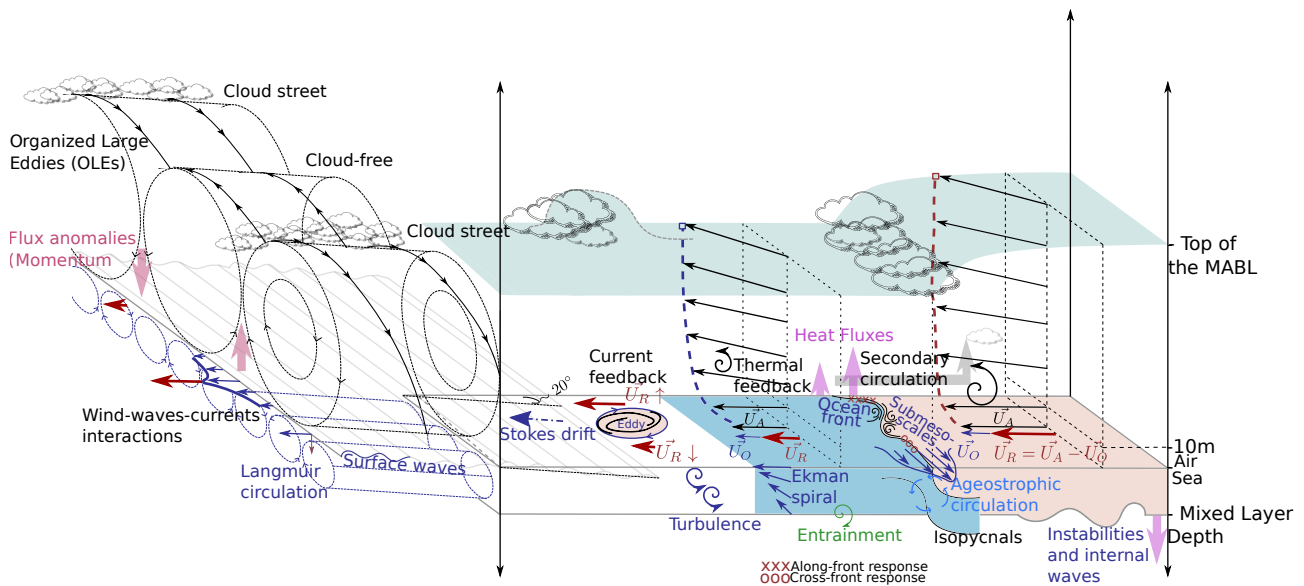


Figure 2.1: Cartoon showing a number of key oceanic and atmospheric processes in the Marine Atmospheric Boundary Layer (MABL), the upper ocean, and at the interface between both. Represented on the left, organized eddies in the MABL, with horizontal and vertical scales in the order of a kilometer, and Stokes-drift driven Langmuir circulation in the oceanic Mixed Layer (ML) ($O(100\text{ m})$ scales) represent a major contribution to vertical fluxes. On the right, thermal ocean fronts modulate the stability of the atmosphere, increasing the surface-stress the warmer side of the front, which in turn leads to increased momentum, heat and CO_2 fluxes across the air-sea interface. Ocean front instabilities and eddy perturbations at the mesoscale and submesoscale drive intense vertical exchanges with the deep ocean.

Air-sea exchanges depend on the disequilibrium between lower atmosphere and upper ocean. They tend to re-establish the balance, but several processes act to maintain the unbalance, such as rolls and large eddies redistributing heat and momentum in the MABL, convective cells thickening the layers directly affected by the air-sea interactions, vertical motions related to convergence and divergence at the surface, Langmuir circulation directly associated with surface wave Stokes drift, lateral transport by currents and winds, and many others. Figure 2.1 illustrates some of the key small-scale processes at play at both sides of the air-sea interface.

Importantly, air-sea fluxes involve processes at multiple scales: the molecular scale of spray dynamics; slick and/or rain wind ripple scale ($O(1\text{ cm})$); the scale of wave breaking ($O(1\text{ m})$), the submesoscale of fronts and wave current interactions ($O(0.1\text{ km to }1\text{ km})$), to the atmospheric synoptic scales ($O(1000\text{ km})$), basin and global scales ($O(10000\text{ km})$), where $O(\cdot)$ denotes the order of magnitude. Figure 2.2 provides an overview of a range of key oceanic and atmospheric processes showing their temporal and spatial scales, as well as anticipating the range of scales that can be resolved by Harmony.

2.2.1 Coupling Air-sea Boundaries

The capability to predict Earth system evolution strongly depends on a correct representation of processes at the air-sea interface. However, a complete understanding of the coupled

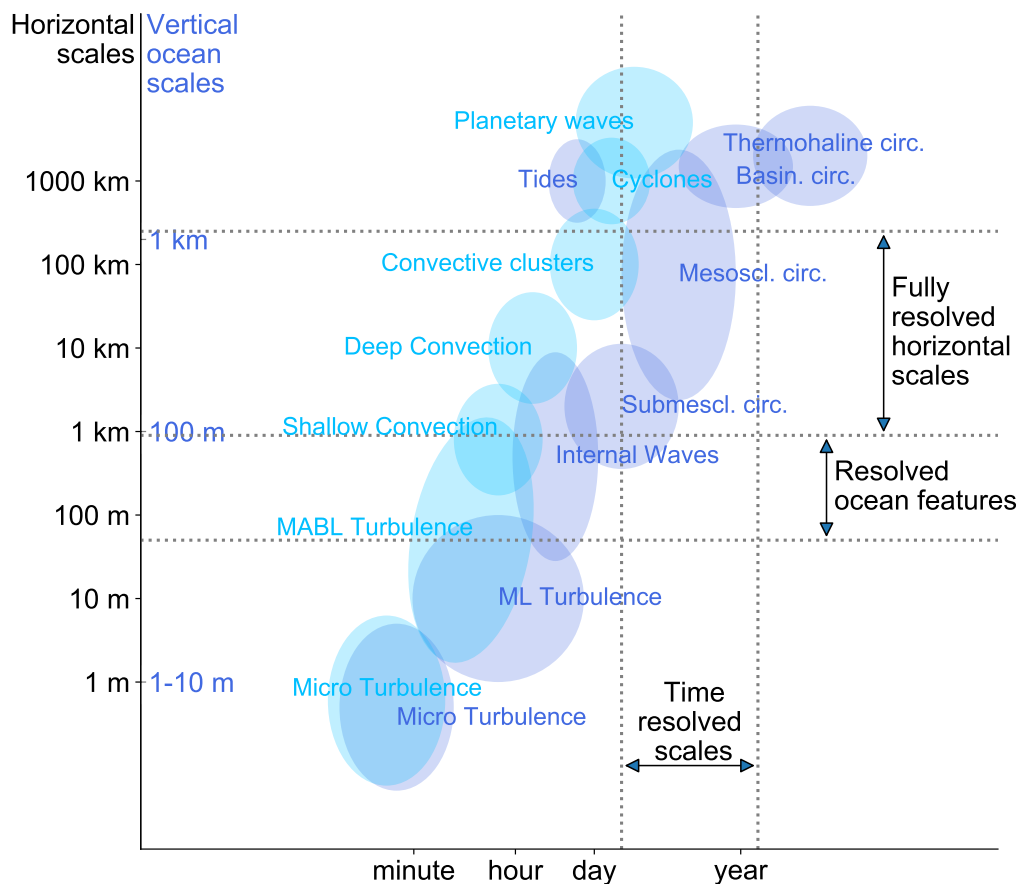


Figure 2.2: Temporal scales (horizontal axis) and spatial scales (vertical axis) of a number of key oceanic and atmospheric processes. For ocean processes, indicated as dark-blue bubbles, their vertical scales are also indicated. For the same spatial scale, atmospheric phenomena (light-blue bubbles) have considerably shorter lifespans.

dynamics of the atmosphere and ocean boundary layers is presently hindered by the lack of contemporaneous observations of co-located vector winds, directional waves, ocean current vectors at spatial scales smaller than $O(10 \text{ km})$, and SST. These processes will also not be resolved in basin-scale models that will be developed in the coming decades, emphasizing the need to more consistently improve current parameterisations in numerical Earth system models. The coupled interactions between SST, ocean surface winds, waves and surface currents are still unsatisfactorily parameterized in global climate models (Belmonte Rivas and Stoffelen, 2019; Trindade et al., 2020), and numerous efforts are currently testing model sensitivities. To help calibrate improved theoretical or data-driven parameterisations it is crucial to build an as complete as possible portfolio of quantitative high-resolution observations of situations under differing environmental conditions. Today, such an ensemble of cases is missing, and parameterisations, that take into consideration the wave-current-wind interactions to compute accurate fluxes at the air-sea interface, are mostly evaluated with numerical simulations (Romero et al., 2020; Renault et al., 2016a) and lack full validation and calibration.

High-resolution optical satellite imagery often reveals that horizontal and vertical gradients of SST, surface current, and surface waves all impact the surface winds, surface stress and, consequently, vertical fluxes. Air-sea exchanges are further modulated by a separate contribution: non-gradient fluxes associated with secondary highly organized quasi-coherent flows that can provide additional vertical exchanges through each boundary layer (atmosphere and ocean), connected to the flows above and below. Yet, the scientific community is generally confronted with the problem of simplifying (parameterizing) these full and complex exchanges of heat and momentum at the air-sea interface upward into the atmosphere and downward into the ocean, armed primarily with simplified local flux models. This also affects gas exchange estimates, as upper ocean processes impacting vertical shear and vertical mixing in the upper ocean can modulate vertical motions and the supply of carbon-rich water from below, but also the rate of wave breaking (e.g. Woolf (1997)), surface slicks (e.g., Frew et al. (1990)), and/or thermal skin effects (e.g. Robertson and Watson (1992); Watson et al. (2020)).

To simply illustrate these complex interactions, depending on the alignment of the surface currents with respect to the surface wind, the air-sea relative velocity will be larger or smaller, increasing or reducing the friction at the air-sea interface and, thereby, also increasing or reducing the momentum transfer into the ocean. It can then be hypothesized that interactions between ocean and atmosphere, leading to negative correlation between wind stress curl and ocean current relative vorticity, overall act as an *eddy killer* mechanism, as mechanical energy is transferred from the ocean mesoscale to the atmosphere (Eden and Dietze, 2009; Hutchinson et al., 2010; Oerder et al., 2018; Renault et al., 2016b, 2017; Xu and Scott, 2008).

Air-sea fluxes are also affected by the vertical mixing within the lower troposphere and within the upper ocean. A weak coupling between the surface layer and the layers away from the surface allows for a quick balancing of any air-sea disequilibrium, with the effect of limiting the exchanges at the interface. Vertical exchanges in the atmospheric boundary layer are favored by turbulence and inhibited by stable stratification. The MABL is typically in a weakly unstable condition, but very stable conditions (such as in upwelling systems or at edges of marginal ice zones) or very unstable conditions (such as over western boundary currents) are not uncommon, in presence of strong thermal disequilibrium between the upper ocean and the lower atmosphere. Simultaneous observations of surface ocean and lower troposphere properties at small scales are currently not feasible, but it is still possible to obtain indirect information on the vertical exchanges by focusing on the momentum transfer, whose imprint is in the small scale surface wind variations, as demonstrated by the presence of a positive correlation between mesoscale and submesoscale thermal anomalies and surface winds (Chelton and Xie, 2010; Seo, 2017; Gaube et al., 2019; Meroni et al., 2020; Gentemann et al., 2020). Those correlations are typically considered to be the effect of the increased coupling between surface winds and the stronger winds aloft when the warm sea surface temperature destabilizes the air column. Due to the fast atmospheric response and to the fast evolution of small-scale unbalanced structures in the ocean, it is necessary to simultaneously observe surface winds and sea surface temperature differences. The simultaneous observation of the wind velocity and, more importantly, its alignment at the top of the boundary layer, as made possible in specific conditions by retrieving low level cloud structure (Klein et al., 1995) and Cloud Motion Vectors (CMV), traces secondary circulation to allow an improved characterization

of the link between vertical exchanges in the MABL and sea surface thermal features.

Turning our attention to present observational capabilities, besides highly resolved optical observations, all-weather observing systems do not provide the simultaneous observations of surface ocean motion, wave spectra, and surface wind stress at the kilometer or sub-kilometer scales that are necessary to provide an adequate description of these air-sea interactions.

So, while scatterometer ocean roughness data already provide important information, lack of contemporaneous surface motion detection and a $O(20 \text{ km})$ spatial resolution that is too coarse to resolve fine-scale processes (MABL coherent structures, sea states and/or surface layer slicks and current) prevent to precisely document these key aspects to disentangle small ocean-scale processes and interactions. Ocean surface imagery from SAR can ensure both criteria: high-resolution and all-weather imaging with surface motion Doppler detection. MABL imprints and/or co-located signatures over SST gradients have already been observed and studied. However, current systems, limited to a single line-of-sight, cannot provide directional information to fully quantify the dynamical properties of detected ocean roughness, which are needed to obtain wind stress and ocean motion vectors.

2.2.1.1 Relevance and scientific impact

Current parameterisations are already optimally tuned to be consistent with current observations. However, the highly non-linear nature of the Earth system requires models to adequately represent all scales in order to remain valid under various regional and global climate evolutions. Failing to do so is seriously hindering our ability to anticipate the full extent of climate variations and their consequences (Schneider et al., 2017; Palmer and Stevens, 2019).

Both short-term and long-term prediction skills of numerical simulations are still limited by uncertainties in the parameterisations used to represent the processes that the models cannot resolve explicitly. These unresolved scales must thus be observed, measured, before approximate laws can lead to efficient parameterisations. In that endeavor, Harmony will provide, for the first time, coincident observations of surface stress and surface current vectors at $O(1 \text{ km})$ scales, combined with improved surface wave-spectra and, depending on cloud-cover conditions, SST at similar scales and/or cloud-top motion and height information. These highly complementary observations will be systematically collected, spanning different sea surface temperature (SST), and lower atmosphere stability and motion conditions up-to the cloud-top height, to allow the quantification of the different multi-scale processes that play a role in the ocean-atmosphere coupling and the conditional variability of the different variables. This information will enter and steer the development and calibration of air-sea couplings in a new generation of Earth System Models, which are expected to increasingly rely on parameter learning methods, through a combination of data assimilation, inverse problems, and data-driven deep learning techniques (Schneider et al., 2017; Reichstein et al., 2019; Bolton and Zanna, 2019).

2.2.2 Tropical and extra-tropical storms

In view of their impacts on the coupled ocean-atmosphere system, marine-atmosphere extremes, i.e. Tropical Cyclone (TC), extra-tropical and Arctic cyclones (Extra Tropical Cyclones (ETCs), and Polar Lows (PLs)), are an integral part of the climate-change questions. For instance, TCs play a substantial role in the maintenance of the general atmospheric cir-

ulation in the Northern Hemisphere. In the second half of the year, TCs transport into mid-latitude about half of the total moisture and angular momentum. As well, Zhang et al. (2020) recently reported how cyclonic mesoscale ocean eddies can be invigorated by strong wind storms. This in turn can enforce the transfer of energy to the Gulf Stream and its Pacific counterpart Kuroshio. Indeed, moving into the current, eddies provide a feedback between TC statistics (intensity, occurrence, trajectories, motions) and ocean heat transport. Moreover, synoptic cyclones in mid- and high-latitudes govern dynamics of the meridional energy fluxes in the Earth's climate system (Trenberth and Stepaniak, 2004).

TCs and ETCs are fueled by intense air-sea fluxes, which are very difficult to fully assess. From large meso-vortices to small scales, a storm evolution is strongly influenced by atmosphere-ocean feedbacks. Strong winds intensify enthalpy fluxes from the ocean into the atmosphere (positive feedback), but also trigger strong mixing and vertical motions in the upper ocean, reducing sea surface temperature (negative feedback). Moreover, rapidly varying high winds in both time and space can trigger the generation of energetic wave events, localized transient intense heat and momentum surface fluxes, as well as density and biological changes in the ocean mixed layer. Questions related to large wave breaking events and gas bubbles on mediating air-sea CO₂ fluxes are matter of debate (Liang et al., 2020). All these processes are still poorly parameterized to predict trends of Marine-Atmosphere extremes in future.

In that context, the only satellite technology capable of producing fine-scale, wide-swath surface and boundary layer process data in nearly all-weather conditions is SAR. All-weather capability is important since rain contamination is a major limitation of the much coarser resolution Ku-band scatterometers (e.g. QuikSCAT) or passive microwave systems (e.g. WindSAT, AMSR-2).

Depending on their translation speed over the tropical oceans, TCs events instigate isolated blasts of vigorous mixing, stirring warm surface water with cooler water in the thermocline. Temperature and salinity conditions within surface and subsurface ocean can then either influence a TC's intensification or relaxation. When the hurricane moves, it will also trigger a wake plume or an internal-wave wake, formed by internal inertia-gravity waves, annular and wedge-shaped, i.e., analogous to a Kelvin wave wedge behind a moving ship. TC passages can then leave spectacular signatures. The strong winds associated with tropical cyclones are responsible for the generation of cold wakes, with SST anomalies as large as -10°C (Chiang et al., 2011) for slow-moving TCs. The surface cooling is due to wind induced vertical mixing, Ekman upwelling of colder water from below, more precisely, the baroclinic and barotropic interior ocean responses (e.g. Kudryavtsev et al. (2019a)), and enhanced air-sea fluxes (Price, 1981; D'Asaro et al., 2007; Sanford et al., 2007). Triggered along the path of moving TCs, very large interior ocean vertical displacements associated to baroclinic and barotropic responses can then leave prominent sea surface height (SSH) anomalies in the TC wake. Resulting surface depressions can reach 0.3–0.5 m, depending upon size, translation speed, and ocean stratification conditions (Kudryavtsev et al., 2019a; Combot et al., 2020). Importantly, these ocean interior responses, baroclinic and barotropic along with cooling, are typically present below the eye, certainly impacting the intensification of the cyclone itself (Mogensen et al., 2017). Figure 2.3 illustrates some of these coupled processes.

Today, only the resulting effects of a TC passage can be analyzed. Within the most intense inner-core area, there is no remote sensing satellite observing system to inform about these

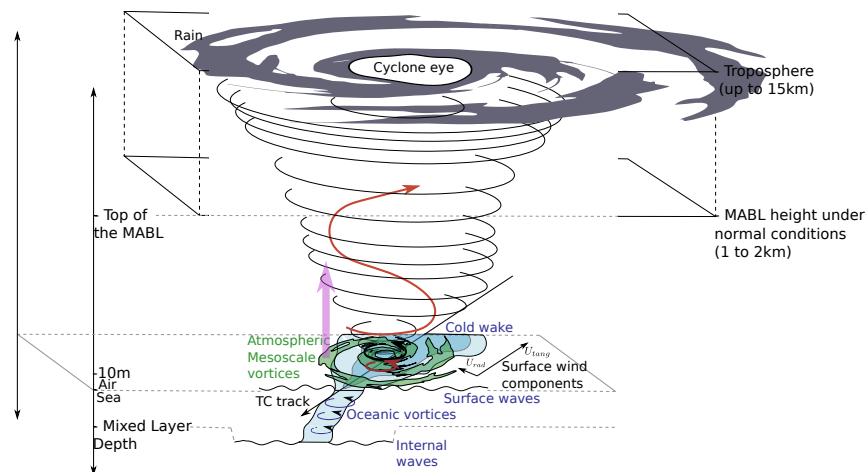


Figure 2.3: Cartoon illustrating the pass of a Tropical Cyclone, inducing extreme heat and momentum fluxes in the atmosphere and across the air-sea interface, and intense mixing in the upper ocean, creating a wake of a deepened Mixed Layer (ML) and with significantly lower surface temperature. Mesoscale and submesoscale rolls and vortices within the TC are considered to play major role in the evolution of the storm, but are very poorly understood due to the lack of high-resolution observations.

extreme horizontal and vertical interior motions.

Moreover, upper ocean signatures of extreme storms are relatively persistent (Mei and Pasquero, 2013a). In the days following the event, the cold wake reduces air-sea fluxes, suppressing cloud cover and rainfall (Ma et al., 2020). Surface signatures then decay and disappear over a time scale of a couple of weeks for the SST signature (Price et al., 2008; Dare and McBride, 2011; Mei and Pasquero, 2013b). Yet, there is evidence that the subsurface warm anomaly persists for a much longer time (Mei et al., 2013), potentially affecting the subsequent evolution of tropical cyclones in the same season (Pasquero and Emanuel, 2008), as well as local and remote climate (Emanuel, 2002; Jansen and Ferrari, 2009; Sriviver et al., 2010). A quantification of the net long-term effect of marine-atmosphere extremes on the upper ocean heat content, however, is currently highly debated. It depends on anomalous air-sea fluxes in the presence of the lower SST and on the upper ocean vertical heat transport associated with baroclinic instabilities that develop near thermal fronts (Boccaletti et al., 2007; Mei and Pasquero, 2012). The depth reached by the warm anomaly depends on the near inertial waves excited by the TC, that propagate downward into the deep ocean and contribute to mixing even at large distances from their origin (Alford et al., 2016; Meroni et al., 2017) The disentanglement of the different contributions and the localization of the overall effects of TCs on ocean warming requires the monitoring of the small-scale ocean dynamics in the tropical cyclone wake.

Harmony's all weather and high resolution capabilities will result in the first system capable of providing co-located surface wind, wave and current directional information, at sufficient resolution to resolve both atmospheric and ocean boundary layer characteristics. Harmony can thus uniquely shed light onto both the local dynamical effects and also on the non-local restratification processes by providing measurements of surface motions, including internal and surface wave directional distributions, to further help fully characterize the near iner-

tial waves excited by the TC winds that generate strong mixed layer currents ($O(80\text{cm/s})$, Kudryavtsev et al. (2019b); Lu et al. (2020)), and their impacts on bubble-induced supersaturation to advance gas flux parameterization under extreme conditions.

Regarding the improved understanding of the air-sea interactions to control the inward convergence of near-surface humidity and angular momentum, i.e., the Carnot engine that drives the storm dynamics, assimilation of standard resolution (~ 25 to 50 km) satellite data have improved the representation of the synoptic scale steering flow and consequently improved tropical cyclone (TC) track forecasts over the past 15 years. However, the same satellite data have had very little impact on intensity forecasts. This is because the physical processes associated with changes in TC intensity are of much smaller scale and not well parameterized in Earth system models. Thus, in spite of the World Meteorological Organisation (WMO) Regional Specialized Meteorological Centres (RSMC) for tropical cyclones, massively integrating satellite observations and model outputs to monitor and issue short-term TC forecasts to public authorities, severe forecast errors remain. Of particular importance, rapid intensification (RI, e.g. Smith and Montgomery (2015)) is responsible for the highest forecast errors, and for a disproportionate amount of human and financial losses. While far to be reliably predicted, RI is not rare and found in about 15-20% of the global tropical cyclones. Those RI events are not only poorly understood, but also difficult to sample in time, remaining a major challenge for forecasters.

Recent work documented the presence of a link between their occurrence and the dynamics of mesoscale vortical plume structures embedded into the cyclone (Gall et al., 2013; Montgomery and Smith, 2014), but their study is limited by the lack of available data, especially TC inner-core, i.e., including the eyewall and the deep convection region outside it.

Based on RADARSAT-2 SAR acquisitions, cross-polarized C-band radar signals were unambiguously demonstrated to be highly sensitive to wind speeds (see also van Zadelhoff et al. (2014)), with very low sensitivity to wind direction and radar incidence angle, to open new and very robust high-resolution mapping of severe storms (e.g. Mouche et al. (2017)). Today, with a catalogue of more than 300 cases (e.g. Combet et al. (2020)), Sentinel-1 data already present unique opportunities to devise new remote sensing capabilities that can lead to an improved understanding of the small-scale ocean surface boundary layer processes and turbulent fluxes under extreme conditions, including the structure inside the eye. It is evident that SAR data can provide an accurate and detailed image of the TC low-level super-gradient winds near and outside the radius of maximum winds that are associated with lower central pressure. Available and future SAR observations are however only one-dimensional and directed in the line-of-sight. Thus, the non-axisymmetric aspects of the flow which play a major role in the formation and intensification of the storms cannot presently be directly retrieved.

By resolving surface roughness directional variations down to $O(500\text{m})$ scales, Harmony will have the unique capability to resolve Organized Large Eddies (OLEs) in the TC boundary layer, and in particular to map their orientations. Combined with the surface wind, this will allow the quantification of near-surface inflow and associated storm boundary layer structure. Careful studies of events that will combine Harmony and aircraft remote sensing will significantly improve our ability to interpret the data from any of these sensors and to exploit their derived products to estimate physically-realistic vertical profiles of the effective

turbulent eddy viscosity and mean wind profiles in the boundary layer for the full sampling of extreme events.

2.2.2.1 Relevance and scientific impact

Harmony's direct motion and stress vector measurements, combined with directional wave and current estimates, will thus uniquely and significantly expand on what is now known about the dynamics of boundary layer processes under extreme marine-atmosphere conditions. Building on improved directional capabilities, novel derived products (boundary layer characteristics in different intensity change regimes, vertical mean wind and turbulent eddy viscosity profiles) shall then provide new information, highly needed to refine parameterizations of air-sea interactions under extreme conditions. This will lead to improved forecasting of the evolution of TCs and ETCs and also to a better representation of marine-atmosphere extremes in regional and global climate models.

2.2.3 Mesoscale and submesoscales

Small-scale dynamical features are ubiquitous in the upper ocean: at any time, an instantaneous ocean surface observation from space, on a synoptic scale of 100 km with resolutions in the order of 20 m, will reveal a host of oceanic signatures, e.g., internal waves (Alpers, 1985; Hsu et al., 2000), filaments and/or spiralling eddies (Ivanov and Ginzburg, 2002; Kudryavtsev et al., 2005, 2012b; Raschle et al., 2017), which affect the air-sea fluxes and contribute to modulate ocean circulation and to shape the seascape for marine biome. Owing to their small-to-moderate lateral scale (0.1–10 km), variable thickness of the affected layer (0.01–1 km) and ephemeral evolving nature (hours to few days), most of the processes at these scales (occurring within the sub-mesoscale and high-latitude mesoscale dynamical regimes) represent a major observational challenge that is not addressed by traditional in-situ ocean sampling and existing satellite Earth observation missions. These processes have a significant impact on several components of the Earth system dynamics, as mesoscale and sub-mesoscale secondary circulations modulate the vertical transport of energy, momentum, chemicals and organisms across the base of the mixed layer, and thus regulate heat absorption and carbon sequestration.

A strong relation between mixed layer depth and sub-mesoscale processes is found in surface frontogenesis and mixed layer baroclinic instabilities (e.g., Fox-Kemper et al. (2008)). Sub-mesoscale features are deemed responsible for a significant part of the vertical transport of heat in the upper ocean and of the exchange of planktonic organisms, dissolved and particulate carbon and nutrients across the base of the euphotic layer (e.g., Lévy et al. (2018); Siegelman et al. (2020)). Moreover, observations and numerical simulations suggest that sub-mesoscale processes can have strong seasonality, being much more energetic in winter than in summer, to also display strong regional contrasts, in tight correspondence with mixed layer thickness variability.

A major shortcoming is that most of our understanding of sub-mesoscale dynamics and energy transfers between scales mostly comes from high resolution numerical modelling and theoretical studies. Only few generation mechanisms have been more deeply investigated and confirmed through observational efforts and dedicated campaigns. Fronts and eddies identified with aerial guidance, further seeded with drifters, occasionally helped to better quantify sub-mesoscale flow kinematics, providing a first reference range for model assess-

ment and tuning (D'Asaro et al., 2018). Reported analysis indicate mean divergence and vorticity values that can vary largely, both in time and spatially, far exceed 5 and even 30 times the Coriolis frequency (Raschle et al., 2017, 2020), which represent very extreme departures from geostrophic balance, and suggest intense vertical motion induced by sub-mesoscale features (Lodise et al., 2020). A key aspect is that information pertaining to wind, thermal and surface current changes, associated to sub-mesoscale ocean features, all largely imprint on the sea surface, as directional variations of both ocean surface roughness and kinematics at sub-km scales, in addition to ocean surface swell refraction at O(10-50 km) scales.

Needless to mention that along the thinning of Arctic ice cover, the upper ocean circulation, but also the speed, magnitude, and extent of ocean wave propagation into the pack ice, are all changing. For instance, travelling into the continuous ice cover, ocean waves are damped because of their energy being transformed to break up the sea ice into pieces. This damping mechanism strongly depends on the local sea-ice thickness and concentration. Once the Marginal Ice Zone (MIZ) has formed, waves can travel further into the pack ice and contribute to break apart the ice because the damping process is then much less effective. As a result, the MIZ tends to have high open-water lead fractions (> 0.5), with large inter-annual variability in ice motions (divergence/convergence). This variability is also not accounted for by current climate models and can contribute to biases and errors in sea-ice forecasts.

2.2.3.1 Relevance and scientific impact

Harmony shall provide unique observational capabilities to unambiguously map and quantify upper ocean surface flows, to identify the surface current vorticity, shear and divergence, with associated vertical velocities, well within the sub-mesoscale range of scales, at all latitudes and over the full year.

To note, the larger scales, mostly in geostrophic balance, termed as mesoscale eddies, are usually well described by sea surface height data, i.e., altimeter measurements. However, the Rossby deformation radius, which sets the size of these ocean mesoscale eddies, strongly depends on latitude, ranging from hundreds of kilometers at low latitudes to about 10 kilometers in the Arctic (Chelton et al., 1998; Nurser and Bacon, 2014). Comparable to the sub-mesoscale range of scales at low latitudes, the small size of mesoscale features in the high-latitude regions are not well observed by the operative constellation of satellites, neither well represented by numerical models. While the role that ocean mesoscale eddies play in the climate and ecosystem has long been identified and investigated through both observational and modelling efforts, the dynamics of eddy perturbations and interactions with smaller scale processes are far less understood (e.g., (Nardelli, 2013; Pilo et al., 2018). Foremost, studies indicate that deep water formation in the Labrador Sea can be impacted (Tagklis et al. 2020, submitted), causing dramatic thickening of the MABL to also generate low level cloud streets resulting in huge perturbations to the air-sea fluxes (Renfrew and Moore, 1999). Questions further arise relative to their control on large scale ocean circulation and sea ice distribution in the Arctic.

Exploiting the SAR measurement principle, algorithms for detecting and quantifying swell propagating in the MIZ have already been demonstrated (Ardhuin et al., 2015) for high-resolution Sentinel-1 SAR products. For that purpose, measuring multi-directional surface motions, Harmony will largely improve available satellite observations, to enable a more precise retrieval of surface wave propagation properties in the MIZ at kilometer to sub-kilometer

resolution, to derive information related to ice concentration and thickness distributions (Belmonte Rivas et al., 2018), along with ice mechanical parameters (e.g the Young's modulus).

2.3 Cryosphere

The cryosphere is an important part of the Earth's system that reacts extremely sensitively to climate fluctuations. In recent decades, global atmospheric and oceanic warming has led to a widespread shrinkage of the cryosphere, with a loss of mass for ice sheets and glaciers, a reduction in snow cover and sea ice extent, and degradation of permafrost. Exploiting the many capabilities that Harmony offers together with Sentinel-1, the mission can explore each cryosphere component to provide more accurate observations than presently available or even fundamentally new ones that will significantly improve our understanding of the state and fate of Earth's cryosphere.

Glaciers and ice sheets adjust to the current climatic forcing through a diminution of their volume and increase of discharge into the oceans, hence contributing to changes in river runoff, input of fresh water into the ocean and the rise of global sea level. Arctic sea ice is decreasing dramatically and transitioning from a perennial ice cover to a seasonal one, influencing the energy exchange between atmosphere and ocean. Arctic and boreal permafrost is thawing and degrading, and has the strong potential to release greenhouse gases and to create powerful global climate feedbacks. All components of the cryosphere are dynamical systems where observations of topographic changes and 3D-deformation are crucial to improve our understanding of their evolution and of their interactions within the Earth's system. Both of these observables are accessible to Harmony in an unprecedented way.

2.3.1 Elevation changes on glaciers and ice sheets

At present, studies of glacier elevation change are usually only regional, and often a spatio-temporal patchwork based on multiple datasets with different time stamps. In addition, as the extent of the vast majority of glaciers is relatively small, observations made by current space altimeters are not sufficient to resolve them properly, potentially creating sampling biases in our knowledge of current glacier evolution. Only higher-resolution observations could allow representative sampling of glaciers worldwide and therefore improve our understanding of spatial patterns and change processes at play. The current set of well-observed mountain glaciers with volume changes measurements constitutes only a small fraction of the global total (IPCC, 2014; Zemp et al., 2019) and important gaps for the ice sheets (McMillan et al., 2014; Smith et al., 2020) still persist in regions where the topography is complex due to the limited horizontal resolution of the current altimeters. As a result, global glacier mass balance measurements are based either on extrapolation from various data sources or on parametric models driven by climate data. These deficits stress the need for comprehensive observations of ice masses, in order to improve the representation of the driving mechanisms in regional and global models of ice flow dynamics and mass balance, and to consolidate projections of the impact of future climate conditions.

2.3.1.1 Relevance and scientific impact

In Across-Track Interferometry (XTI) mode, the Harmony mission will be able to fill major gaps in global glacier monitoring by providing comprehensive and spatially detailed measurements of surface elevation changes of glaciers and outlet glaciers of ice sheets over well-

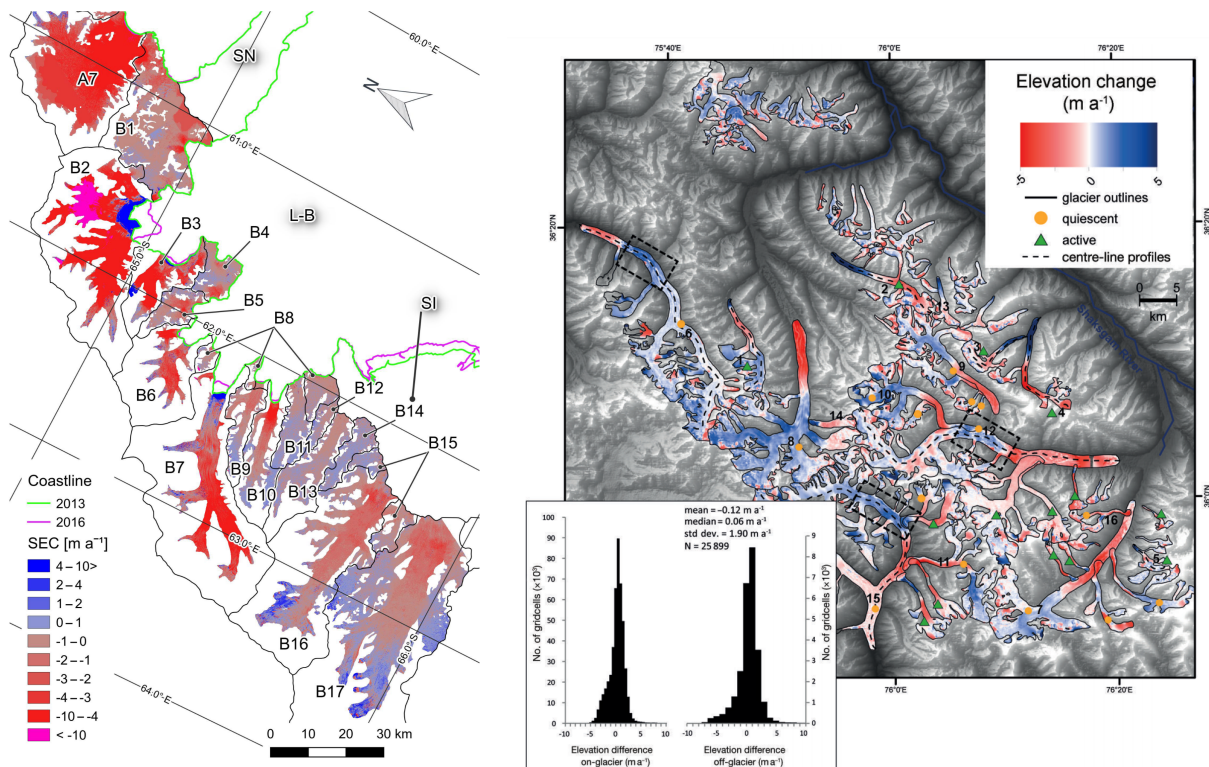


Figure 2.4: (Left) Map of surface elevation change (Topography Changes (TOC) m/yr) for glaciers of Larsen B embayment, Antarctic Peninsula based on SP-InSAR DEMs of TanDEM-X from May/June 2011 to June/July 2013 from Rott et al. (2018). Similar observations would be possible with the XTI mode of Harmony. (Right) Map of surface elevation change (TOC m/yr) between 2000 (SRTM/X-SAR DEM) and 2012 (TanDEM-X) in the Karakoram High Asia from Kääb et al. (2018). These two examples for outlet glaciers of Antarctica and mountain glaciers of Himalaya shows the possibilities that would be offered on a much larger scale by Harmony with the XTI mode.

defined epochs. These measurements enable to derive average mass changes of glaciers over the lifetime of the mission (5 years) and therefore improve the global and regional estimates of their contribution to sea level rise, to run-off availability and to natural hazards as already demonstrated with single pass interferometric results from TanDEM-X (Rott et al., 2018; Rankl and Braun, 2016) (Figure 2.4). The new detailed dataset of surface elevation changes will also support the initialization and validation of numerical glacier models trying to hindcast and forecast the evolution of glaciers around the world (Mayer et al., 2018; Wendt et al., 2017; Marzeion et al., 2014, 2018). Over the ice sheets, the mission will focus on outlet glaciers and areas of complex topography, where the resolution of the altimeters (CryoSat-2, ICESat-2) limits our ability to resolve with enough details the current elevation changes. The improved observations of surface elevation changes near glacier termini or grounding lines will also benefit the estimates of ice flux discharging into the ocean by allowing to better correct for the ice dynamic thinning associated with the glacier acceleration. Both detailed ice volume changes and improved ice discharge will allow to further reduce uncertainties in mass balance estimates of the ice sheets. Harmony will also much facilitate partitioning of the mass loss between ice-dynamic and climatic processes, which both are the main drivers that need to be known to estimate the future evolution of the ice sheets.

2.3.2 *Flow dynamics of glaciers and ice sheets*

In addition to the long-term integrated adjustment to climate changes, we also observe rapid changes and highly dynamic responses of land-ice to external forcing. Glacier instabilities such as surges or glacier avalanches (Figure 2.4, which are amongst the most dramatic phenomena in the cryosphere, are expressions of such abrupt and potentially irreversible processes (Gilbert et al., 2018; Käab et al., 2018). Large seasonal fluctuations in ice dynamics have also been associated with significant dynamic thinning or thickening of tidewater glaciers (Joughin et al., 2020) and the physical mechanisms behind these large seasonal dynamic changes are potential keys to understand and project the long-term evolution of the affected glaciers. A number of fast glacier elevation changes observed are actually driven by changes in ice dynamics or instabilities on short time scales, rather than the often gradual climate-driven changes. Today, there is no sensor or mission available to perform simultaneous measurements of horizontal displacement and elevation change. Rather, such conclusions have today to be drawn from temporally often disconnected measurements of glacier flow and thickness change, whereby the main bottleneck stems in particular from the lack of elevations with a temporal repeat frequency in the same order as available for the ice flow.

The rate of ice flow is a fundamental characteristic of glaciers and ice-sheets that defines the speed at which ice is transported from areas of accumulation to areas of ablation, and how the ice mass is evolving with time. For the last decades, satellite SAR has been successfully used to map glacier flow independent of cloud cover, solar illumination, or the presence of surface features. The mapping of ice motion has redefined our view of glacier and ice sheet flow dynamics, with implications for improving reconstructions of past and ongoing changes and for modeling the evolution of ice sheet dynamics in a warming climate. However, with these observations at most two components of the displacement vector are measured, achieving a 3D solution only by assuming that the ice flows parallel to the surface (Joughin et al., 1998). This approach assumes that the ice flow is in equilibrium with the gravitational driving stress, precludes measuring any changes in surface slope and elevation that would come from changes

in basal drag or sub-glacial water distribution, and neglects vertical displacement associated with accumulation and ablation rates of the ice Gray (2011). This limits our representation of the global structure of the ice dynamics and how it may change in a warming climate..

2.3.2.1 Relevance and scientific impact

During each XTI observation phase, Harmony will be able to track simultaneously ice displacements and large elevation changes (in the order of several metres or tens of metres) by combining offset tracking based on repeat Sentinel-1 or Harmony SAR data and Harmony XTI-mode single-pass elevation models. The integration of measurements of lateral ice flow and simultaneous elevation changes holds a large potential to understand and predict fast glacier volume losses. In addition, the XTI mode would also have the advantage of providing the exact topographic component in range offset or phase, where current observations have to rely on external digital elevation models to compensate for topographic biases. As a result, the ice displacement measured through Harmony would be more accurate than from Sentinel-1 alone, reducing further the uncertainties in measuring ice flux discharge into the ocean, hence improving mass balance estimates from input/output methods (Rignot et al., 2019; Mougnot et al., 2019a; King et al., 2020).

For small (interferometrically coherent) flow rates, 3-D displacement measurements would be available from Harmony through the diversity in lines-of-sight offered by its SAR stereo mode or the XTI mode combined with the line of sight of Sentinel-1, together providing unique cm-precision 3D displacements by combining radar interferograms from ascending/descending passes. This would allow to overcome the limitation of current sensors that are used to derive the two horizontal components assuming surface parallel flow to derive the vertical one (Mougnot et al., 2019b). Precise 3-D measurements of ice surface deformation are crucial for instance for understanding and quantifying processes governing glacier hydraulics, effects of subglacial volcanism, and processes leading to sub- and intra-glacial water outbreaks (Gudmundsson et al., 2002; Magnússon et al., 2007, 2010). Succeeding in finally gaining access to the subsidence or emergence speed components of the ice flow would also give insight in the mean rates of accumulation and ablation. Such measurements would be very useful to constrain regional climate models that are used, for example, to estimate and refine the input flux of ice in mass balance exercises.

2.3.3 Sea ice deformation

A key feature of the sea ice is that it is constantly in motion because of the influence of wind and ocean currents. Reversibly, sea ice motion directly or indirectly controls the exchanges of heat, momentum and buoyancy fluxes within the ocean—sea ice—atmosphere system (Vihma, 2014). The state of internal stresses in the sea ice is the most variable of the different factors influencing its motion; it is very heterogeneous in space and intermittent in time (Thorndike and Colony, 1982) due to the brittle behavior of sea ice (Figure 2.5). The current methods for sea-ice drift and deformation retrieval utilize pairs of SAR images, or passive-microwave sources usually separated by days and/or with low resolution - up to tens of kilometers for passive-microwave sensors - (Curlander et al., 1985; Kwok et al., 1998, 2003; Lavergne et al., 2010; Karvonen, 2012; Howell et al., 2018; Tschudi et al., 2020). Consequently, it is only possible to derive sea-ice drift speed integrated over these time scales, therefore impairing our ability to describe properly the evolution of the internal stresses of sea ice at shorter time scales. Indeed, over such time scales sea ice is undergoing multiple

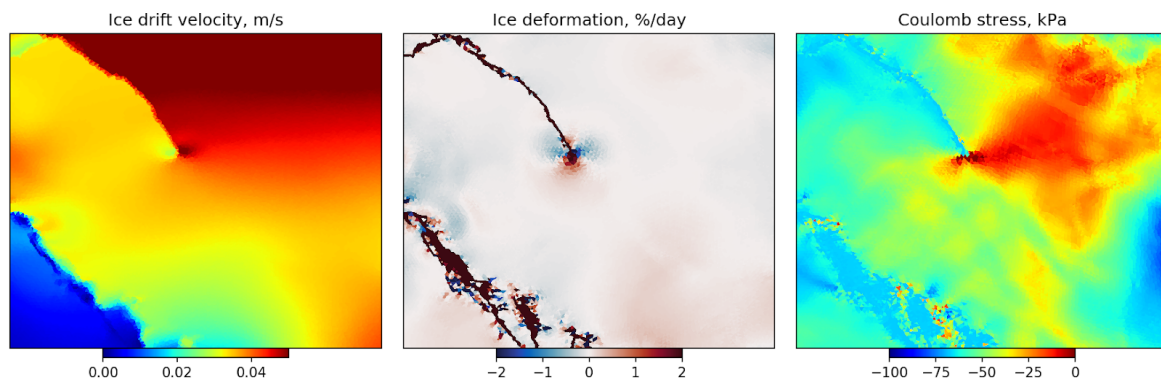


Figure 2.5: Expected instantaneous ice drift(left) and divergence (middle) and Coulomb stress (right) as simulated with (Rampal et al., 2016). For the first time, this would be directly observed with Harmony stereo mode configuration.

deformation events associated with the formation of multiple cracks and these events are not separable from each other. As a result, the underlying processes controlling this variability are not well understood yet, and as a consequence are poorly, or even not at all simulated in current state-of-the-art sea ice models. In other words, the sea-ice deformation, i.e. the sea-ice-cover break up and associated seismic activity, sea ice floe motion, divergence and convergence, is still to be better observed (Geiger and Drinkwater, 2001, 2005).

2.3.3.1 Relevance and scientific impact

Motion of sea ice is mainly driven by winds and ocean currents, but this relationship is complex and highly non-linear (Figure 2.5). Given that current observations are performed either on very small temporal and spatial scales (lab experiments) or on large scales (satellite observations integrated over days), the key science question is how to fill the gap in observation of spatially large features on very small time scales. Harmony in a stereo mode configuration will provide direct multi-directional Doppler velocity measurements, allowing for the retrieval of relative surface velocities, from which instantaneous ice drift and deformation can be derived. The major advantage compared to current observations would reside in the ability to observe the formation of individual fractures while they are being formed and to compute the associated fields of deformation. This unique ability of Harmony to provide instantaneous deformation measurements at high spatial resolution will allow direct calibration and validation of sea ice models. Indeed, models still need realistic rheology, where key parameters such as the Young modulus or Coulomb failure criterion are precisely characterized, in order to simulate realistically the propagation of fractures in pack ice. As already pointed, this is obviously not achievable with the existing observations of sea ice and would be a major contribution from Harmony.

2.3.4 Subsidence and erosion in permafrost areas

Similar to other shrinking components of the cryosphere, permafrost is subject to extensive thaw and degradation in a warming Arctic (IPCC Special Report on the Ocean and Cryosphere in a Changing Climate). Critical feedbacks from carbon emissions from thawing soil to the global carbon cycle are expected (Romanovsky et al., 2010; Schuur et al., 2015; Biskaborn et al., 2019). Seasonal vertical changes in the order of cm to dm reflect the annual freeze-

thaw cycle within the permafrost active layer, while interannual changes in the same order of magnitude, in particular over several years, can indicate subsidence due to ground ice loss. Based on repeat XTI-mode elevations, the Harmony mission will be able to provide data on the spatial distribution, extent, magnitude, and rates of abrupt permafrost thaw associated with rapid subsidence, thermokarst, or erosion across the global permafrost regions. No satellite mission is currently capable of delivering this critical information with the required spatial and temporal coverage. Further, traditional repeat-pass interferometry measures line-of-sight displacements and has in case of permafrost typically to assume that the observed displacement stems from vertical thaw subsidence or frost heave.

2.3.4.1 Relevance and scientific impact

Harmony will, for the first time, enable us to quantify both the vertical and the lateral components of seasonal and long-term subsidence, and thus to understand landscape-scale influences of topography on permafrost dynamics.

2.4 Solid Earth

Spatially-detailed maps of 3-D surface displacements and topography change, and their temporal evolution, are essential for understanding and modelling geophysical processes that trigger earthquakes and volcanic events, and for the assessment of hazards arising from these phenomena. Current SAR missions are sensitive to vertical and east-west motions, but are extremely limited in their sensitivity to north-south motion. The Harmony mission will deliver 3-D vectors of surface motion by means of differential repeat-pass InSAR methods. In areas where displacement is predominantly north-south, the ability to systematically measure the third dimension of displacement will reveal motions that have been invisible up until now, and in other areas will enable to resolve ambiguities in the underlying physical processes that lead to earthquakes and volcanism. In its cross-track configuration, the Harmony mission will deliver time series of topographic change, providing high resolution views of the active processes that reshape the Earth's surface.

2.4.1 Earthquakes and Volcanoes

Surface displacement maps are an essential component for understanding and modelling the tectonic processes that lead to earthquakes, and for assessing the associated seismic hazard. InSAR applied to Sentinel-1 data can already provide east-west velocities at high resolution, but the data are extremely limited in their sensitivity to north-south motion. In the case of an east-west trending strike-slip fault, InSAR allows motion due to strain build up along the fault to be almost fully imaged (Figure 2.6c). The strain rate can then be extracted with high resolution (Figure 2.7c), which can be fed into models of seismic hazard. For a north-south trending fault, however, the north-south motion cannot be extracted at high resolution using InSAR. At best, the recovered velocity and strain rate is equivalent to that from using GNSS only for an east-west fault (Figure 2.6b and Figure 2.7b), but for the majority of regions with sparser GNSS networks, the recovered velocity and strain rate is even worse.

Traditional approaches for estimating seismic hazard are based on statistical analyses of historical and instrumental catalogues of earthquakes. This approach is fundamentally limited for most continental active tectonic regions, where the average recurrence interval for earthquakes is longer than the historical record. However, earthquakes occur where stress builds up, and strain rate serves as a proxy for stress accumulation. Therefore by measuring 3-D

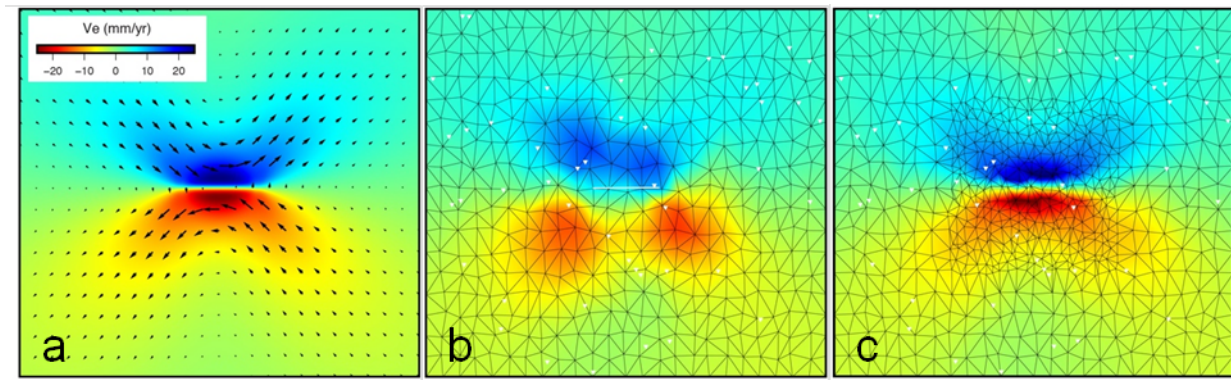


Figure 2.6: Simulations of recovered velocity for an east-west strike-slip fault. a, synthesised velocity, b, recovered velocity using GNSS only and c, recovered velocity using GNSS and InSAR.

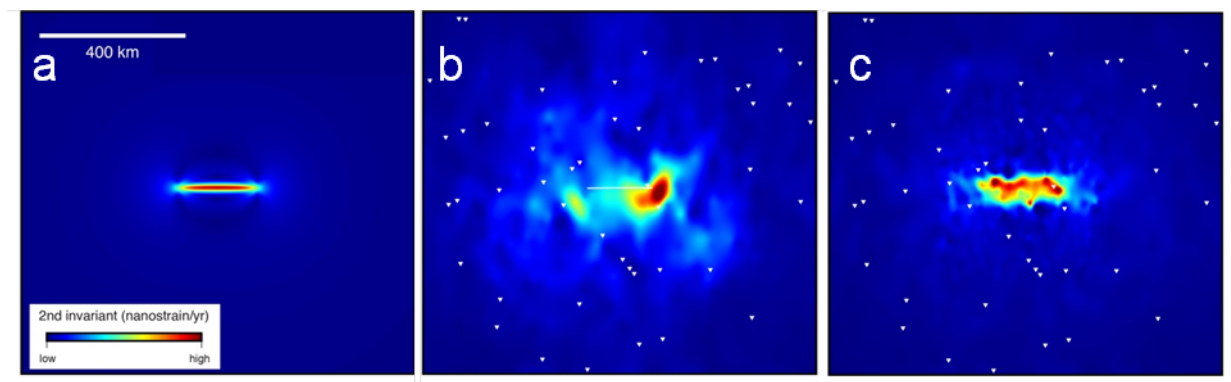


Figure 2.7: Simulations of recovered strain rate for an east-west strike-slip fault. a, synthesised strain rate, b, recovered strain rate using GNSS only and c, recovered strain rate using GNSS and InSAR.

velocity everywhere, we can calculate strain rates and forecast where earthquakes will occur (Elliott et al., 2016). The vast majority (96%) of all earthquake deaths occur in regions with strain rates greater than 10^{-8} per year. Measuring strain rates with this level of accuracy equates to 3-D velocity estimation with an accuracy of 1 mm/year between points 100 km apart.

Volcanic eruptions are typically preceded by a period of unrest and monitoring data is essential for assessing the threat to local populations which may need to be evacuated. Maps of surface displacement and topographic change are vital for understanding the geometry and activity of underlying magma storage areas and the stability of steep volcanic edifices. Combining eruption volumes with subsurface volume changes determined from deformation measurements has implications for the comprehensibility of magma – a critical yet elusive physical parameter that can provide insights into the volatile content of the melt (Mastin et al., 2009). At many volcanoes, deformation is offset from the edifice or associated with rift zones or sector collapses and consequently may be asymmetrical (Ebmeier et al., 2018). Currently, while the spatial coverage of InSAR is advantageous compared to the low spatial

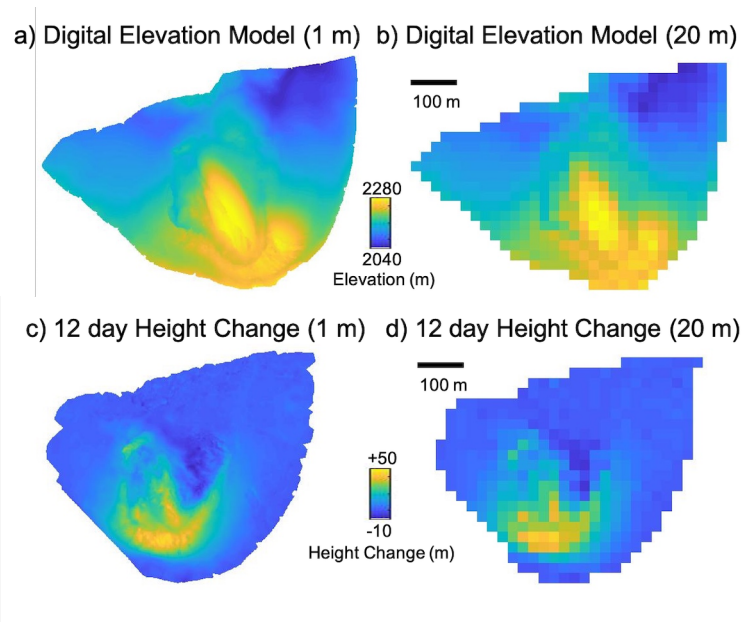


Figure 2.8: Simulations of recovered topographic change using the 2004 dome growth at Mt St Helens to illustrate. a, Digital surface model (DSM) from aerial photogrammetry; b, recovered DSM; c, 12 day topographic change from aerial photogrammetry; d, recovered topographic change.

resolution of terrestrial GNSS networks, information from a single line-of-sight may lead to incorrect conclusions about the depth and geometry of magma storage (Lundgren et al., 2017; Wicks et al., 2011). The infrequent acquisition of suitable satellite images means that eruption volumes are often estimated from just a few field locations rather than mapped comprehensively, and time-series of topographic changes are only available at a handful of volcanoes (e.g. Figure 2.8a,c).

2.4.1.1 Relevance and scientific impact

The Harmony mission will deliver 3D vectors of surface motion, allowing us to study areas where motion is predominantly north-south, which includes regions around north-south trending strike-slip faults and east-west trending dip-slip faults and rift zones. Until now the third dimension of displacement has been invisible. Constraints from Sentinel-1 for east-west motion will allow us to image strain-rates for only 43% of regions straining at 10^{-8} per year (Figure 2.9). The addition of the north-south constraint from Harmony will allow the remaining 57% to also be imaged, leading to global estimates of seismic hazard. The north-south component of motion will also be vital for understanding asymmetrical patterns of magma storage, such as the east-west rift zones at Agung, Indonesia and Kilauea, Hawaii, where major evacuations have taken place in recent years.

In its cross-track configuration, Harmony will provide high-temporal-resolution views of topographic change and yearly DSM updates at actively erupting volcanoes, of which there are several dozen around the world at any given time. Measuring topographic change over time will provide new constraints on eruption rates which can be used to forecast the behaviour of an ongoing eruption. Updated DSM information can be used to measure the growth and

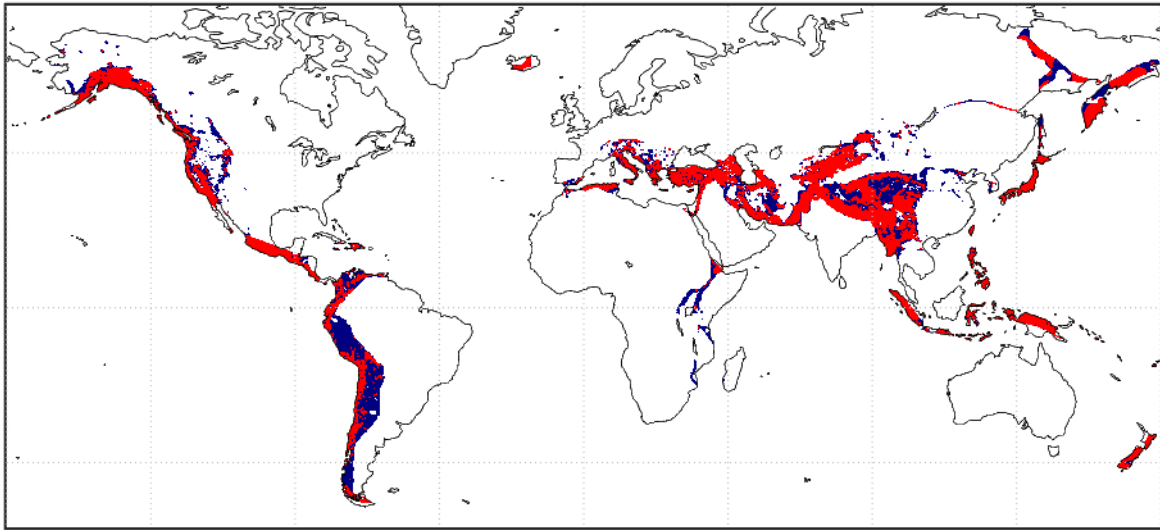


Figure 2.9: Coloured areas show regions straining at greater than 10 nanostrain per year. Blue regions are those that have a small component of north-south strain and can be imaged by Sentinel-1 alone. Red regions indicate the extra area that will be constrained by Harmony.

collapse of volcanic domes (Figure 2.8b,d) and improve modelling of the potential paths and inundation areas of hazardous mass flows (primarily lava, pyroclastic density currents, and lahars).

3 MISSION OBJECTIVES

3.1 Scientific goals

Harmony's scientific goals have been mapped to the Living Planet (LP) Challenges following their definition in (SP-1329/2). The reader is referred to this document to take note of the formulation of these broadly defined scientific challenges for Earth observation.

Oceans, atmosphere, and air-sea interactions

Presently, and in the foreseeable future, the choice of grid resolution for the ocean in Earth System Models and the way unresolved processes are modeled are, and will remain, a major source of uncertainty in model projections and even in the quantification of the uncertainty. For Earth System Models, efforts particularly strive to increase the ocean resolution and to improve the parameterisation of unresolved complex processes with enhanced fidelity. The overarching goal of combined Harmony measurements is to provide the high-resolution observations urgently needed to drive these developments. Harmony will thus provide kilometer-scale surface roughness, root mean squared slopes, and surface kinematics, in different viewing perspectives, reflecting the imprint of MABL eddies on the ocean surface. This provides information about both the surface wind vector, as well as (Total) Surface Current Velocity vectors (SCV) and swell, and, importantly, the thermal disequilibrium between air and ocean. Hence, Harmony will lead to a more precise understanding of small-scale (submesoscale) impacts on air-sea fluxes, especially CO₂ fluxes, momentum, ocean heat uptake and overall energy pathways, to reduce uncertainties for lateral dispersion of pollutants and tracers, vertical transport and nutrient pumping. Specifically, Harmony's very high-resolution capabilities aim at:

- H-O1** Quantifying and disentangling sub-mesoscale effects, i.e., the air-sea interactions and adjustment between ocean features (e.g., fronts and eddies) and the MABL and troposphere under different environmental conditions (Western boundary current systems, Eastern boundary upwelling systems, coastal and/or marginal ice zones), to consolidate empirical parameterisations, targeting momentum and heat exchanges and CO₂ fluxes, leading to precise data-driven representations of these processes in new generation Earth System Models. *This science goal contributes to LP Challenge O4.*
- H-O2** Improving the prediction of the evolution of tropical and intense extratropical cyclones (notably, rapid intensification events), as well as evaluating the feedbacks between these extreme weather events and the upper ocean state. *This science goal contributes to LP Challenge O5.*
- H-O3** Resolving the high-latitude small mesoscale ocean surface dynamics and quantify the submesoscale surface current gradients over all latitudes and seasons, i.e., the upper ocean deformation, with the divergences and associated local vertical velocities in the upper ocean, strains and vorticities down to O(1-5 km) horizontal resolution, to understand their contribution to ocean circulation, upper ocean ventilation, ocean heat uptake, CO₂ sequestration and related vertical ocean transport processes, and to develop data-driven downscaling parameterisations. *This science goal contributes to LP Challenge O2.*

Dynamical changes in the Cryosphere

The scientific goal of Harmony for the cryosphere is to bridge existing observational gaps in order to improve our understanding of the physical processes causing the widespread shrinkage of the cryosphere. These conceptually new observations will push back the existing limits by refining the reconstructions of past and ongoing glacier changes, by improving the representation of the driving mechanisms in regional and global models of ice flow dynamics and mass balance, by describing the unresolved complex processes allowing calibration and validation of sea ice models with more realistic rheology or by improving our understanding of the permafrost dynamics.

Harmony aims at providing, for the first time, worldwide integrated measurements of elevation changes and ice flow on glaciers and ice-sheet coastal areas, as well as localised elevation measurements of icebergs and ice shelves. To date, no such measurements exist from space but have to be synthesised from different data sources, with different characteristics, spatial resolutions and coverages, and time stamps. Availability of such simultaneous measurements of 3-D surface changes, combined with Harmony's other mission characteristics, will overcome a number of current deficiencies in monitoring and understanding glaciers and ice sheets. It is a particular strength of the interferometric capabilities of Harmony that the mission is able to measure large topographic changes and lateral displacements (scale of metres and tens of metres) through repeat XTI-mode elevation models and SAR offset tracking, and, at the same time, small changes (cm-scale) thanks to the diversity of SAR lines-of-sight.

Harmony will provide direct measurements of relative surface velocities, from which instantaneous ice drift and deformation can be derived. These new observations will allow to improve state-of-the-art sea ice models.

The Harmony primary scientific goals regarding cryosphere are:

H-C1 Providing a consistent and highly resolved global glacier mass balance, filling major spatial gaps in the current observation of mountain glaciers and outlet glaciers of the ice sheets. *This science goal contributes to LP Challenge C2 and relates to climate change and sea-level rise in LP Challenge O5.*

H-C2 Give new insight on the physical processes associated with the coupling between glacier mass change and ice dynamics. Through that, substantially improve understanding and prediction of rapid or even abrupt glacier changes, and the balance between vertical ice flow and mass accumulation/ablation. *This science goal also contributes to LP Challenge C2.*

Further secondary goals regarding cryosphere are:

H-C3 Provide measurements of instantaneous sea-ice velocities providing missing constraints on the sea ice dynamics and rheology in order to improve their missing representation in numerical models. *This science goal contributes to LP Challenge C1.*

H-C4 Provide crucial large-area information on the spatial distribution, extent and magnitude of subsidence and erosion in permafrost areas in order to estimate permafrost degradation and its local and global impact. *This science goal contributes to LP Challenge C5.*

Solid Earth

Harmony aims to provide an integrated view of the dynamic processes that shape the Earth's surface. For the Solid Earth, the scientific goals are to improve our understanding of tectonic and magmatic processes by bridging existing observational gaps, i.e.,

1. Current missions are only able to measure strain rates for less than half of the tectonic areas and provide incomplete imaging for earthquakes in certain orientations. The ability to measure the N-S component of deformation will complete this map and hence improve global estimates of seismic hazard;
2. Measurements of the spatial distribution of elevation changes associated with actively erupting volcanoes (e.g. dome growth, flow deposition) are currently rare, particularly over steep volcanic edifices. Elevation time-series data are critical for calibrating and validating process models and forecasting the associated hazards.

The unique interferometric capabilities of Harmony will enable it to measure the 3-D strain field (mm/yr-scale displacements) using the diversity of lines-of-sight and also measure large topographic changes (1-10 m-scale elevation changes) in repeat cross-track mode. Together these abilities will allow us to improve our understanding of the processes that drive earthquakes and volcanoes and ultimately improve hazard management.

H-G1 Map all components of global tectonic strain and the deformation caused by volcanism and the earthquake cycle. These measurements are required to constrain the geometry and nature of the driving processes and improve forecasts of the associated geohazards. *This science goal contributes to LP Challenge G1.*

H-G2 To understand cycles of topographic growth, mass transport and collapse at actively erupting volcanoes and improve forecasts of the associated geohazards. *This science goal contributes to LP Challenge G2.*

3.2 Mission objectives

Whereas scientific goals as expressed in Section 3.1 are related to broad scientific challenges or questions – e.g. as defined in a strategy document –, mission objectives are related to the mission itself and traceable to the scientific goal(s). In general, mission objectives can be achieved by using primarily data from the mission with limited use of (retrieval) models and auxiliary data files during the mission life time. A mission objective can be related to a data product at Level 1, 2, or 3 and shall be achieved in Phases E1 or E2 (SRL 7 & 8). Table 3.1 provides Harmony's mission objectives with a clear mapping to the scientific goals as discussed in Section 3.1, with *P* or *S* to distinguish primary from secondary objectives and a unique identifier to allow for easy referencing in the flow-down of these objectives.

Table 3.1: Harmony primary and secondary mission objectives.

Objectives	Priority	ID
Ocean		
Air-Sea Interactions (H-O1)		
Extend the knowledge of the 2D co-spectra of surface stress, surface wind, surface currents, and SST from the scatterometer scale (25km) down to O(1km) scales, covering all relevant conditions at the sea surface and in the MABL.	P	OBJ-O11
Quantify the contribution of small scale processes (down to O(1 km) scales) to the air-sea fluxes of gas (CO ₂), momentum, and heat.	P	OBJ-O12
Quantify the vertical fluxes (momentum and buoyancy) within the MABL at 1km horizontal scale.	P	OBJ-O13
Marine-Atmosphere Extremes (H-O2)		
Measure surface stress equivalent wind vectors at 1 km scale in extreme wind conditions, to estimate inflow convergence toward the low pressure center and vorticity perturbations embedded in the cyclonic flow.	P	OBJ-O21
Retrieve directional wave spectra and simultaneous near inertial currents at 5-10km resolution, during all phases (ahead, during, and in the wake) of the passage of the extreme weather event.	P	OBJ-O22
Small-scale upper ocean dynamics (H-O3)		
Extend the knowledge of the ocean surface motion power spectrum from currently resolved mesoscales (O(50km)) down to submesoscales (O(1-10km)), capturing the regional variability and the seasonal cycle.	P	OBJ-O31
Quantify the vorticity and flow divergence in the upper ocean at O(1km) horizontal scale, to estimate the vertical transport of nutrients, heat and, gas across the ocean boundary layer.	P	OBJ-O32
Cryosphere		
Land Ice (H-C1,H-C2)		
Quantify multi-year average elevation change for most glaciers and ice sheet outlets, with a high spatial resolution of at least 100m, and sub-meter accuracy.	P	OBJ-C11
Providing (i) elevation change, at high spatial resolution of at least 100 m, at sub-seasonal time-scale, and with vertical accuracy of 5m or better, together with (ii) simultaneously-acquired SAR data from which horizontal displacements can be derived.	P	OBJ-C21
Monitor 3-D surface motion and deformation of glaciers and ice streams.	S	OBJ-C22
Permafrost (H-C4)		
Quantify the extent, magnitude, and rates of rapid thaw subsidence and erosion of permafrost, at multi-annual time scale, at high spatial resolution of at least 100m, and with sub-meter vertical accuracy.	S	OBJ-C41



Solid Earth		
Tectonic Strain (H-G1)		
Measure 3-D surface motions in tectonic regions with an uncertainty lower than 1 mm/yr over a distance of 100 km.	P	OBJ-G11
Provide measurements of N-S surface motions associated with earthquakes, volcanoes and landslides around the world at a spatial resolution of 100 x 100 m ² .	S	OBJ-G21
Volcanoes (H-G2)		
Provide measurements of topographic change at actively erupting volcanoes with a spatial resolution of 20 x 20 m ² .	S	OBJ-G12

4 MISSION REQUIREMENTS

This chapter outlines the mission requirements, through providing quantitative descriptions and justification, including prioritisation, of the Level 2 geophysical requirements that would allow to fulfil the mission objectives. A synoptic presentation of mission requirements at system level will be given first – due to its global applicability. Following this, the product flow-down will be presented including Level-1 and -2 product definitions, as this approach best allows for a logical grouping of requirements. Finally, mission requirements for ocean and air-sea interactions, cryosphere and solid Earth are provided, respectively.

4.1 Mission requirements at system level

The Harmony mission, comprised of two companion satellites, shall fly in a loose convoy with Sentinel-1. For Harmony, two different configurations shall be foreseen:

1. A “stereo-phase” optimised for the measurement of motion vectors, where each Harmony satellite is positioned on either side in the along-track direction of Sentinel-1. The separation distance between each of the Harmony satellites to Sentinel-1 is in the order of 100’s of km and to be optimised for performance.
2. A formation flight between the Harmony satellites during a XTI phase optimised for the measurement of time-series of surface topography, where one of the Harmony satellites will be positioned in a close formation with the other Harmony satellite. Also in this phase, the along-track separation distance between the XTI-formation of the Harmony satellites to Sentinel-1 will remain in the order of 100’s of km.

A nominal mission lifetime of 5 years would sufficiently cover Harmony’s mission objectives as it allows to accommodate the following operational sub-phasing of the mission, i.e.:

1. A close-formation-phase focused on XTI lasting at least one year and starting at the beginning of the scientific exploitation of the mission.
2. A stereo-phase focused on ocean and surface deformation observations lasting at least two consecutive years, with allowance for occasional XTI observations.
3. A close-formation-phase focused on XTI during the last year of nominal operations of the mission.

Harmony shall be capable of switching in and out of XTI configuration at least twice per year during the stereo phase in order to allow for some flexibility in the operations of the mission.

Each Harmony satellite shall embark a passive SAR and a multi-view TIR payload. The passive SARs on-board the two companion satellites shall be able to acquire data from all Sentinel-1 sub-swaths, when Sentinel-1 is operating in any of the following modes: Stripmap Mode (SM), Sentinel-1 Interferometric Wide swath mode (IW), Sentinel-1 Extra Wide swath mode (EW) and Sentinel-1 Wave mode (WV). The passive SARs on-board the two companion satellites shall acquire two orthogonal polarisations simultaneously. The swath of the multi-view TIR instrument shall cover, for each separate view, at least that of the SAR Wave mode in the sense that the inner side of the innermost vignette to the furthest side of the outermost vignette shall be observed by the TIR instrument contiguously.

4.2 Mission requirement flow-down approach

Figure 4.1 provides the Phase-0 requirement flow-down approach and processing flows using a product analogy. The boxes can be interpreted as products or logical groupings of requirements. All acronyms appearing in the boxes are explained in Table 4.2, Table 4.1, Table 4.8 and Table 4.7.

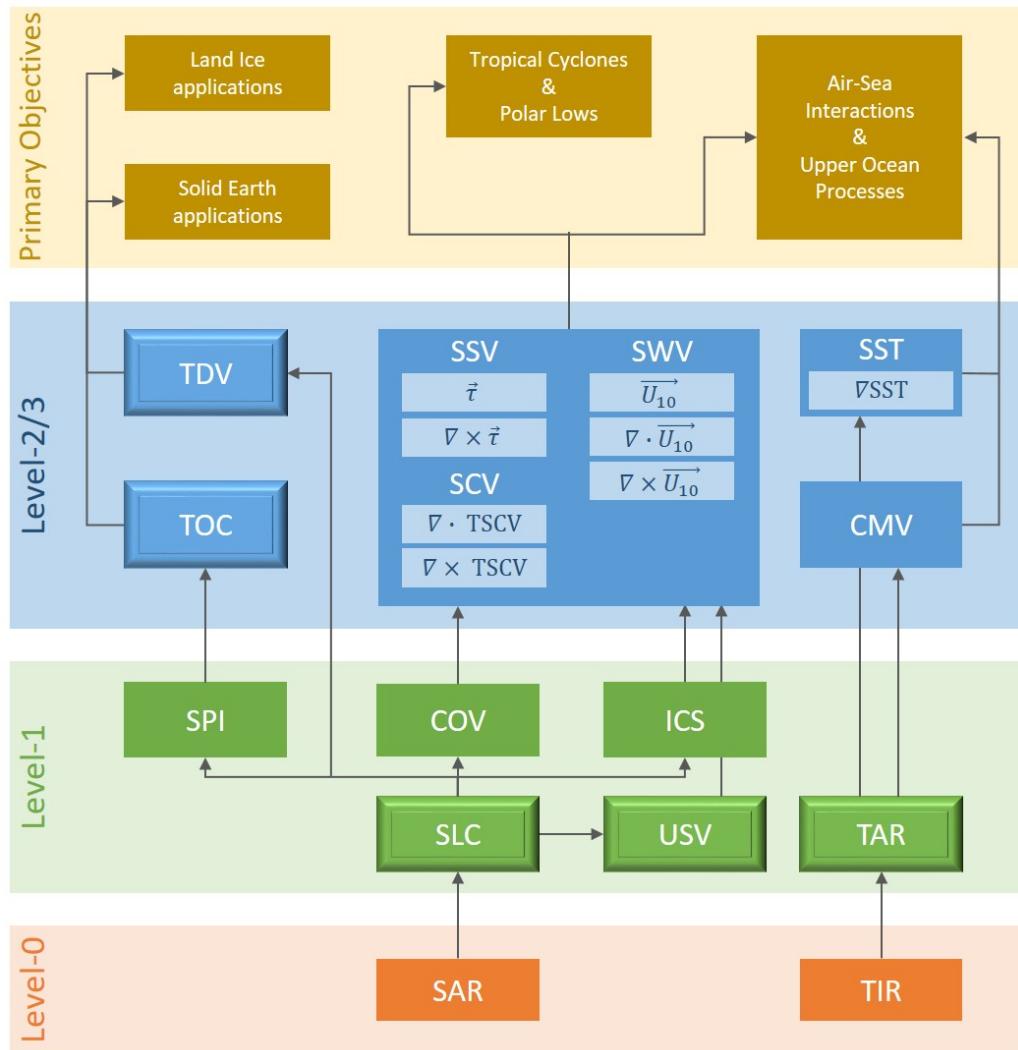


Figure 4.1: Harmony product flow chart, connecting the SAR and TIR instruments to the primary science objectives. Upward arrows represent processing flows. The downward direction represents requirement flow-down.

The following sections will detail the envisaged flow, product definitions and requirement specifications for each thematic area. Requirements have the following attributes:

- Priority: G(oal), N(ominal), T(hreshold)
- Level: L1, L2, L3
- ID: Unique identifier

Nominal is used when there is a single specification to reach compliance; *Threshold* specifies the minimum condition to reach compliance; *Goal* reflects the intended performance.

4.3 Ocean and air-sea interaction

From the product flow for ocean and air-sea interactions in Figure 4.1, the mission shall be able to generate the products as described in Table 4.1.

Table 4.1: Level-2 products definition for ocean & air-sea interaction.

Short name	Long name	Description
SSV	Surface Stress Vectors	The wind stress τ is the shear stress exerted by the wind on the surface of large bodies of water - such as oceans, seas, estuaries and lakes. It is the force component parallel to the surface, per unit area, as applied by the wind on the water surface. The product contains the stress vector field τ and its curl.
SWV	Surface Wind Vectors	Stress-equivalent Vector Winds at 10m altitude from the ocean surface (U10S). The product contains the horizontal 2D wind vector field U10S, as well as its divergence and vorticity.
SCV	Total Surface Current Vectors	Ocean surface currents are the coherent horizontal movement of surface ocean water over a specified integration depth with a given velocity and an upper boundary in contact with the atmosphere. Geophysical processes governing surface flow include wind drift, Stokes drift velocity, Ekman transport, tides, geostrophic and ageostrophic flows. The Total Surface Current Vector (TSCV) is the vectorial representation of the surface velocity and characterised by a magnitude and direction. It is independent of any geophysical or non-geophysical measurement bias due to the observation system. The SCV product contains the TSCV vector field, as well as its divergence and vorticity.
CMV	Cloud Motion Vectors	This is a point-cloud like product, with 3-D velocity vectors associated to 3-D positions derived from cloud tracking and multi-angle retrievals.
SST	Sea Surface Temperature	Sea surface temperature (SST) is the water temperature at the surface of the ocean. For Harmony the quantity of interest is the gradient of this temperature.

In order to generate those products at Level-2, Table 4.2 provides the required products at Level-1.

Table 4.2: Level-1 products definition for ocean & air-sea interaction.

Short name	Long name	Description
TAR	Top of Atmosphere Radiance	Top of Atmosphere (TOA) brightness temperatures (K) in the infra-red channels.
SLC	Single Look Complex	Single Look Complex images are SAR products in which each pixel is represented by a complex (I and Q) value and therefore contains both amplitude and phase information. The processing for all SLC products results in a single look in each dimension using the full available signal bandwidth. They contain two orthogonal polarisations. The data is radiometrically calibrated and synchronisation errors have been corrected.
ICS	Image Cross Spectra	Estimated cross-spectra of inter-looked SLC images in the azimuth direction.
COV	Covariance matrices of NRCS	The COV product contains the backscatter data, including the non-zero elements of the covariance matrix of the signals received in the 2 polarisation channels of both Harmony's and Sentinel-1.
USV	Geophysical equivalent surface velocity	The geophysical equivalent surface velocity vector is the mean surface velocity of the scatterers in a resolution cell, as measured in an Earth fixed, Earth centered reference frame, and projected on the WGS-84 ellipsoid. It is obtained as: $USV = UDOP - UNG$. Systematic errors due to pointing uncertainties, synchronization errors, etc, have been corrected. Residual uncertainties are annotated. This product will include geophysical biases such as wave bias. The USV product contains two components of the surface velocity vector.

The definition for USV makes use of the definitions stated in Table 4.3.

Table 4.3: Definitions of terms used in Level-1 products.

Short name	Long name	Description
UDOP	Doppler surface velocity	The Doppler surface velocity vector is the mean surface velocity of the scatterers in a resolution cell, as measured by the radar in the antenna reference frame, and projected on the WGS-84 ellipsoid.
UNG	Non-moving surface Doppler velocity	The non moving surface Doppler velocity vector UNG is the Doppler surface velocity projected on the WGS-84 ellipsoid for a target fixed on the Earth surface, taking into account the satellite position and velocity, the viewing geometry, and the solid earth motion.

Using the definitions listed in Table 4.2 and 4.1, Table 4.4 provides the mission requirement specification at Level-2 for ocean & air-sea interaction. Coverage and revisit requirements are listed in Table 4.5. Regarding Level-1 (L1), ICS and COV are intermediate products and as such can be seen as functional elements in the flow-down logic. USV requirements are

directly flown-down from SCV requirements. Requirements for TAR are specific low-level requirements tied to the instrument specifications and have therefore been listed separately in Table 4.6.

Table 4.4: Requirement specification for ocean & air-sea interaction.

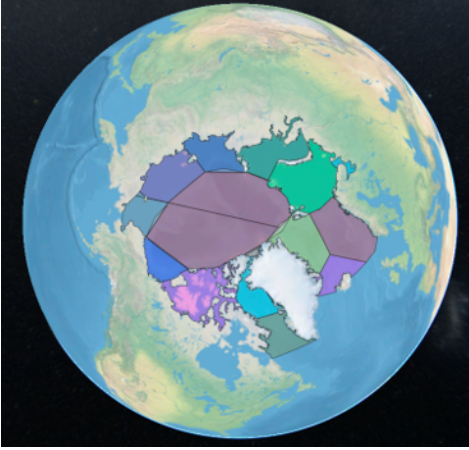
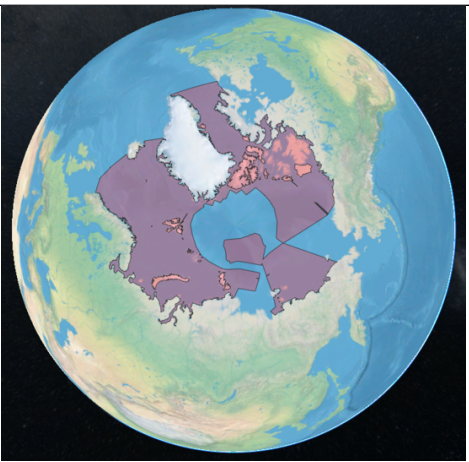
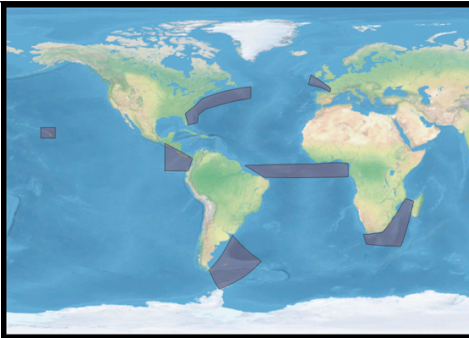
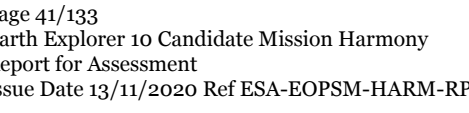
Requirement	Priority	Level	ID
SSV requirements for air-sea interactions	N		PP-130
The Mission shall observe Surface Stress Vectors (τ) with a horizontal resolution of 1 km ² <i>Note 1: this resolution is set by OBJ-O11</i>	N	L2	PP-423
SWV requirements for air-sea interactions	N		PP-122
The Mission shall observe U10S with a horizontal resolution of 1 km ² <i>Note 1: this resolution is set by OBJ-O12 and OBJ-O13 and is required to, for example, resolve OLEs.</i>	N	L2	PP-125
The Mission shall observe U10S over the range 3 m/s to 50 m/s and directional range 0-360°.	N	L2	PP-126
The Mission shall support the estimation of both vector components of U10S to an accuracy <1 m/s or 7.5%, whichever is larger. <i>Note 1: this provides sufficient sensitivity to resolve U10S variations associated to OLEs.</i>	N	L2	PP-127
SCV requirements for air-sea interactions	N		PP-121
In low-wind conditions, the Mission shall observe TSCV with a horizontal resolution better than 25 km ² .	N	L2	PP-218
In high-wind conditions, the Mission shall observe TSCV with a horizontal resolution better than 5 km ² . <i>Note 1: This requirement is driven by OBJ-O31.</i> <i>Note 2: Like other resolution requirements, this needs to be combined with the corresponding sensitivity requirement, PP-222. Resolution and sensitivity can in practice be traded for each other.</i>	N	L2	PP-219
The Mission shall observe TSCV over the range of 0 to 5 m/s.	N	L2	PP-220
In low-wind conditions, the Mission shall observe TSCV with a relative performance error of <0.20 m/s for both the along-track and across-track components over an area of interest of 50km x 50km.	N	L2	PP-221
In high-wind conditions, the Mission shall observe TSCV with a relative performance error of <0.1 m/s for both the along-track and across-track components over an area of interest of 50km x 50km. <i>Note 1: RPE is driven by observed small-scale variability in model outputs.</i> <i>Note 2: Resolution and sensitivity (here expressed as RPE) can in practice be traded for each other.</i>	N	L2	PP-222

<p>The Mission shall observe TSCV with an absolute performance error of <25 cm/s for both the along-track and across-track components.</p> <p><i>Note 1: drivers for this requirement the correction of the TSCV in the conversion of Surface Stress Vectors (SSV) to Surface Wind Vectors (SWV), as an absolute SCV errors translates directly into an equal SWV error.</i></p>	N	L2	PP-223
<p>CMV requirements for air-sea interactions</p>	N		PP-203
<p>Cloud Motion Vectors shall be understood to be 3D motion vectors at or near cloud tops.</p> <p><i>Note 1: Cloud-top height retrieval, which is necessary to position the CMV data in 3-D space to deliver a point-cloud like product, is a part of the CMV retrieval process.</i></p> <p><i>Note 2: CMV requirements are driven by OBJ-012 & OBJ-013.</i></p>	N		PP-205
<p>Individual CMV measurements shall be height registered with an accuracy of 500 m.</p> <p><i>Note 1: this accuracy requirement is corresponding to each point in the retrieved point-cloud, not the overall height field.</i></p> <p><i>Note 2: The ability to position the top of the cloud-layer, and to some extent its vertical structure, will depend on the density of cloud-top points.</i></p>	N		PP-206
<p>The mission shall support the estimation of CMV with an accuracy of the horizontal u and v components of better than 1 m/s.</p>	N		PP-207
<p>The mission shall support the estimation of CMV with an accuracy of the vertical component of better than 3 m/s.</p>	N		PP-208
<p>The mission shall support the estimation of CMV with a horizontal resolution better than 1.5 km.</p>	G		PP-209
<p>The mission shall support the estimation of CMV with a horizontal resolution better than 2.25 km.</p>	T		PP-210
<p>SST requirements for air-sea interactions</p>	N		PP-112
<p>The SST product shall include cloud flags wherever the SST performance requirements cannot be met due to cloud cover.</p>	N	L2	PP-115
<p>The Mission shall observe SST at a horizontal resolution of 1 km².</p> <p><i>Note 1: This requirement is driven by OBJ-011.</i></p>	N	L2	PP-116
<p>The Mission shall observe SST over the range 230K to 305K.</p>	N	L2	PP-117
<p>The Mission shall observe SST with a relative performance error of 0.25 K over distances of 50 km.</p> <p><i>Note 1: The purpose of the requirement is to constrain in a relative sense the SST retrievals, so that SST structures can be observed, without the need of doing this on an absolute scale.</i></p> <p><i>Note 2: The Relative Performance Error (RPE) shall be achieved for each spatial sample.</i></p>	N	L2	PP-118

The mission shall observe the gradient of SST with an absolute performance error of better than 0.25K per 50 km. <i>Note 1: To be interpreted as the difference between the means of the performance error taken over two areas within a single observation.</i> <i>Note 2: For each area a size up to 15x15 km may be assumed for allowing sufficient radiometric noise reduction.</i>	N		PP-442
SWV requirements for cyclones	N		PP-90
The Mission shall observe U10S with a horizontal resolution of 1 km ² <i>Note 1: This requirement is driven by OBJ-021.</i>	N	L2	PP-173
The Mission shall observe U10S over the range 3 m/s to 50 m/s and directional range 0-360 deg.	N	L2	PP-174
The Mission shall observe both U10S components to an accuracy <1 m/s or 7.5%, whichever is larger.	N	L2	PP-175
CMV requirements for cyclones	G		PP-152
Cloud Motion Vectors (CMV) shall be understood to be 3D motion vectors near cloud tops.	G	L2	PP-169
CMVs shall be height registered with an accuracy of 500 m.	G	L2	PP-202
The mission shall support the estimation of CMV with an accuracy of the horizontal u and v components of better than 3 m/s.	G	L2	PP-165
The mission shall support the estimation of CMV with an accuracy of the vertical component of better than 2 m/s.	G	L2	PP-166
The mission shall support the estimation of CMV with a horizontal resolution better than 1.5 km.	G	L2	PP-167

Table 4.5: Coverage and revisit requirements for ocean & air-sea interactions

Requirement	Priority	Level	ID
Coverage and revisit requirements for air-sea interactions	N		PP-106
The mission shall produce air-sea interaction products in the Arctic ocean, with a coverage as defined by the Polar Arctic Ocean Region of Interest (RoI) mask in PP-467. <i>Note 1: Here coverage is defined as full wall-to-wall coverage, in imaging mode.</i>	G	L2	PP-107

				
<p>The mission shall produce air-sea interaction products in the Arctic ocean, with a coverage as defined by the mask in PP-472, which is the intersection of the Polar Arctic Ocean RoI mask with the areas covered by S1, according to the Sentinel-1 reference scenario defined in (ESA, 2020).</p> <p><i>Note 1: Here coverage is defined as full wall-to-wall coverage, in imaging mode.</i></p>		G	L2	PP-107
				
<p>The mission shall produce air-sea interaction products over ocean current Regions of Interest (RoI), with a coverage as defined by the Current System RoI mask in PP-468.</p> <p><i>Note 1: Here coverage is defined as full wall-to-wall coverage, in imaging mode.</i></p>		T	L2	PP-469
				
<p>The mission shall produce air-sea interaction products over ocean current Regions of Interest (RoI), with a coverage as defined by the Current System RoI mask in PP-468.</p> <p><i>Note 1: Here coverage is defined as full wall-to-wall coverage, in imaging mode.</i></p>		N		PP-470
				
		N		PP-468

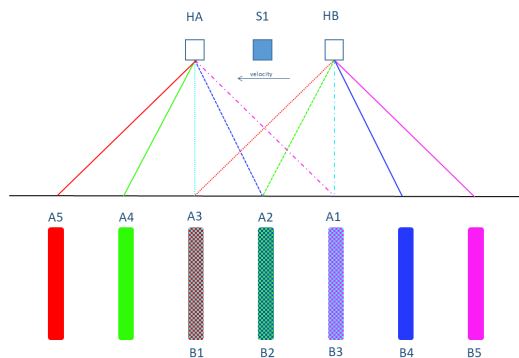
The mission shall produce globally sampled air-sea interaction products with wave mode coverage.	N	L2	PP-213
The mission shall produce air-sea interaction products with a longitudinal mean revisit better than 2 days, over the current system RoI as defined by PP-107.	G	L2	PP-214
In the Polar Arctic Region, as defined in PP-469, the mission shall produce air-sea interaction products with a revisit as good as Sentinel-1. <i>Note 1: The Sentinel-1 reference scenario as defined in (ESA, 2020) can be assumed.</i>	T	L2	PP-473
The mission shall produce air-sea interaction products with a longitudinal mean revisit better than 5 days, over the current system RoI as defined by PP-470.	N	L2	PP-212
The mission shall produce globally sampled air-sea interaction products with a local maximum revisit time of 12 days or better.	N	L2	PP-215
Air-sea interaction products shall be available throughout phase OP-II of the mission.	N	L2	PP-225
Coverage and revisit requirements for cyclones	N		PP-102
The mission shall opportunistically observe cyclones whenever they occur and can be observed by Sentinel-1.	N		PP-103

In order to connect requirements placed on CMV and SST to the TIR instrument, the mission requirements are flown down to specify the requirements for Top-of-Atmosphere Radiance at Level-1 for the TIR instrument. The resulting requirements are shown in Table 4.6.

Table 4.6: Mission requirements at Level-1 specified for the TIR instrument

Requirement	Priority	Level	ID										
Requirements for TAR Product	N	L1	PP-232										
The instrument shall measure the scene radiance in the TIR spectral ranges specified in the table below:	N	L1	PP-245										
<table border="1" data-bbox="172 1592 555 1834"> <thead> <tr> <th>Band</th> <th>Spectral Range [µm]</th> </tr> </thead> <tbody> <tr> <td>TIR-1</td> <td>10.4 - 11.3</td> </tr> <tr> <td>TIR-2</td> <td>11.4 - 12.5</td> </tr> <tr> <td>CD-1</td> <td>8.0 - 9.2</td> </tr> <tr> <td>PAN</td> <td>8.0 - 12.0</td> </tr> </tbody> </table>	Band	Spectral Range [µm]	TIR-1	10.4 - 11.3	TIR-2	11.4 - 12.5	CD-1	8.0 - 9.2	PAN	8.0 - 12.0			
Band	Spectral Range [µm]												
TIR-1	10.4 - 11.3												
TIR-2	11.4 - 12.5												
CD-1	8.0 - 9.2												
PAN	8.0 - 12.0												
<i>Note 1: TIR-1 & TIR-2 are used for SST retrieval; CD-1 for cloud discrimination; PAN for CMV and SST gradient retrieval</i>													

The spatial resolution requirements apply to a swath width that covers the Sentinel-1 wave mode vignettes. <i>Note 1: This shall take into account the relative movements of the vignettes across the different views in PP-445.</i>	N	L1	PP-478
In the across-track views (A3 and B3 in PP-445), the PAN band shall have a spatial resolution no larger than 333m across the swath specified in PP-478.	N	L1	PP-288
In the across-track views (A3 and B3 in PP-445), the TIR-1, TIR-2 and CD-1 bands shall have a spatial resolution no larger than 1000m across the swath specified in PP-478.	N	L1	PP-475
In the skewed views (A1, A2, A4, A5, B1, B2, B4 and B5 in PP-445) the spatial resolution shall be no worse than 2x the spatial resolution of the across-track views.	N	L1	PP-476
The TAR products shall have a NEdT no larger than 0.1K.	G	L1	PP-282
The TAR products shall have a NEdT no larger than 0.15K.	T	L1	PP-479
The TAR products shall have a dynamic range of 200K - 305K. <i>Note 1: This specified range allows the retrieval of the Sea Surface Temperature (SST) gradients and Cloud Motion Vectors (CMV).</i>	N	L1	PP-285
The NEdT requirement specified in the table above shall be met at 280K.	T	L1	PP-287
The NEdT requirement specified in the table above shall be met over the full dynamic range specified in PP-285.	G	L1	PP-286
The swath of the TIR instrument shall be maximised with a goal of 340km in the across-track direction.	G	L1	PP-272
The swath of the TIR instrument shall cover at least that of the SAR Wave mode.	N	L1	PP-273
The TAR product from the TIR instrument shall be spatially co-registered with the SLC product from the SAR instrument with an accuracy of 200m or better.	N	L1	PP-274
The TAR products shall be produced in 5 views, that are symmetrically positioned with respect to the across-track direction, as schematically illustrated below: <ul style="list-style-type: none"> - 3 co-temporal views between the followers (shown with dashed lines) - 5 congruent views with identical viewing geometry and pure time-lapse in between (shown with colours) - 1 view that is simultaneous and colocated with the SAR footprint - 1 across-track view from each follower <i>Note 1: Different views on each Harmony satellite are needed to unambiguously resolve both structure as well as 3D motion of clouds.</i> <i>Note 2: The largest time lapse from the separate views determines the maximum sensitivity for advective processes.</i> <i>Note 3: Line of Sight (LoS) diversity allows enlarging the visible ocean surface in cloudy conditions.</i>	N	L1	PP-283



			N	PP-445
Each view specified in PP-283 shall include the PAN band specified in PP-245.	N	L1	PP-284	
Views A1, A3, B1 and B3 shall include all bands specified in PP-245.	T	L1	PP-444	
All views specified in PP-283 shall include all bands specified in PP-245.	G	L1	PP-446	

4.4 Cryosphere

From the product flow for land ice applications in Figure 4.1, the mission shall be able to generate the products as described in Table 4.7.

Table 4.7: Level-3 products definition for cryosphere/land ice.

Short name	Long name	Description
TOC	Topography Change	Changes in topographic height over timescales between observations. TOC products are derived from single pass interferometry SPI products.
TDV	3D Velocity Vectors	Three-Dimensional displacement/velocity Vectors. Velocity vectors are associated with relatively slow processes that are temporarily resolved by the observation system. TDV products are derived from either repeat-pass interferometry or from combining topographic change products with feature tracking techniques based on SLC products.

In order to generate these higher-level products, Table 4.8 provides the required products at Level-1.

Using the definitions listed in Table 4.7 and 4.8, Table 4.9 provides the mission requirement specification expressed at Level-3 for land ice applications. For the Phase 0, the mission design for the land themes of Harmony was optimised using the TOC and TDV requirements – that was considered more relevant as it could be linked directly to the geophysical parameters of interest for which performance estimation tools were available. As expressed in Table 6.2, the mission shall enable to produce these products, but these products shall not be generated by the Harmony PDGS. Coverage and revisit requirements are listed in Table 4.10.

Table 4.8: Level-1 products definition for cryosphere/land ice.

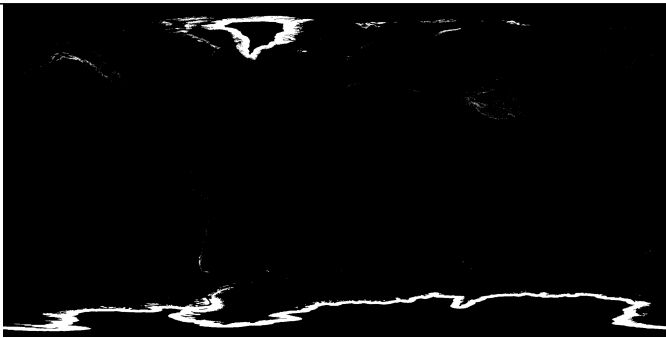
Short name	Long name	Description
SLC	Single Look Complex	See definition in Table 4.2
SPI	Single Pass Interferogram	SPI (from SPInSAR) products are multi-looked and interferometrically calibrated single-pass interferograms, coherences, and intensity images, calculated from the SLC products of the two followers. They contain two orthogonal polarisations. They require the observation system to form an across-track interferometric baseline (XTI) during a single overflight.

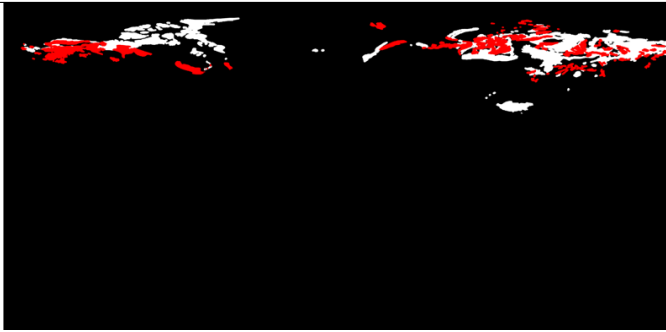
Table 4.9: Requirement specification for cryosphere applications.

Requirement	Priority	Level	ID
TDV requirements for land ice	N		PP-28
The mission shall support the estimation of TDV with a horizontal resolution of 100 x 100 m ² (threshold) or 30 x 30 m ² (goal). <i>Note 1: The threshold requirement is matching the specification in (Glaciers-CCI, 2019) with the understanding that current techniques measure at most two components of the displacement vector</i> <i>Note 2: TDV requirements for land ice are driven by OBJ-C21 and relate to OBJ-C22.</i>	N	L3	PP-14
The mission shall support the estimation of TDV with an accuracy of the velocity magnitude of 5% (threshold) or 3% (goal). <i>Note 1: For surface velocity of glaciers and ice streams specifications are provided in relative scale (%) due to the wide range of velocities (up to several km/yr). A threshold value for slow velocities may be added (e.g. 5 m/yr or 10 m/yr).</i>	N	L3	PP-15
The mission shall support the estimation of TDV with a temporal sampling of 1 yr (threshold) or 1 month (goal).	N	L3	PP-17
TOC requirements for land ice	N		PP-30
The mission shall support the estimation of topography change at a horizontal resolution of 100 x 100 m ² (threshold) or 50 x 50 m ² (goal). <i>Note 1: The threshold requirement is matching the specification in (Glaciers-CCI, 2019) with the understanding that current techniques measure at most two components of the displacement vector</i> <i>Note 2: TOC requirements for land ice are driven by OBJ-C11 & OBJ-C21.</i>	N	L3	PP-33
The mission shall support the estimation of topography change with an accuracy of 0.5 m/yr (threshold) or 0.2 m/yr (goal). <i>Note 1: Accuracy requirements specified in terms of topography change rates as it refers to relative height differences over a certain time span.</i>	N	L3	PP-34

The mission shall support the estimation of inter-annual relative surface height change rates at least once during the mission. As a minimum, Harmony should provide monthly measurements in two different years. In order to maximize the sensitivity to inter-annual changes these measurements should take place near the beginning and near the end of the mission.	N	L3	PP-36
TOC requirements in permafrost regions	G		PP-178
The mission shall support the estimation of topography change at a horizontal resolution of 100 x 100 m ² (threshold) or 30 x 30 m ² (goal). <i>Note 1: TOC requirements for permafrost relate to OBJ-C41.</i>	G	L3	PP-182
The mission shall support the estimation of topography change with an accuracy of 0.5 m/yr (threshold) or 0.2 m/yr (goal).	G	L3	PP-183
The mission shall support the estimation of topography change with a temporal sampling of 3 yrs (threshold) or 1 yr (goal).	G	L3	PP-184

Table 4.10: Coverage and revisit requirements for cryosphere

Requirement	Priority	Level	ID
Coverage requirements for land ice	N		PP-429
The mission shall observe TOC and TDV for glaciers, ice streams and grounding zones with a coverage defined as the Land ice RoI mask in PP-431.	G	L3	PP-13
	N		PP-431
The mission shall observe TOC and TDV for glaciers, ice streams and grounding zones with a coverage defined as the intersection of the mask in PP-431 with the Sentinel-1 reference scenario defined in (ESA, 2020).	T	L3	PP-461
Coverage requirements for permafrost	G		PP-430
The mission shall support the estimation of topography change for permafrost regions with a coverage as indicated by the Permafrost RoI mask in PP-432.	G	L3	PP-181

		G	PP-432
---	--	---	--------

4.5 Solid Earth

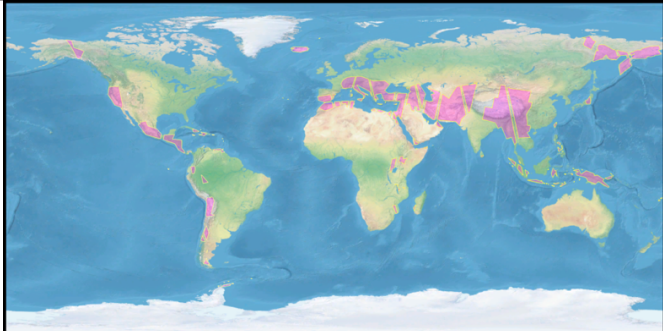
For Level-3 product definitions for TOC and TDV, please refer to Table 4.7; for Level-1 product definitions for SLC and SPI, please refer to Table 4.8. Following those definitions, Table 4.11 provides the mission requirement specification at Level-3 for solid Earth applications. Coverage and revisit requirements are listed in Table 4.12.

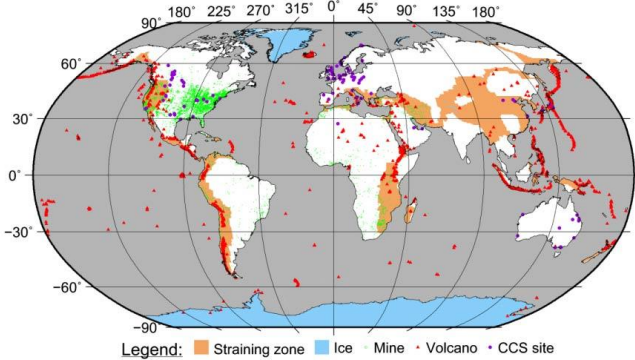
Table 4.11: Requirement specification for Solid Earth applications.

Requirement	Priority	Level	ID
TDV requirements for strain rates	N		PP-189
The mission shall support the estimation of 3D surface velocity vectors with the specified accuracy over the duration of the mission.	N	L3	PP-20
The mission shall support the estimation of 3D surface velocity vectors at a horizontal resolution of 100 x 100 m ² . <i>Note 1: This is required to meet the objective of constraining strain rate with sufficient resolution to detect spatial variability as small as 10 nanostrain per year.</i>	N	L3	PP-22
The mission shall support the estimation of 3D surface velocity vectors with a relative performance error of 1 mm/yr in each dimension (Up-Down, East-West, North-South). The relative performance error is to be evaluated over distances of 100 km. <i>Note 1: This is required to meet the objective of measuring strain rates down to 10 nanostrain per year at the largest relevant length scale.</i> <i>Note 2: This requirement is driven by OBJ-G11.</i>	G	L3	PP-24
The mission shall support the estimation of 3D surface velocity vectors with a relative performance error of 2 mm/yr in each dimension (Up-Down, East-West, North-South). The relative performance error is to be evaluated over distances of 100 km.	T		PP-458
TOC requirements for volcanoes	G		PP-199
The mission shall support the estimation of surface height changes with an observation at least once every 12 days.	G	L3	PP-39

The mission shall support the estimation of surface height changes at a horizontal resolution of 30 x 30 m ² . <i>Note 1: Resolution and accuracy (PP-41) can be traded against each other.</i> <i>Note 2: TOC requirements for volcanoes are driven by OBJ-G12.</i>	G	L3	PP-40
The mission shall support the estimation of surface height changes with an accuracy of 1 m.	G	L3	PP-41
The mission shall support the estimation of surface height changes for two consecutive years (goal) and for two non-consecutive years (threshold).	G	L3	PP-42

Table 4.12: Coverage and revisit requirements for solid Earth

Requirement	Priority	Level	ID
Coverage requirements for strain rates	N		PP-433
The mission shall observe 3D surface velocity vectors for tectonic straining regions with a coverage as indicated by the Global Strain RoI mask in PP-435.	G	L3	PP-434
	G	L3	PP-435
The mission shall observe 3D surface velocity vectors for tectonic straining regions with a coverage as indicated by the mask in PP-471, which is the intersection of the Global Strain RoI mask with the areas covered by S1 in both ascending and descending passes, according to the Sentinel-1 reference scenario defined in (ESA, 2020).	T	L3	PP-465
	T	L3	PP-471
Coverage requirements for volcanoes	N		PP-436

<p>The mission shall support the estimation of surface height changes over volcanoes. The locations of the volcanoes are indicated as red triangles in the below figure.</p>	G	L3	PP-38
 <p>Legend: Straining zone Ice Mine Volcano CCS site</p>	G	L3	PP-437

5 PRELIMINARY SYSTEM CONCEPT(S)

This Section provides the technical description of the Harmony mission, as derived from the preparatory activities in Phase 0. Two technical baseline concepts (referred to as A and B) are described that were developed in two parallel Phase 0 system studies led by ADS and TAS respectively. Several of the figures in this chapter are courtesy of the respective industrial consortia.

5.1 Description of Mission Architecture

5.1.1 Objectives and Driving Requirements

Harmony is a mission that will observe in four dimensions: it will observe 3D velocity vectors and how they change over time. While this capability serves many different scientific applications, the spatial and temporal scales of interest vary greatly. Capturing all the relevant requirements and combining them in a single mission concept has been the greatest challenge and necessitated a rigorous traceability from science objectives down to Level-1 requirements. The requirements on each of the products have been described in Chapter 4 and the traceability between the requirements at different levels is schematically shown in Figure 4.1 on page 35. Six products are defined at L1: SPI, COV, ICS, SLC, USV, and TAR. There are no driving performance requirements on the COV and ICS products. During Phase 0, both consortia have optimised the system directly against the performance requirements on TDV and TOC products. Hence the flow-down of these performance requirements to SLC and SPI products respectively is irrelevant. All the SAR products are derived from one common low-level product: the SLC, for which L1 performance requirements have been specified. In summary, the requirements that have been driving the system design are those associated with these five products: TDV, TOC, USV, SLC and TAR. These are discussed in more detail hereafter.

3D Velocity Vectors (TDV): These are observed with Repeat Pass Interferometry (RPI) to measure velocity components along multiple LoSs. The specified accuracy (PP-15,PP-24) typically requires a stack of images gathered from multiple ascending and descending passes, and a favourable viewing geometry. Hence the performance requirements, together with the sampling (PP-17,PP-20,PP-26) drive the observations plan and the distance between Harmony and Sentinel-1 (S1). A good Signal to Noise Ratio (SNR) is also important, which flows down to the Single Look Complex SAR image (SLC) requirements and drives the design of the SAR antenna.

Topography Changes (TOC): These are observed with single-pass XTI and contain vertical topography changes. The performance requirements (PP-33,PP-34,PP-36) drive the SNR to be delivered by the instrument and - through the perpendicular baseline required between the two followers - the design of the XTI formation.

Geophysically equivalent surface velocities (USV): These are instantaneous velocity vectors associated with scatterers at the ocean surface, observed with Along-Track Interferometry (ATI) or Doppler Centroid Anomaly (DCA). At this early stage, the sensitivity requirements on USV are flown down directly from the SCV requirements PP-221 and PP-222. They are some of the most driving requirements for the system design, as they drive the distance with S1 in stereo formation, the ATI baseline length (and hence the SAR antenna design), and the SNR that must be achieved (also driving SAR antenna design).

Single Look Complex SAR image (SLC): The classic root product of phase-preserving imagery from a SAR instrument from which all other products are derived. Spatial resolution will be similar to that of S1 (after ground projection). Typical Level-1 requirements on NESZ, DTAR, and RA are flown down from the intermediate Covariance matrices of normalized radar scattering coefficients (COV) requirements (to enable wind retrievals), and from the higher level TDV and TOC requirements:

- Noise Equivalent Sigma Zero (NESZ): -21 dB
- Distributed Total Ambiguity Ratio (DTAR): -19 dB
- Radiometric Accuracy (RA): 0.6 dB

The NESZ and DTAR requirements are at first instance the most driving since they determine the design of the antenna (as explained in Section 5.3.1). The RA requirement will drive the calibration approach. Flow-down of USV requirements to SLC is not relevant since USV performance is evaluated directly and the flow-down requires detailed assumptions on the antenna implementation. The performances required for SLC on one hand and USV on the other, drive the design of the SAR antenna in different directions. Both concepts include an innovative multi-channel antenna design that allows to meet the requirements for all products with the same antenna concept. This is explained in more detail in Section 5.3.1.

Top of Atmosphere Radiances (TAR): Brightness temperatures from the TIR instrument are used for the retrieval of the Sea Surface Temperature (SST) gradients and Cloud Motion Vectors (CMV). The performance requirements are listed in Table 4.6. The specified Noise Equivalent delta Temperature (NEdT) (PP-479), the spatial resolution (PP-288, PP-475), and the multi-view observation geometries (PP-283), drive the design for the optical instrument. The instrument will observe in the 4 spectral bands listed in table 4.6 with their main purpose (PP-245). Observations shall be co-located with the swath of the SAR instrument, as a minimum covering the range spanned by the SAR WV vignettes (PP-273). The different views on each Harmony satellite are there to unambiguously resolve both structure as well as 3D motion of the clouds. The number of views and their geometry will be consolidated further once the end-to-end performance simulation tools have matured enough to make quantifiable trade-offs. For Phase 0, the five views shown in Fig. 5.1 have been specified (PP-283) in order to constrain the degrees of freedom. Nearly 6 minutes separate the most forward view (A5) with the most rearward view (B5), resulting in maximum sensitivity to small target velocities.

5.1.2 Mission Architecture

The space segment consists of two companion satellites to S1, each carrying a receive-only SAR instrument, complemented by a TIR payload. The companion satellites fly in two different configurations with S1. In the stereo configuration, one companion is leading and the other is trailing S1. The optimum distance to S1 (stereo baseline) is determined from a complex trade-off on the performance of both instruments. One of the strongest drivers is the improved viewing geometry associated with large squint angles and both concepts therefore use a long baseline (350 km for Concept A and 400 km for Concept B). The Harmony orbit is dictated by the S1 orbit, which is a Sun-synchronous, frozen orbit with a repetition cycle of 12 days, during which 175 orbits are completed.

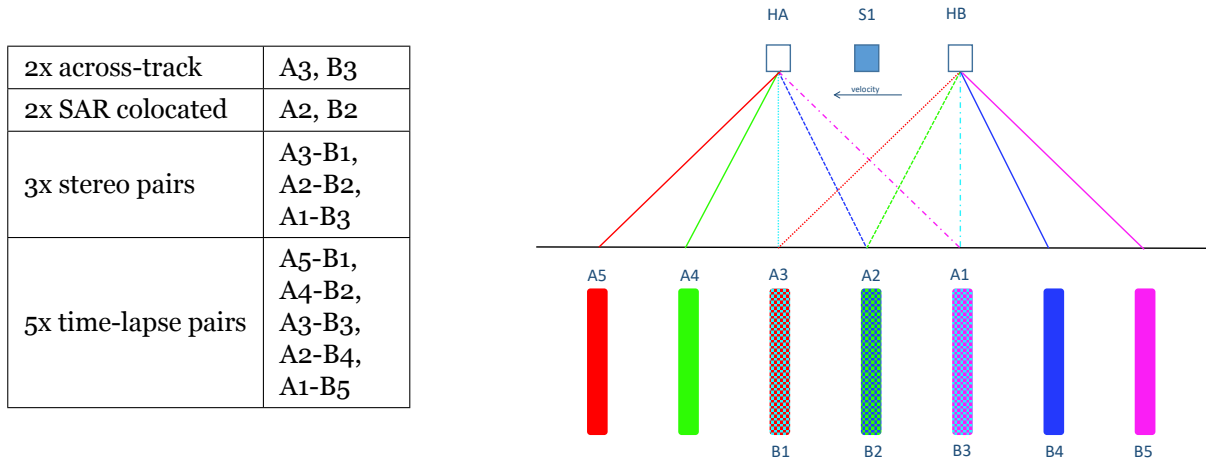


Figure 5.1: The 5 views of both Harmony spacecraft A and B are shown with respect to the antenna footprint of Sentinel-1. Stereo pairs provide geometric information. Time-lapse pairs provide velocity information.

The overall mission architecture is shown in Figure 5.2. It includes the following elements:

- The Launch Segment: Harmony is designed to be compatible with a launch on Vega-C.
- The Space Segment: this is comprised of two Harmony satellites flying in formation with S1.
- The Ground Segment, including a Flight Operation Segment (FOS) and a Payload Data Ground Segment (PDGS), each interfacing that of S1 (as described in Section 5.5).

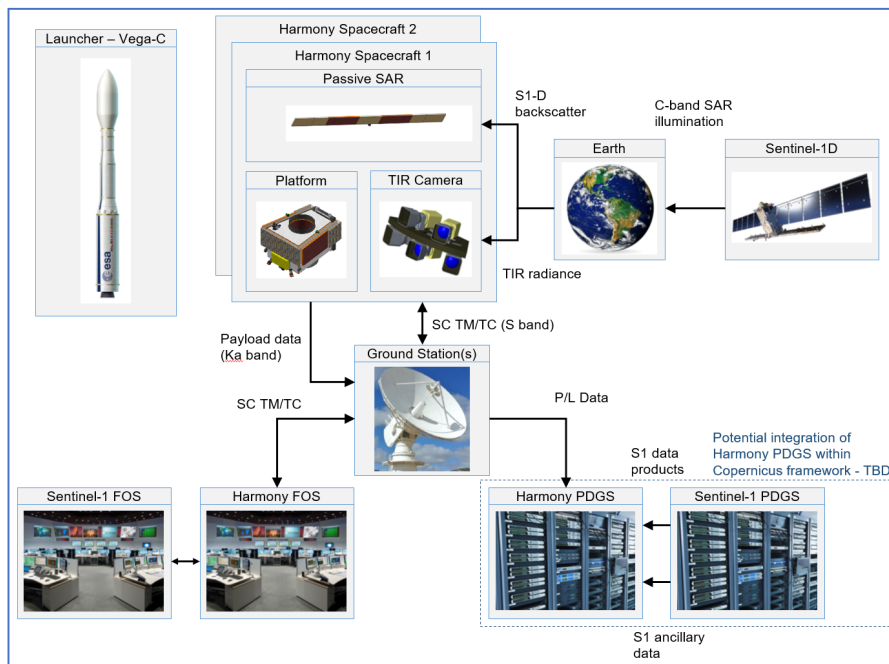


Figure 5.2: Harmony mission architecture (Concept A).

The stereo and XTI configurations of the Harmony formation are illustrated in Figure 5.3. With its forward, backward and sideways viewing geometry, the stereo configuration is optimised for detecting velocity vectors on the surface. Different observation techniques (Doppler detection, RPI, backscatter) are deployed to detect velocities from the very slow (mm/year) for solid Earth applications, to the very fast (m/s) for ocean currents and wind. The XTI configuration is optimised to detect vertical movements of the surface. Thanks to the Single Pass Interferometry (SPI) observation technique, both sudden and slow changes in topography in the order of 10's of cm can be detected and quantified.

A multi-spectral TIR imager complements the SAR instrument. The imager has 5 views, as illustrated in Figure 5.1. The multi-channel, multi-view capabilities of the instrument return information about structures in the sea temperature and the clouds above.

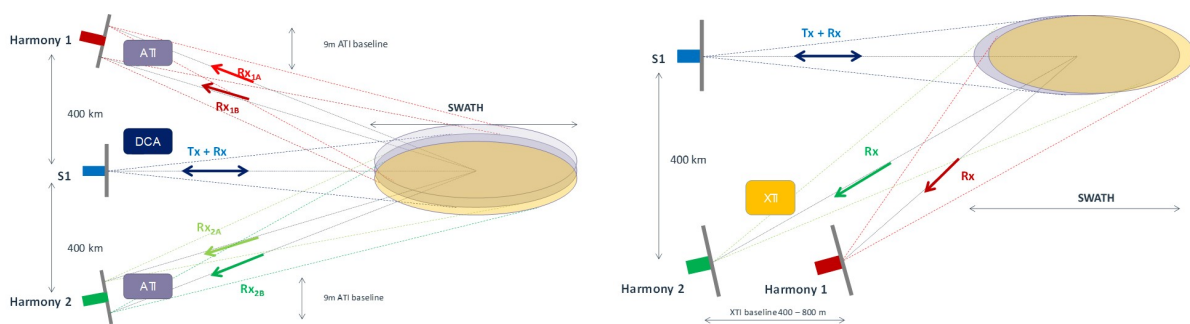


Figure 5.3: (left) stereo and (right) XTI flight configuration. (Concept B)

5.2 Mission Analysis

5.2.1 Assumptions on Sentinel-1

Harmony is designed to be compatible with either Sentinel-1C (S1-C) or Sentinel-1D (S1-D) as a transmitter (see also Section 5.3.1.3). With a planned launch date in the 2024-2027 timeframe (Copernicus Space Component Long Term Scenario) and an expected lifetime of 10 years, S1-D can be assumed to be in orbit at the time the Harmony mission will fly. The current operational scenario of Sentinel-1A (S1-A) and Sentinel-1B (S1-B) applies a complex load balancing at constellation level, with the two satellites having very different observation plans. The operational scenario that will be applicable to S1 is not yet defined and may look very different from that of today. To support the Harmony mission analysis, a realistic reference scenario has been assumed and is documented in (ESA, 2020). This reference scenario is based on the current S1-A observations plan (Figure 5.4). Of course this is only a reference scenario, since any major modification to the real S1 operations plan will follow the High Level Operations Plan revision process, which includes an endorsement by the European Commission. The reference scenario makes an allowance for a small increase in observation capacity up to the current limit of 30 minutes per orbit. Flexibility in the load balancing between the S1 satellites is introduced by allowing duty cycles up to a maximum of 35 minutes, for up to 35 orbits per cycle, while keeping the mean duty cycle below 30 minutes. In the next Sections it is explained how the Harmony science objectives can be met with the reference scenario currently assumed. Improvements to the coverage will be studied in the next phase.

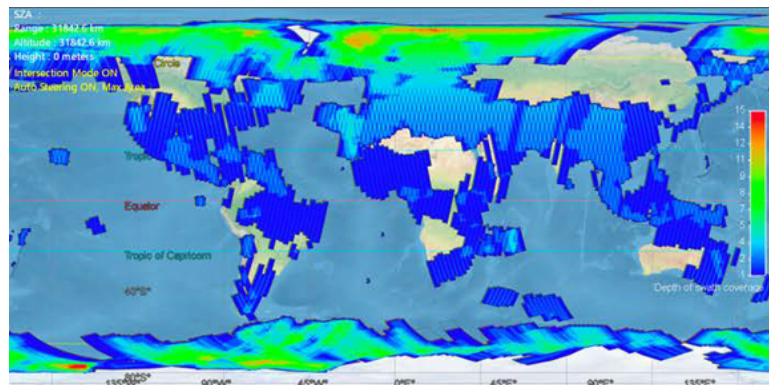


Figure 5.4: Depth of coverage obtained for one cycle of S1-A observations during the non-eclipse season in Jan/Feb 2020. This cycle is used as a reference scenario for Harmony. Dark blue means a single pass, cyan around 4 passes, and green around 8 passes.

5.2.2 Coverage and Revisit

Since Harmony is serving many different science goals, the Mission and Technical Requirements Document (MATER) has coverage and revisit requirements for each. RoI are defined for land ice (PP-431, PP-461), permafrost (PP-432), strain rates (PP-435, PP-471) and air-sea interactions (PP-467, PP-472, PP-468, and PP-480). Of these, only land ice, strain rates and air-sea interactions are included as primary mission objectives. RoI masks have been defined for both threshold and goal requirements, the latter covering all areas of potential scientific interest. Threshold requirements are defined as the intersections of the RoI with currently observed areas by S1. For air-sea interactions the situation is a little different since at present S1 is observing in imaging mode (IW or EW) primarily in coastal areas, and in wave mode over the deep oceans. Harmony will take benefit of both these coastal imaging and global sampling capabilities. In addition, the mission requirements include RoI over major current systems, which are to be systematically imaged in IW/EW mode with a high revisit of 5 days or less (PP-212). The imaging of these ocean RoI is possible with a small extension to the current S1 duty cycle, and within the constraints documented in (ESA, 2020). Figure 5.5 shows a combined mask with the RoI for land ice, strain rates and air-sea interactions. It represents the sizing scenario for duty cycle and data volume. The Figure also shows the coverage and revisit times that Harmony can achieve, assuming EW mode imaging over the ocean RoI. In practise IW will offer better spatial resolutions and will be the mode of choice in the most energetic regions with smaller features, i.e. at higher latitudes. EW mode will be the mode of choice to observe the larger features in equatorial regions with a revisit time of 5 days. Finally it can be noted that no explicit revisit requirements have been formulated corresponding with land ice or strain rate objectives, since the revisit time is already implied by the performance requirements on TDV and TOC products.

5.2.3 Orbit and formation flying

A key feature of the mission is that the formation can be reconfigured into the stereo and XTI configuration, as explained in Section 5.1. The stereo configuration optimises the performance of the USV and TDV products, whereas the XTI configuration optimises the performance of the TOC product.

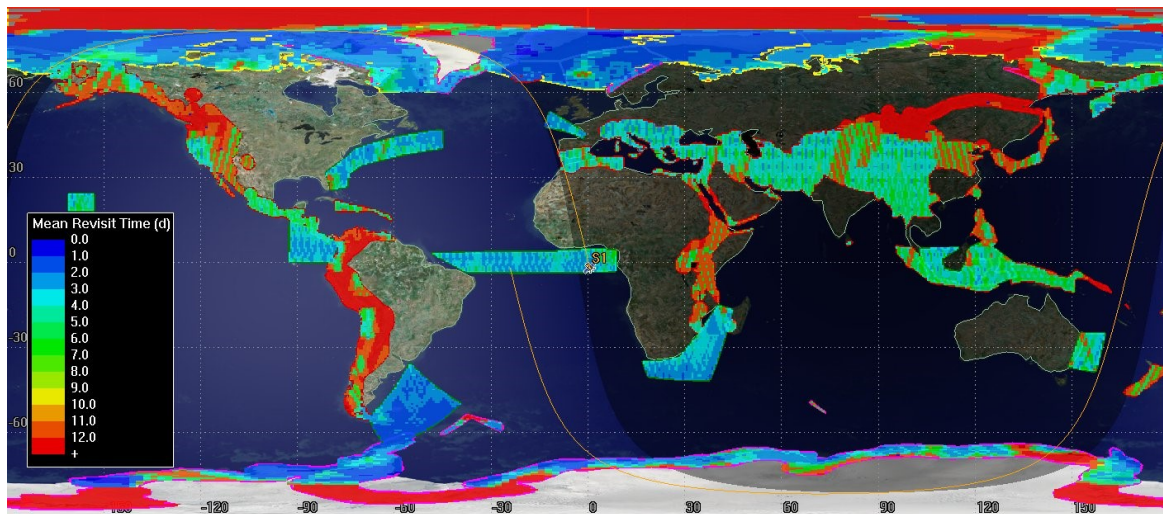


Figure 5.5: Coverage and mean revisit time that Harmony will achieve over a combined (goal) observation mask for Ocean Arctic + Ocean major current system + Cryosphere land ice + Solid Earth strain rates. Although most of the RoI are well covered on both ascending and descending passes, it can be seen that some areas remain red (Siberia, South America), which means that these areas are typically observed by S1-B rather than S1-A. For the current analysis it has been assumed that over land the S1 duty cycle is not extended. A small extension has been assumed to cover the ocean RoI in imaging mode (IW/EW). (Concept B)

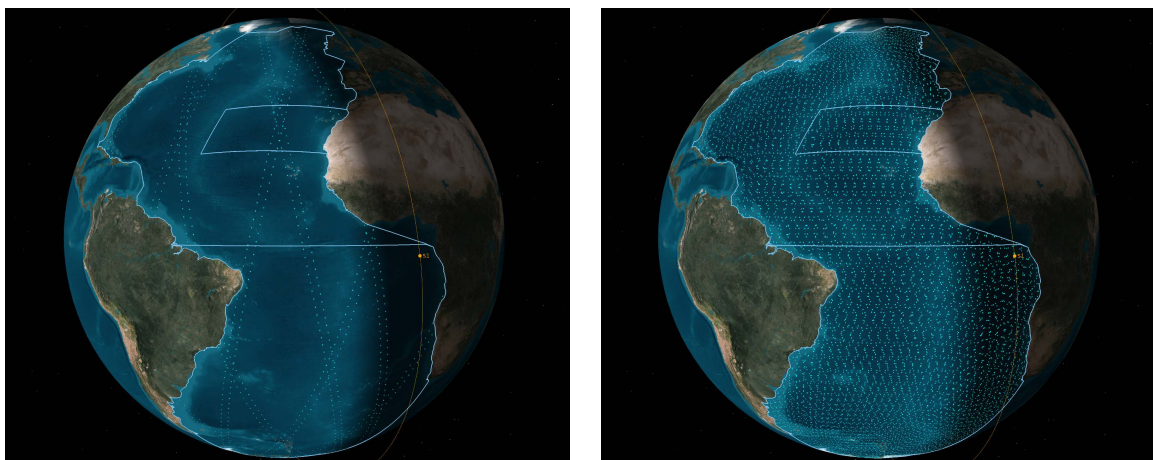


Figure 5.6: Whenever S1 and Harmony are not in imaging mode (IW/EW) over the ocean, they will be sampling the ocean in wave mode (WV) as shown here after 1 day (left) and after 1 cycle of 12 days (right). The WV products are discontinuous, but provide global sampling and better SLC and USV performance. (Concept B)

5.2.3.1 Stereo phase

During the stereo phase, the nominal orbit is that of S1, with both Harmony satellites flying ahead and behind S1. Harmony can coordinate its manoeuvres to be performed at the same time. Depending on solar activity, 25 to 220 in-plane manoeuvres per year may be required, corresponding with a delta-V of between 0.18 m/s and 15 m/s. In addition but much less

frequently, out-of-plane manoeuvres up to typically 25 cm/s are required, assuming the orbital tube is controlled to ± 120 m, just like S1. Safety of the formation is ensured by the long distances with S1. Should one of the satellites enter safe mode, the response time before a collision can occur is in the order of 7 days.

5.2.3.2 XTI phase

During the XTI phase, the two Harmony satellites will fly in a passively safe helix formation. In this phase the interferometric sensitivity to topography is driven by the so-called perpendicular baseline, which is the distance between the two followers, as measured in a vertical plane and orthogonal to the LoS. The perpendicular baseline varies over the orbit, as shown in Figure 5.7. Combining ascending and descending passes, the whole range of latitudes is covered with baselines ranging between 500 m and 800 m. Latitudes below about 20° are observed with baselines exceeding 400 m in both ascending and descending passes. Around the poles the baseline is limited to around 500 m, which is compensated by more frequent revisits.

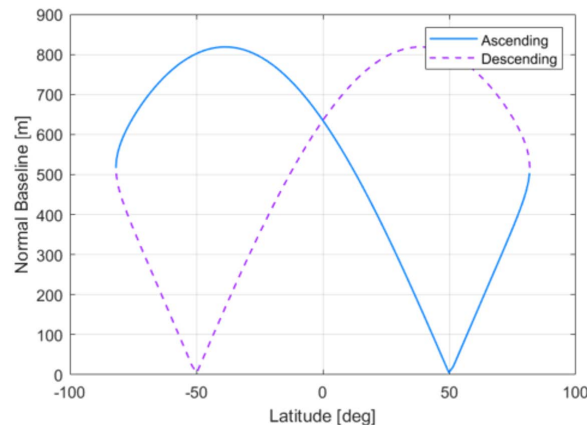


Figure 5.7: The perpendicular baseline length achieved during XTI phase is shown as a function of latitude. Ascending and descending geometry can be switched in order to achieve good performance over all latitudes. (Concept B)

5.2.3.3 Transfer phase

Transfer phases are required for Harmony to pass from the stereo phase to the XTI phase or vice versa. One of the Harmony satellites is brought in an orbit with an in-plane drift and taken out once it reaches the target position. A trade-off exists between transfer duration and propellant consumption. A nominal value is obtained by performing the transfer in one week, which would require a delta-V of around 2.2 m/s. The question arises whether both Harmony satellites are designed to be interchangeable and/or equal. Both concepts A and B have chosen for identical designs for programmatic reasons. A change in attitude of the spacecraft ensures this is possible for the radar instrument. This implies, however, that the optical instruments on each of the Harmony satellites are compatible only with either the leading or the trailing position. During XTI phase it is not required to have two operational optical instruments. Both Concept A and B have opted for a solution whereby both Harmony satellites will be interchangeable and share the burden of making the transfers. Since leading and trailing positions for the stereo phase are fixed, the satellites need to take turns to make

the round-trip in-and-out of XTI phase.

5.3 Space Segment

5.3.1 SAR Instrument

The SAR instrument on the Harmony satellites will passively receive the echoes of the pulses transmitted by S1. It needs to be compatible with all the different radar modes used by S1, including the Terrain Observation by Progressive Scans (TOPS) modes. This requires the antenna to have elevation and azimuth steering capabilities. For the measurement of the surface velocities (USV) with ATI, the antenna needs to be split into at least two phase centres, which are recorded simultaneously. The measurement accuracy improves with an increased separation of the antenna phase centres. Similarly, the Doppler Centroid Anomaly (DCA) measurement accuracy improves with antenna length, which leads to a narrower beam width. Both measurement techniques benefit from improvement in SNR, which is proportional to the antenna surface. Increasing the baseline as well as the antenna surface are conflicting design drivers, both limited by mass, volume and budget constraints. Due to the bistatic observation geometry, the echo of the vertically polarised pulse transmitted by S1 is not anymore aligned with the vertical polarisation of the Harmony antenna. In order to receive the full signal energy Harmony coherently records both polarisations, allowing any required receive polarisation to be reconstructed in ground processing. The SAR instrument is split in two major sub-systems, the SAS and the SES, which are described in more detail in the following.

5.3.1.1 SAR Antenna Subsystem (SAS)

The SAR antenna subsystem (SAS) is the most visible part of the radar instrument with its large antenna aperture. It includes the radar front-end with the radiating elements, the first level of distributed low noise amplification and the beam forming network. It provides the following functions:

- Splitting the receive antenna aperture in a number of sub-apertures (also referred to as phase centres), which are distributed along azimuth direction,
- Combining a number of dual polarised radiating elements into sub-arrays,
- Providing low noise signal amplification combined with variable attenuation and phase shift to allow for electronically controlled beam shaping and beam pointing in azimuth and elevation,
- Combining the signals from all sub-arrays in each sub-aperture as inputs to the SES,
- Controlling the attenuation and phase setting of the Rx modules including temperature compensation and monitoring,
- Distributing the internal calibration signal from the SES to the Rx modules,
- Distributing and conditioning of the DC power needed for the front-end electronics.

As explained above, the ATI observations require to split the antenna in at least two sub-apertures with an as long as possible baseline between the ATI phase centres. For the measurement of TDV and the measurement of TOC during the XTI phases, the signals from the full antenna are combined to provide enough sensitivity and ambiguity suppression. The Harmony SAR performance is determined by the combined antenna gain from the S1 transmit

pattern and the array pattern of the combined Harmony receive apertures. With the pulse repetition frequency (PRF) given by S1, the signal contributing to the azimuth ambiguities falls in certain angles of the two-way antenna pattern. As shown in the following example, it turns out that the addition of a third sub-aperture in the centre between the two wings significantly improves the azimuth ambiguity performance. Through a nonlinear optimisation of the end-to-end performance, the number and distance between the phase centres has been determined. For this optimisation, accommodation and instrument mass constraints were also taken into account. This lead both concepts to adopt the antenna configurations shown in Figure 5.9, together with their physical dimensions.

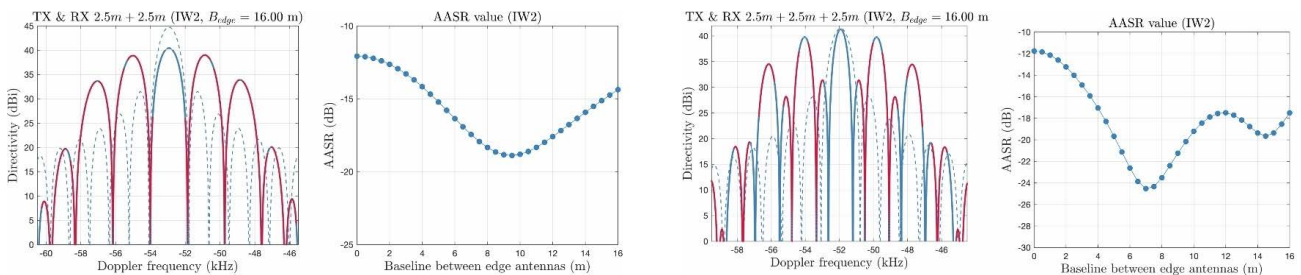


Figure 5.8: The plot on the left shows the directivity of the S1 Tx antenna as dashed line and the directivity of the Harmony Rx antennas as solid line. In this example from Concept A, each Rx sub-aperture has a length of 2.5 m and the distance between the wing phase centres is 16 m. The red colour marks the Doppler frequencies from where ambiguous signal energy is received. For the centre right plot a third sub-aperture has been added in the centre between the wings. The plots on the centre left and on the right side show the evolution of the azimuth ambiguity to signal ratio (AASR) as a function of distance between the wing phase centres for the two and the three sub-aperture case.

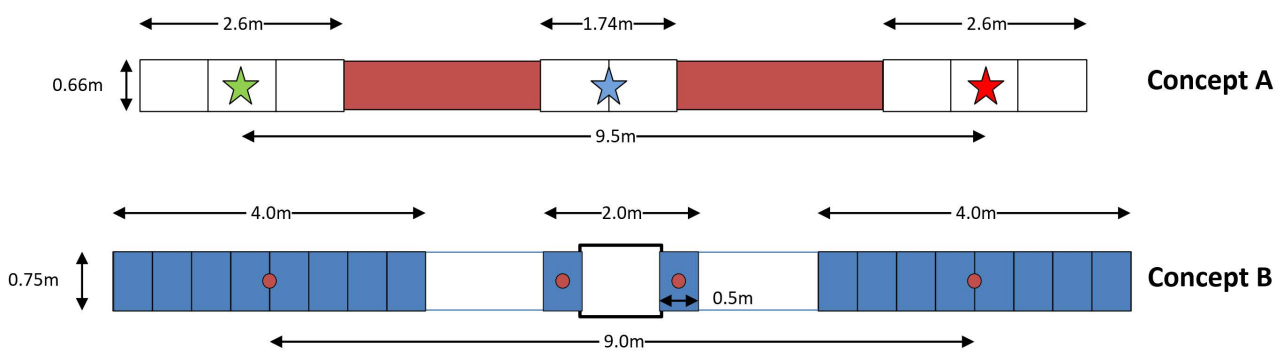


Figure 5.9: SAR antenna configuration showing the two wing and the centre apertures in Concept A and the two wing apertures and the split centre aperture in Concept B. The centre aperture in Concept B is split in order to allow for a stacked launch configuration.

In Concept A, the SAR antenna has an overall length of 12.1 m. The wing apertures have a separation of 9.5 m between their phase centres. They are split in three antenna panels each, while the centre aperture has two antenna panels. Every panel is built-up of 8 sub-arrays in elevation containing 2x10 dual polarised patches each. Every sub-array is equipped with an Rx module providing low noise amplification as well as amplitude and phase control for

both polarisation channels. Four of these Rx module functions are integrated in one Quad receive module, that is 2 Quads per panel and 16 Quads in total. Within every sub-aperture the signals for both polarisations are summed up by the antenna feed network and the 3x2 signals are provided to the inputs of the SES.

In Concept B, the SAR antenna has an overall length of 13 m. The wing apertures have a separation between their phase centres of 9.0 m, which are split in 8 antenna panels each. The centre aperture has two antenna panels with a separation of 1.5 m between the two panel phase centres. Every panel is built-up of 16 sub-arrays in elevation. They are realised by slotted waveguides providing both linear polarisations similar to the radiators used by S1. Each of the 16 waveguide pairs is equipped with a Rx module providing low noise amplification as well as amplitude and phase control for both polarisations. Four of these Rx module functions are integrated in one Quad receive module, that is 4 Quads per panel and 72 Quads in total. For each wing aperture the signals for both polarisations are summed up by the antenna feed network. Similarly, the signals from the two central panels are combined. Also here there are in total 3x2 signals provided to the inputs of the SES.

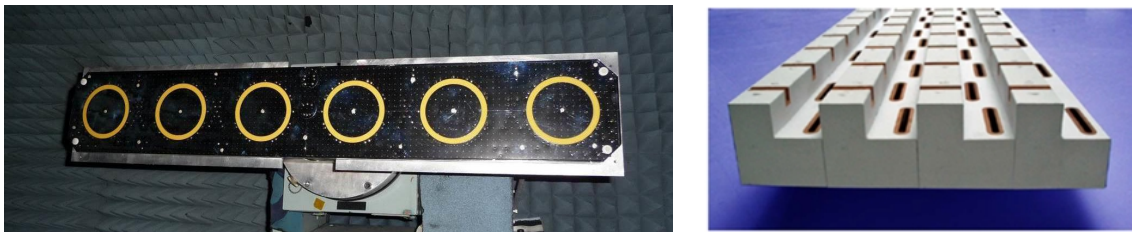


Figure 5.10: (left) Breadboard of an L-band dual linearly polarised circular patch subarray built for SAOCOM-CS and (right) four C-band dual polarised waveguide radiators used on S1.

The proposed radiating element technology is well known. It will be adapted to fit for the application in Harmony. The dual polarised patch technology was already used in the phased array antenna of ASAR flown on Envisat. This radiator technology was used in several applications since then. The dual polarised slotted waveguide technology in metalized CFRP technology is used on S1. A pre-development has been started for Concept B to design a version adapted for Harmony in aluminium. The receive module technology is derived from the TRM technology used in S1. Harmony requires only the receive function, which is a significant simplification.

5.3.1.2 SAR Electronic Subsystem (SES)

The SAR electronic subsystem (SES) is the core of the radar instrument. It contains the following functionalities:

- Generating the radar timing for the SES and the SAS,
- Routing of all radar signals coming from the SAS to the radar receivers,
- Amplifying, analogue filtering and power conditioning of the radar echo,
- Sampling and digital down conversion and decimation filtering of the received signal,
- Compressing and transferring of the payload data to mass memory,

- Generating the internal calibration signal,
- Command and control of the radar instrument.

The SES in Concept A has a Routing and Redundancy Network (RRN) as interface to the SAS. The RRN performs the redundancy switching between the prime and the redundant Central Electronics (CE) and combines (during XTI mode) in the analogue domain the signal from the central sub-aperture with the signals of the wing sub-apertures. This is required because the CE has only four input channels, two per polarisation. The CE samples the signal directly without mixing it to an intermediate frequency, which is a significant simplification of the RF Section of the CE. The SES in Concept B shown in Figure 5.11 can record the signals from all three sub-apertures separately. At the SAS interface, the incoming signal is simply split to the nominal and the redundant branch. With this approach, there is no need for redundancy switches. Any combination of the signals from the different sub-apertures can be performed in the digital domain if required. The SES architecture is quite similar in both concepts but the integration of the functions in Concept B is not as high as in Concept A.

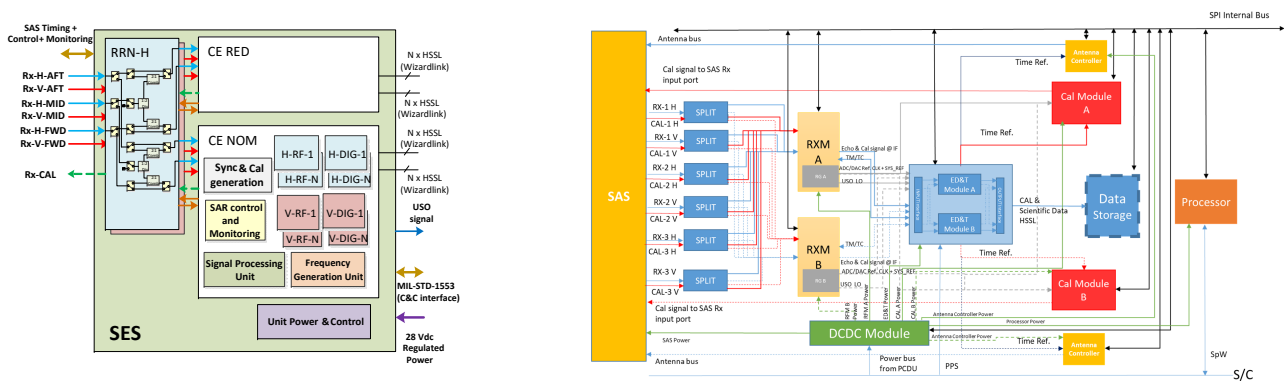


Figure 5.11: (left) Functional block diagram of the SES in Concept A comprising of Routing and Redundancy Network (RRN), Central Electronic (CE) and Power Unit. (right) Functional block diagram of the SES in Concept B comprising of signal splitter, Receiver only Module (RXM), Echo Digitizer & Timing Module (ED&T), Calibration Module, Antenna Controller, Data Storage, Processor and DCDC Module.

5.3.1.3 Synchronisation with Sentinel-1

To enable its bistatic observations, Harmony needs to time-synchronise its receivers with the radar transmitter on S1. This is required at three levels:

1. **Local Oscillator (LO) synchronisation:** The local oscillators on transmit and receive side must be synchronised to an accuracy of better than 5° in order not to cause frequency and phase errors in the USV, TDV and SPI products.
2. **Coarse-time synchronisation:** In order to synchronise the antenna beamsteering, it is necessary to synchronise the start of the data take between S1 and the Harmony satellites with an accuracy of around 3 ms. The task is challenging because S1 uses a position-based commanding approach to trigger the data take start.
3. **Fine-time synchronisation:** Radar receivers are not in listening mode 100% of the time. They use receiving windows when they expect the echoes to return in order to

reduce the amount of data they need to record. This requires a synchronisation with an accuracy of around 20 μ s.

It can be noted that while it is more difficult to obtain fine-time synchronisation than coarse-time synchronisation, the latter is more critical as it must be achieved for the radar system to function, and it must be achieved in real-time. Fine-time synchronisation is only required to reduce the data volume, and can be performed off-line provided sufficient data storage is available.

LO synchronisation is achieved by using Ultra Stable Oscillator (USO) clocks on all spacecraft and employing the so-called common-clock approach, whereby the instrument clocks are also used as local clock by the on-board Global Navigation Satellite System (GNSS) receivers. The GNSS system automatically retrieves any drift between the local clocks and the atomic clock reference of the GNSS system. Implementation of the common-clock approach on S1 required a small modification to its design, which will be implemented on the C and D models. Both concepts have adopted this approach and have shown that the residual errors are sufficiently small, for both the interferometric measurements and the LoS velocity measurements. A detailed end-to-end simulation was performed as part of a risk retirement activity for Concept A, and confirmed there are no show-stoppers for Harmony using this synchronisation method.

In order to achieve coarse-time synchronisation, a wide range of solutions have been studied. They all revolve around the Harmony satellites making an assisted prediction about the S1 position, based on some extra information used by the Harmony satellites. Both concepts A and B have settled for a method whereby the predicted orbit from S1 is used to convert the position where S1 will start its acquisition to an acquisition start time. This information must be uploaded to the Harmony satellites prior to the acquisition. With S1 already in orbit, it has been possible to test the accuracy of this method as a risk retirement activity (Concept A). The results are shown in Figure 5.12 and have demonstrated the feasibility of the method.

Also for fine-time synchronisation different solutions have been investigated. All methods investigated use the signals transmitted by S1, but differ in which signals are being used (direct, specular reflection or the echo) and how they are received and processed. Initial simulations performed as part of risk retirement activities with both concepts have shown that the required accuracy is achievable, but probably not under all circumstances. Backup options are in place for when the signals are too weak to retrieve the fine-time synchronisation. These are the temporal storage of 100% of the data until the real times are known and can be uploaded from ground (Concept A) or to download all data with an additional ground station (Concept B).

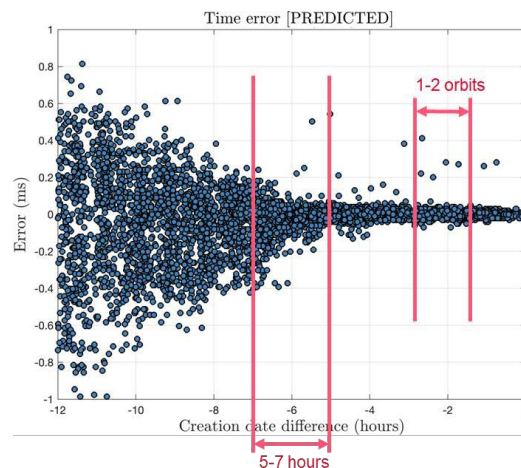


Figure 5.12: Start time prediction error as a function of the time ahead of the observation the orbit was predicted. The error corresponding to a 5-7h prediction timeframe is $19\mu s \pm 0.08ms$. When used in an overall error budget to take into account other sources of error, an overall timing error of 1.3 ms is obtained, well below the required 3 ms.

5.3.2 Optical Instrument

The instrument is a multi-spectral imager operating in the Thermal Infra-Red (TIR) region of the spectrum. Both studies provide instrument concepts that share several characteristics, and differ on some specific elements. In both Concept A and B, the requested 5 views are covered using five replicas of the same camera unit, mounted on an optical bench with an angular offset. The mechanical accommodation for both concepts is shown in fig.5.13. The single camera units are based on refractive optics for both Concept A and B, with comparable aperture of respectively 72 mm and 67 mm, and the same f-number $F=1$. Both instrument concepts operate in a push-broom scanning approach, with optical filters mounted in proximity of the focal plane. Both studies use the ULIS PICO 1024 micro-bolometer detector, which has been designed specifically for the TIR bands and for operation at ambient temperature. Thermal imagers are sensitive to the surrounding thermal environment and hence require frequent calibration. Both concepts include a 2-points calibration approach, but with different strategies: Concept A employs two planar black-body sources that are rotated in front of the detector, whilst Concept B uses a black-body and deep-space views, made accessible with the use of a scanning mirror. The specified radiometric performance (PP-479, PP-282) requires oversampling and averaging techniques to reduce the noise from the detector. In Concept A an approach with temporal oversampling and digital Time Delay and Integration (TDI) has been proposed for this purpose. A risk retirement activity is ongoing to demonstrate the approach with tests on a breadboard. Also in Concept B digital TDI has been proposed. The skewed viewing geometry requires (on-board) resampling and processing of the images. The resampling algorithm has been developed in a risk retirement activity and is being tested on a data processing unit similar to the one being developed for the CHIME mission. The test set-up is shown in Figure 5.14. The Figure also shows that resampling is required to avoid severe degradation of the data.

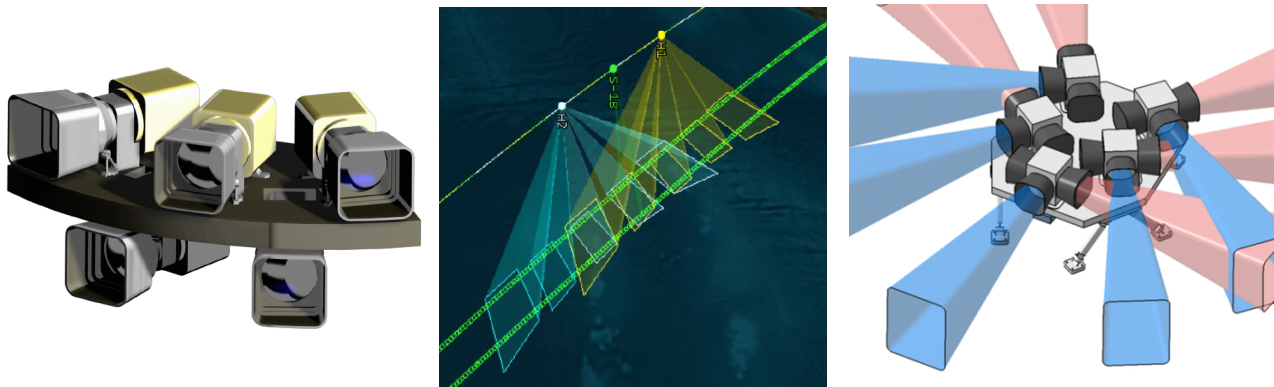


Figure 5.13: The optical payload accommodation for (Left) Concept A and (Right) Concept B. The middle view shows the footprints are skewed, which requires on-board resampling (Concept A).

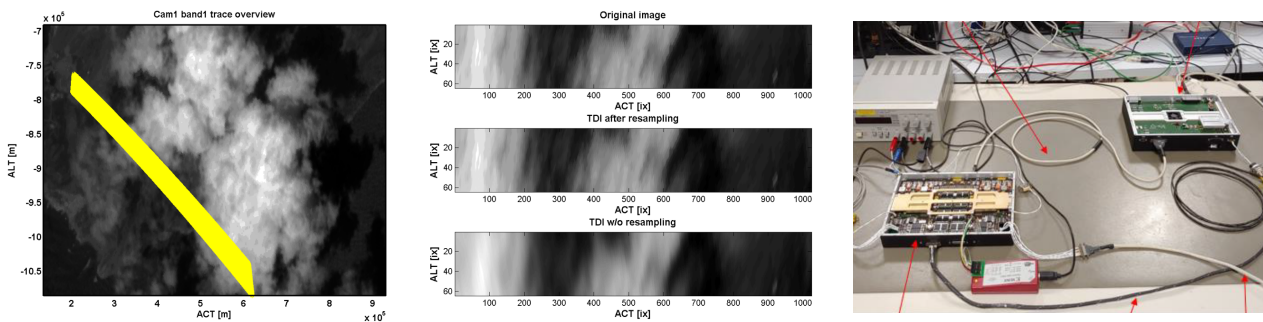


Figure 5.14: Testing of resampling algorithm. (left) Simulated test scene overlapped with detector trace. (middle) Comparison of TDI with and without resampling. (right) Test set-up to implement processing algorithm for Harmony.

5.3.3 Platform Architecture

5.3.3.1 Structure and mechanisms

The structure for Concept A is a straight re-use of the LSTM platform. The structure has a cuboid shape with a single central shear web. An additional structure is placed over the top panel to create sufficient clearance for the SAR instrument.

Concept B requires a custom structure design in order to facilitate the stacking of the two satellites in the fairing. The advantage is a better launcher capacity and more mass available for the satellites. The structure has a central Carbon Fibre Reinforced Polymer (CFRP) tube design which connects the satellites to the launcher via an adapter cone and an interface which allows the mounting of both satellites on top of each other.

Both solutions include Hold-down and Release Mechanism (HDRM)s for the Solar Array (SA) and the SAR antenna. The deployment mechanism for the SA will need to ensure a rotation with an angle of 30° around its longitudinal axis, in order to compensate the Harmony roll angle. This can be implemented with a simple hinge rather than a complex Solar Array Drive Mechanism (SADM) mechanism. In addition the Ka-band antenna for data downlink requires a pointing mechanism.

5.3.3.2 Thermal control

The main function of the thermal control subsystem is to guarantee the operating and non-operating temperature ranges for all the satellite components. Harmony is flying in the same dusk-dawn Sun Synchronous Orbit (SSO) orbit as S1, with clear hot and cold sides of the spacecraft and a stable thermal environment. The exception is during the summer months, between June and August, where eclipses are encountered. These are relatively brief, as their duration rises and falls linearly with the days, with a maximum duration of 18 minutes when the spacecraft is flying over the South Pole region.

Both concepts include a completely passive thermal architecture relying on Multi-Layer Insulation (MLI), radiators, heatpipes, and heaters for temperature control. Dissipation from the passive SAR antenna is not an issue.

The lateral SAR antennas will be exposed to the Sun, and thus the backside must be covered by MLI to ensure a constant thermal environment. Depending on the antenna design, the effects from Thermo-Elastic Distortion (TED) may cause slow variations in the antenna pattern over timescales of an orbital period. This in turn will cause systematic signals in the measured LoS velocities. The impact of TED on the USV accuracy will have to be studied in detail in the next phase. The SAR antenna for Harmony will in any case be designed so it has a minimum susceptibility to TED. Active heater control for the antenna is not being considered at present, as it would require a significant amount of heater power.

The thermal design of the TIR instrument will present some challenges. The instrument is mounted on the eclipse side of the spacecraft, while heaters finely control the temperature stability. The thermal design of the optical payload will require careful attention.

5.3.3.3 Power and energy storage

The baseline electrical power subsystem will use a standard approach for the generation, storage and management of the spacecraft's power. The EPS uses a solar array for power generation and Li-ion batteries as power storage. The solar generator is based on a deployable fixed solar array optimized in regards to the orbit and the attitude law to assure efficient power generation throughout the mission.

For both solutions, the solar array will be rotated with an angle of 30° around its longitudinal axis. For Concept A, the SA is downsized to 4 m^2 from the LSTM SA size of 6 m^2 , which means it will have 2 panels rather than 3. For Concept B, the SA has an area of 7.1 m^2 .

5.3.3.4 Payload Data Handling and Transmission (PDHT)

In order to transfer the payload data volume to ground (see Table 5.4), both concepts foresee a single-channel Ka-band system with steerable Medium gain Antenna (MGA). The effect of the mechanical steering on the pointing knowledge will have to be assessed. Concept A includes a 32 bit APSK modulator, capable of delivering 1.85 Gbps to Svalbard. Concept B includes a more advanced Variable Coding and Modulation (VCM) scheme with a data-rate varying between 1750-2225 Mbps (depending on the elevation angle). The size of the mass memory is 4 Tbit EOL for Concept A and 8 Tbit for Concept B.

5.3.3.5 Telemetry, tracking and command

The TT&C subsystem for Harmony consist of an S-Band TT&C link, which provides the S-Band communication capabilities between the satellite and the ground station, and (for Concept

B) an inter-satellite link to exchange navigation data during the close formation phases. Harmony uses a flight-proven heritage S-Band TT&C system thus allowing to establish communications with the Harmony spacecraft in each mission phase, from Launch and Early Orbit Phase (LEOP) to End of Life (EOL).

5.3.3.6 Attitude and orbit control

A standard attitude control system for 3-axis stabilised satellites is envisaged for both of the Harmony satellites. Two points stand out that are specifically required for Harmony:

- A high performance gyro and high precision star trackers are required to provide the best possible attitude knowledge.
- GNSS receivers shall be used that are compatible with common-clock synchronisation with S1.

5.3.3.7 Propulsion

A conventional hydrazine system is proposed for both Concept A and B, with a pressurized tank of 198 l (Concept A) and 96 l (Concept B). Concept A includes 4x 20 N thrusters. Concept B includes 3+3 Orbit Control System (OCS) thrusters for orbit control as well as an additional 8+8 Reaction Control System (RCS) thrusters for attitude control, in a force-free configuration to eliminate parasitic delta-v.

5.3.4 Satellite Configuration and Budgets

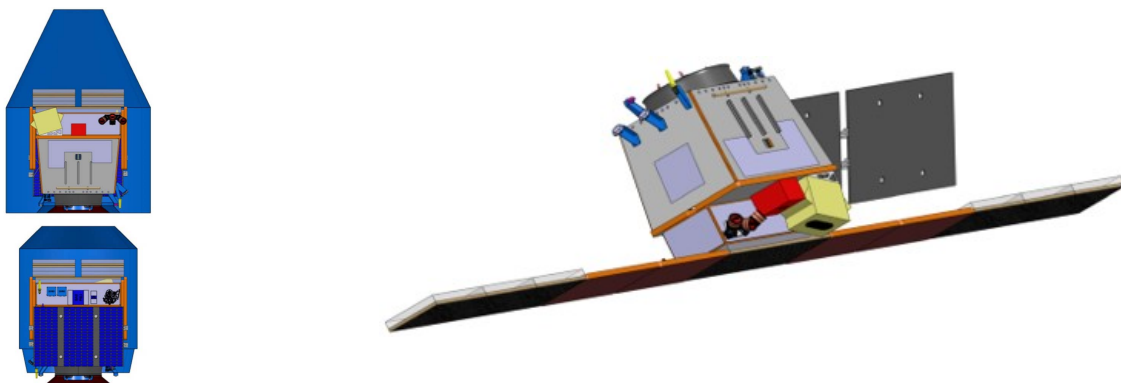


Figure 5.15: Concept A configuration stowed (left) and deployed (right).

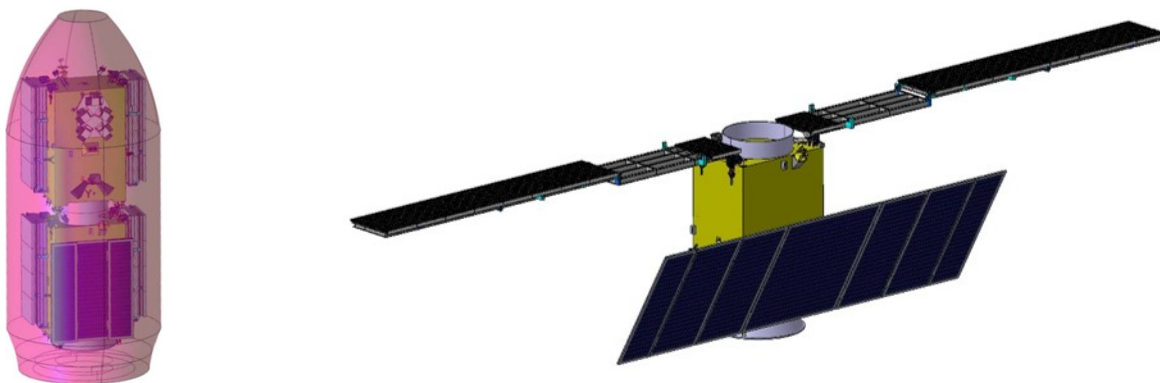


Figure 5.16: Concept B configuration stowed (left) and deployed (right).

Table 5.1: Average power consumption in Nominal Mode for concepts A and B.

	Concept A	Concept B
	[W]	[W]
Platform	460	622
SAR instrument	201	185
Optical instrument	60	21
Other	63	
Total satellite	784	828
Total satellite inc. system margin	941	993

Table 5.2: Mass budget for concepts A and B.

	Concept A	Concept B
	[kg]	[kg]
Platform	445	387
SAR instrument	207	374
Optical instrument	47	61
Dry total	700	822
Dry inc. system margin	840	987
Propellant A+B	266	114
Total A+B	1945	2088
LVA	455	95
Total launch mass	2400	2183
Launcher capability to target orbit	2470	2225
Margin	3%	2%

Table 5.3: Delta-V budget for concepts A and B.

	Concept A	Concept B
	[m/s]	[m/s]
LEOP	33	32
Orbit raising	161	
Station keeping	55	26
Formation transfer	17	15
Collision avoidance	2	2
Formation collision avoidance	3	
Uncontrolled re-entry	20	30
TOTAL	291	105

Table 5.4: Data volume budget for concepts A and B.

	Concept A			Concept B		
	Data Rate [Mbps]	Min/orbit	Data vol/orbit [Tbit]	Data Rate [Mbps]	Min/orbit	Data vol/orbit [Tbit]
IW	1192.4	15.1	1.08	1933.2	8.9	1.03
EW	360.6	8.5	0.18	518.4	7.6	0.24
WV	355.2	2.9	0.06	233.7	18.6	0.23
Optical	67.6	18.6	0.08	188.7	16.5	0.19
TOTAL			1.40			1.69

5.4 Mission Performance

In order to link the design to achievable performances, detailed error trees, analysis tools and error budgets have been developed. In this Section the performance evaluation against the most driving performance requirements is reported for both concepts A and B.

5.4.1 SLC performance

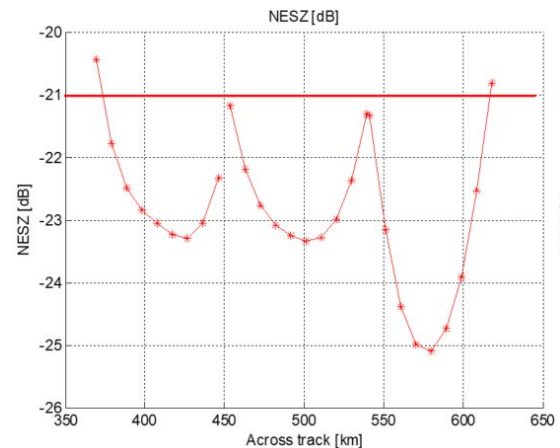
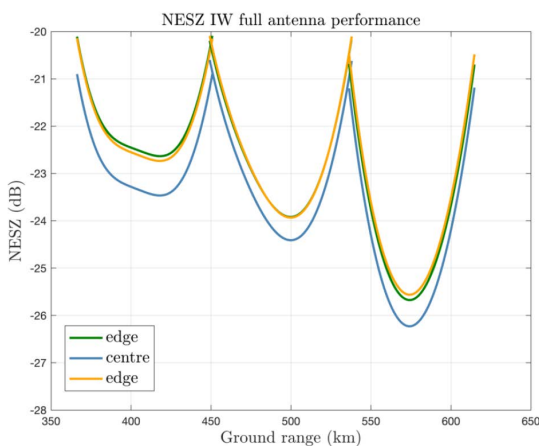


Figure 5.17: SLC SAR image performance for the three sub-swath in the Interferometric Wide Swath Mode in terms of sensitivity (NESZ) for the full antenna in Concept A on the left and in Concept B on the right.

Figure 5.17 shows the NESZ performance for the IW mode when using the full antenna (three sub-apertures combined). If the data from the three sub-apertures is downlinked to ground (as is the baseline for Concept B), then the sensitivity can be further improved by applying azimuth beamforming between the three phase centers in the SAR processor. The worst case NESZ performance is better than -20 dB for Concept A and -21 dB for Concept B. For both concepts, the worst case DTAR in IW mode for the full antenna is better than -17 dB, which is not compliant to the specified -19 dB. This non-compliance is expected to be tolerable as the total ambiguous signal is dominated by the azimuth ambiguities (range ambiguous are very small, namely, below -20dB). Further work is required to reduce these with ground processing.

5.4.2 USV performance

One of the key requirements placed on the USV product is the RPE on each vector component, specified over 50 km scales. Detailed error budgets have been developed and show that the RPE over short timescales is dominated by the interferometric noise, which in turn is determined mainly by the antenna design. Figure 5.18 shows the USV precision distribution for both low-wind and high-wind scenario's, in IW mode for Concept A. The analysis takes into account the antenna performance, polarisation, synchronisation errors, antenna stability errors, spacecraft attitude, stereo baseline and retrieval effects such as back-scatter statistics and temporal decorrelation due to ATI time-lag and sea state. Figure 5.19 shows the USV precision of Concept B over the swath. In IW mode, Concept A is marginally non-compliant, while Concept B is fully compliant. In EW mode both concepts are non-compliant. For Concept B an improved Doppler estimation technique (multi-channel DCA) has been developed that would allow it to reach compliant USV performance also in EW mode. This work will be further consolidated.

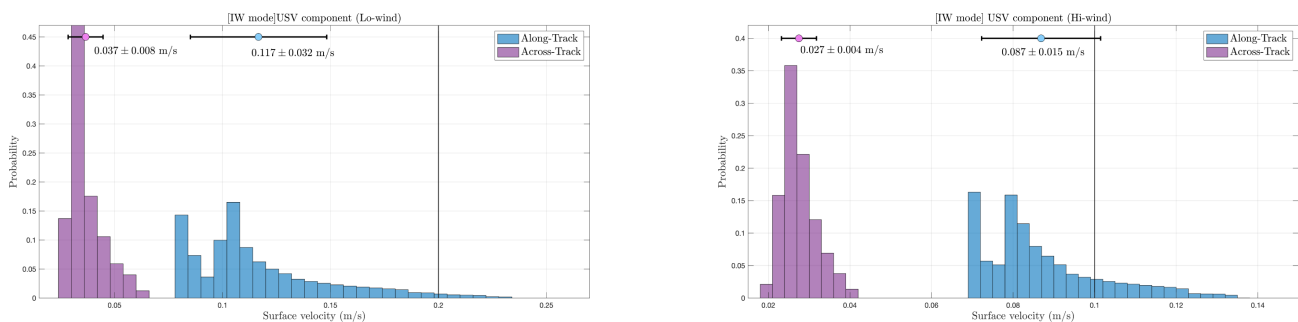
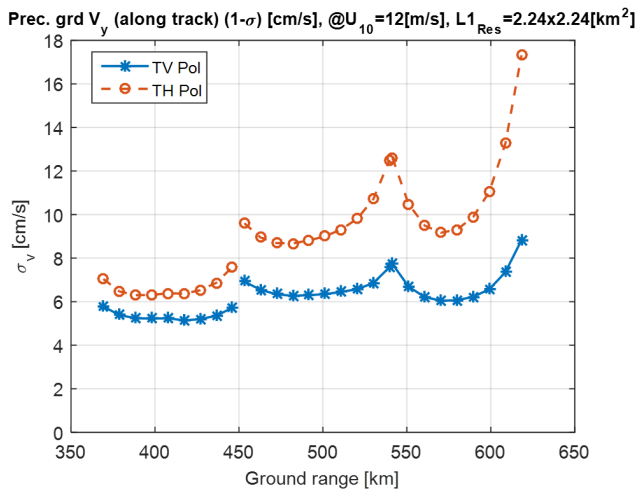


Figure 5.18: Distribution of simulated USV precision with climatology data for winds and a Small Slope Approximation (SSA) backscatter model (along-track in blue and across-track in purple). (left) Performances in low-wind conditions (4 m/s and below) are 5 cm/s across-track and 15cm/s along-track. (right) Performances in high-wind conditions (12 m/s and above) are 3cm/s across-track and 10 cm/s along-track. Tails in the distribution are caused by reduced performances in subswath overlaps. Requirements shown in black lines. These results assume IW mode and vertical polarisation on transmit. WV mode performs significantly better. (Concept A)

5.4.3 TOC performance

The performance analysis for the TOC product takes into account instrument contributions (thermal noise, ambiguities, polarisation effects), synchronisation errors, formation flight contributions (spectral shift, baseline errors) and propagation effects (volume decorrelation and penetration). The performance requirements have been assessed for the different RoI corresponding with volcano regions, permafrost regions and land ice regions. For each point the actual latitude (and thus Height of Ambiguity (HoA) and Doppler shift) has been computed and the σ_0 value has been retrieved from a map compiled with real S1 data shown in Figure 5.20. The total number of SPI products in the stack takes into account the different revisit times as a function of the latitude. The performance computations assume an incidence angle of 38° (mid point of IW2 subswath) and the average NESZ, Azimuth Ambiguity to Signal Ratio (AASR) and DTAR of the instrument in full antenna configuration. TOC products



	OCEAN - Low wind (4 m/s) Req: 20 cm/s @25 km2		OCEAN - High wind (15 m/s) Req: 10 cm/s @5 km2	
	vx [cm/s]	vy [cm/s]	vx [cm/s]	vy [cm/s]
WV1 TV Pol	1	2	2	3
WV2 TV Pol	1	4	1	3
IW1 TV Pol	3	8	3	6
IW3 TV Pol	4	18	3	9
EW1 TV Pol	7	12	8	12
EW5 TV Pol	5	19	5	16

Figure 5.19: (left) USV precision plotted over the IW swath for the high-wind scenario and (right) summary of performances obtained with different modes and subswaths. All results obtained with ATI. (Concept B)

with different resolutions have been assessed and volume penetration assumed to be 20m for land ice, 10m for permafrost, and 0m for volcanoes/landslides. For volcano regions the derived products will not benefit of stack processing and will be available every 12 days. In this case the assumed perpendicular baseline is taken as an average value for volcano locations spread over latitudes values lower than +/-60°.

Two examples of the various cases analysed are shown in Figure 5.21 for land ice. An overview of the analysis results for all cases considered is shown in Table 5.5. The results demonstrate that in IW mode the TOC height accuracy over land ice regions will be compliant with the 0.5 m/yr (PP-34) for a product pixel size of 50 m (PP-33, goal). With a resolution of 100 m (PP-33), an accuracy of 0.2 m/yr (PP-34, goal) is achievable. Over permafrost regions, TOC height accuracy is compliant with 0.5 m/yr (PP-183) in IW mode, but in EW mode that is not the case at the swath edge. With 100 m resolution (PP-182) the accuracy is better than 0.5 m/yr everywhere over the EW swath.

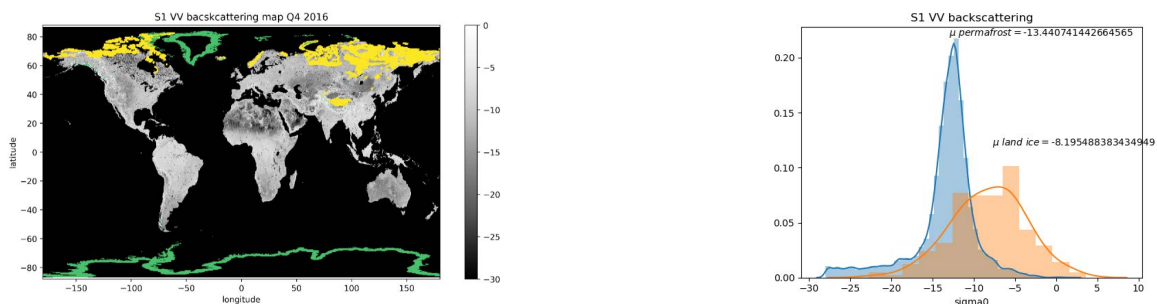


Figure 5.20: (Left) S1-VV backscattering map with Permafrost region mask overlaid in yellow and land ice region in green region. (right) Histogram of the backscattering for permafrost and land ice regions. (Concept A)

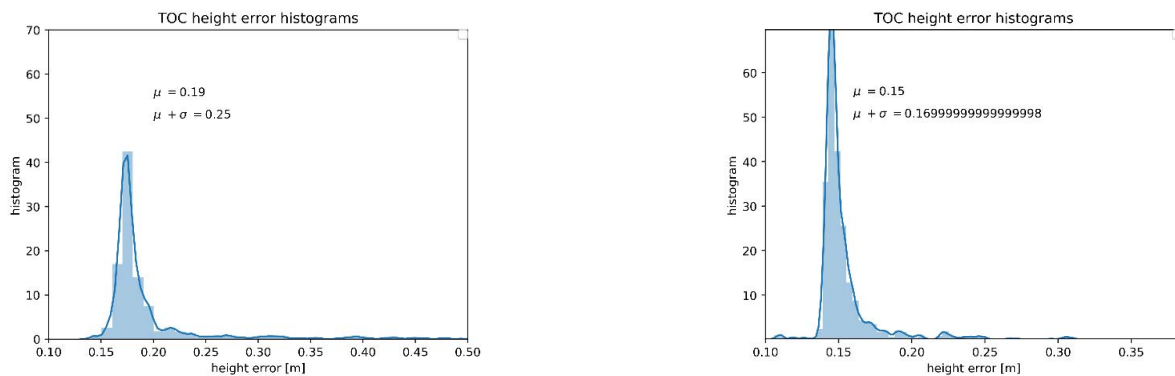


Figure 5.21: (Left) TOC Land ice product height accuracy in IW mode with average NESZ and DTAR , a product resolution of 50x50m² and volume penetration of 10 m. (right) The same TOC product for a resolution of 100x100m². (Concept A)

Table 5.5: TOC height accuracy for the three different RoI (volcanoes, land ice and permafrost). For the latter two results are shown for 50m and 100m product resolutions, and for IW and EW mode. Each time the figures for average and worst case are listed. (Concept A)

	TOC _volcano 30m		TOC land ice 50m		TOC land ice 100m		TOC permafrost 30m		TOC permafrost 100m	
Imaging mode	Worst case	Average	Worst case	Average	Worst case	Average	Worst case	Average	Worst case	Average
IW	1.20m	0.87m	0.3 (IW3)	0.19	0.19 (IW3)	0.15	0.21 (IW3)	0.13	0.13 (IW3)	0.11
EW	NA	NA	1.2 (EW1)	0.46	0.67 (EW1)	0.18	0.94 (EW1)	0.26	0.48 (EW1)	0.12
Worst case:	Worst NESZ, TAR in the swath and mean+sigma of results over locations									
Average :	Average NESZ, TAR in the swath and mean result over locations									

5.4.4 TDV performance

The retrieval of TDV is based on repeat-pass differential Interferometric synthetic aperture radar (InSAR) techniques to compute surface deformation from a stack of interferometric acquisitions after removal of the atmospheric and topographic components. Interferograms from both followers and from S1 are used. To serve the different science goals, different requirements are formulated in terms of sampling and spatial resolutions, of which the most challenging are the strain rate requirements (PP-20,PP-22,PP-458).

As for the TOC product, a detailed error model has been set up to evaluate the performances of the TDV product, taking into account the L1 performances of the system, but also the geophysical noise from the atmosphere. Figure 5.22 provides the results of the TDV deformation velocity accuracy over the strain RoI, in this case for 3 years of stereo configuration with 3 LoS (the two Harmonies and S1) per overflight. It can be seen that both E-W and U-D components will meet the 1 mm/yr goal requirement (PP-24) in the full mask, while the uncertainty on the N-S component is around 2mm/year (threshold requirement PP-458). Even though the observation geometry is more favourable at lower latitudes, the larger number of acquisitions at higher latitudes explain the better performance there. TDV products can also be obtained while Harmony is flying in an XTI configuration. Note, however, that the accuracy of the N-S component is significantly better during the stereo phase due to the larger angular diversity between the LoS when compared to the XTI phase. In general, though, the good accuracy in the N-S component is explained by the high correlation between the atmospheric noise terms

among the Harmonies and S1 LoS, which cancel out almost completely. This is a key advantage of Harmony’s stereo configuration for observing the N-S component of the deformation.

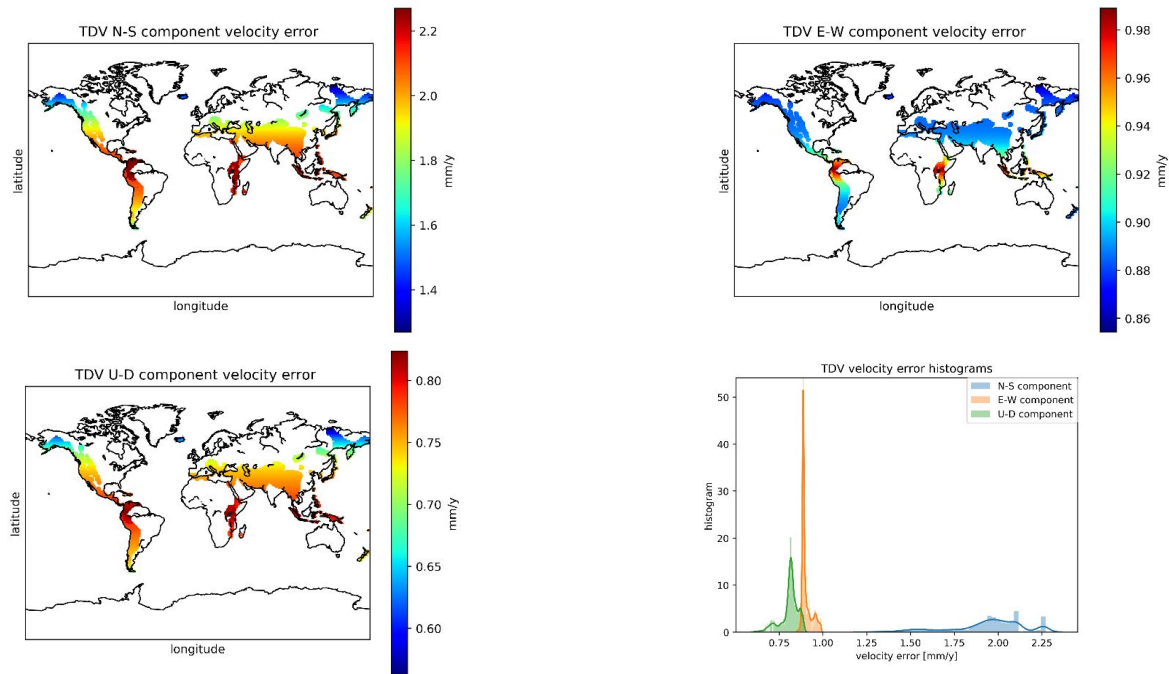


Figure 5.22: Average swath TDV uncertainty over the strain RoI. North-South component (top left), East-West component (top right), Up-Down component (bottom left) and the histogram of error for each component (bottom right). Results are shown in mm/yr considering a 100m resolution product and 3 years in stereo observation. (Concept A)

5.4.5 TAR performance

The main performance requirements for the TAR product are the spatial resolution (PP-475, PP-288, PP-476), and the radiometric sensitivity expressed as NEdT (PP-282,PP-479).

Both concepts have a compliant design with respect to spatial resolution (defined as the Full Width at Half Maximum (FWHM) of the Point Spread Function (PSF)). The optical design of both concepts achieves an across-track swath for the central view close to 260 km.

In Concept A the compliance to the threshold NEdT is achieved for all bands using both temporal averaging and spatial binning. The performance figures are obtained with some simplified assumptions, and a consolidation of the current budget is expected for the next study phase. For Concept B compliance to the threshold NEdT is achieved for band CD-1 and PAN, with a combination of temporal averaging and spatial binning where possible, while the other bands show an NEdT slightly non-compliant, as shown in Fig.5.23. The NEdT figures are obtained with a conservative approach, and the model will be refined in the next phase of the study.

Both studies have addressed the retrieval algorithm for SST using multi-view approach, similar to Sentinel-3 SLSTR, in a split-window scheme using the 11 μm and 12 μm channels. For Concept A, the SST retrieval algorithm is studied by University of Reading. The study

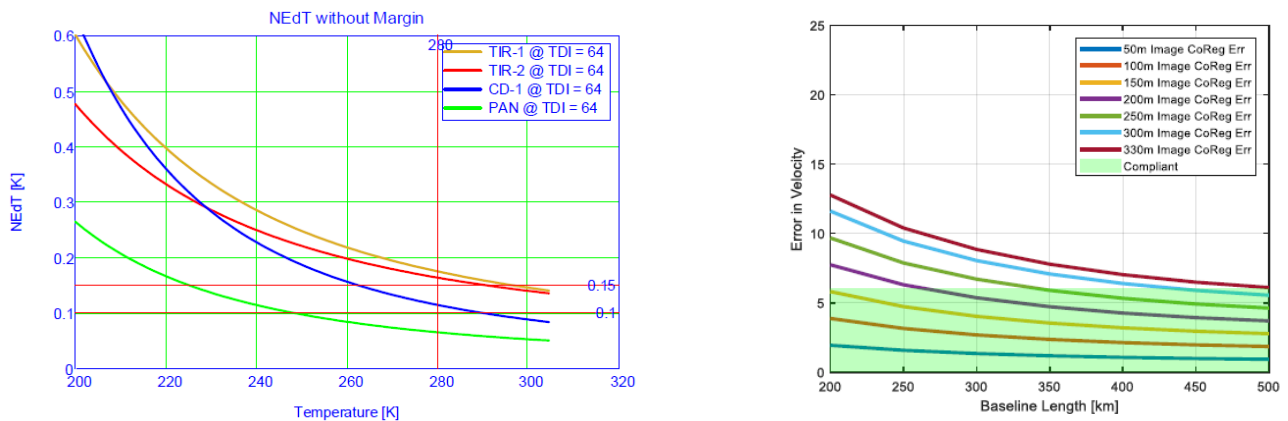


Figure 5.23: (left) Results for Concept B for NEdT performance for the 4 spectral bands, for different ground temperatures. (right) Results for Concept A analysis of CMV performance.

shows that the SST gradient is not particularly affected by the absolute calibration of each TIR camera, which impacts the absolute SST retrieval, but mostly by the NEdT value. Using 3 cameras per spacecraft, and with calibration accuracy of 1 K, an NEdT of 0.1 K translates into an uncertainty for the SST in the range 0.3-0.4 K, and an uncertainty in the differential SST of 0.15-0.35 K, with variability depending on the value of the inter-calibration accuracy between the cameras. The Concept B study reviews several retrieval schemes, and evaluates the possibility of using also the $8.6 \mu\text{m}$ band in addition of the split-window scheme, finding no particular advantage. An uncertainty of 0.5 K for the SST is considered feasible with NEdT of 0.12 K.

The CMV performance has been evaluated for both concepts, and compared with the required values (PP-165, PP-166, PP-167). The analysis for the cloud motion vector accuracy was carried out in both Concept A and Concept B study using the approach developed for the MISR mission concept, which used a similar multi-view detection geometry to measure winds through cloud motion. Additionally, in the Concept B study the optimal set of 3 views to be used for CMV retrieval was also investigated. The analysis highlights how the CMV performance depends on the geometric calibration error of the TIR cameras. The required camera co-registration is a function of the baseline distance (distance between the Harmony spacecraft and Sentinel-1). The results show that the mission requirements for CMV are feasible for the considered baselines, with required camera co-registration in the order of 0.5 of the PAN sampling distance, as reported in Fig.5.23 for Concept A, considered feasible in the Harmony context.

5.5 Ground Segment and Operations

5.5.1 Ground segment architecture and options

A typical Earth Explorer Ground Segment (G/S) uses generic components configured or adapted to each mission. Following this approach, the Harmony G/S consists of two main components, the FOS and the PDGS. The FOS includes the S-band Telemetry Tracking and Command (TT&C) ground stations and the Flight Operations Control Centre (FOCC) in ESOC. The function of the PDGS is to receive the science data from the satellite via dedicated ground stations, the application of the processing algorithms and the delivery of data products to the

users.

For each concept, two possible architectures are proposed for the Harmony ground segment. Concept A considers two options for the PDGS. Option 1 is to have a separate PDGS for Harmony and interface it with that of S1. Option 2 is to have one integrated PDGS for both S1 and Harmony. The FOS for Harmony is in any case kept separate and interfaces that of S1. Concept B also considers two options, whereby option 1 is to have a separate G/S for Harmony (similar to Concept A) and option 2 is to have both the FOS and PDGS fully integrated. Of course hybrid solutions between those options are possible, and detailed trade-offs will be performed in Phase A for all of the G/S functions. The description in this Section is based on Concept A.

5.5.2 FOS functionality and interfaces

Functions of the FOS are discussed only in so far they are specific to the Harmony mission or relevant to the interface with S1.

On Ground Monitoring and Control. Harmony will require the following extra routine operations:

- Command the S1 predicted orbit every 12 hours when received from Constellation Coordination in order to establish coarse time synchronisation of the SAR instrument on Harmony.
- Command station keeping on weekly basis with inputs from Flight Dynamics.
- Command collision avoidance manoeuvres if indicated by the Constellation Coordination function.
- Monitor the (propagated) footprint overlap between S1 and Harmony with inputs from Constellation Coordination and Flight Dynamics.

Mission Planning. Harmony will require the following extra routine operations:

- Plan station keeping manoeuvres in coordination with S1. While it is not required to align the manoeuvres with Sentinel 1 (performance requirements are met as long as Harmony stays within a 100m orbital tube), this approach is likely to be beneficial.
- Plan required formation reconfiguration with inputs from Constellation Coordination function.

On Ground Automation. Harmony will require automated functions to monitor the relative geometry between the Harmony satellites during the XTI phase.

Constellation Coordination. A Constellation Coordination function is required to manage the loose convoy flight with S1 as well as the formation flight between the Harmony satellites during XTI phase. This function includes:

- POD-based coarse time synchronisation. Requires daily interfacing and special coordination before S1 manoeuvres.
- Formation flight monitoring (control box violation and baseline monitoring)
- S1/Harmony collision avoidance

- Coordinated collision avoidance with foreign object

In order to implement these functions, the Harmony FOS requires the following interfaces with the S1 G/S:

- Sentinel-1 POD prediction files with 3h prediction of state vectors
- Planned manoeuvres and expected outages from Sentinel-1 FOS
- S1 orbit relevant parameters (mass, ballistic coefficient, etc) for orbit propagation
- Mission planning parameters (acquisition start times, acquisition mode, etc.)

5.5.3 *PDGS functionality and interfaces*

A functional diagram for a PDGS concept corresponding with option 1 (separate PDGS) is shown in Figure 5.24. The diagram also shows the main building blocks and interfaces to the PDGS: the Harmony production system (purple), the SAR processors (orange), the data handling components (grey), the production management (yellow), the Harmony satellite interface (blue), the Sentinel-1 elements (satellites, FOS and PDGS) (red) and the Harmony FOS elements (green). The data required from the S1 PDGS is listed below. With the expected evolution of the Copernicus PDGS to cloud-based infrastructure, the data will be available via simple downloads over the Internet (with the exception of the antenna model).

- **Precise S1 orbit:** Orbit auxiliary data contain information about the position of the satellite during the acquisition of SAR data. There are three types of orbit auxiliary data: Precise Orbit Ephemeris, Restituted Orbit, and Predicted Orbit.
- **Precise S1 attitude:** Attitude auxiliary products contain information about the pointing of the satellite during the acquisition of SAR data.
- **GNSS raw data**
- **Tagging data:** Time in GPS basis of the pulses. The Level-0 (LO) datation algorithm computes the time-tag of the measurements.
- **Headers of the ISPs:** Primary and secondary headers extracted from SAR Instrument Source Packets (ISP) stream.
- **S1 noise pulses:** Noise pulses extracted from SAR ISP stream.
- **Lo cal products**
- **Internal Calibration products**
- **External Calibration products** Used to correct and calibrate the imagery during processing: azimuth and elevation antenna pattern, azimuth antenna elements pattern, absolute calibration constant, noise calibration factor.
- **S1 antenna model**
- **L1 product** SLC products. (Depends on S1 processing being performed in Harmony PDGS.)
- **L1 product annotations** Timing(range,azimuth), Orbit (Depends on S1 processing being performed in Harmony PDGS.)

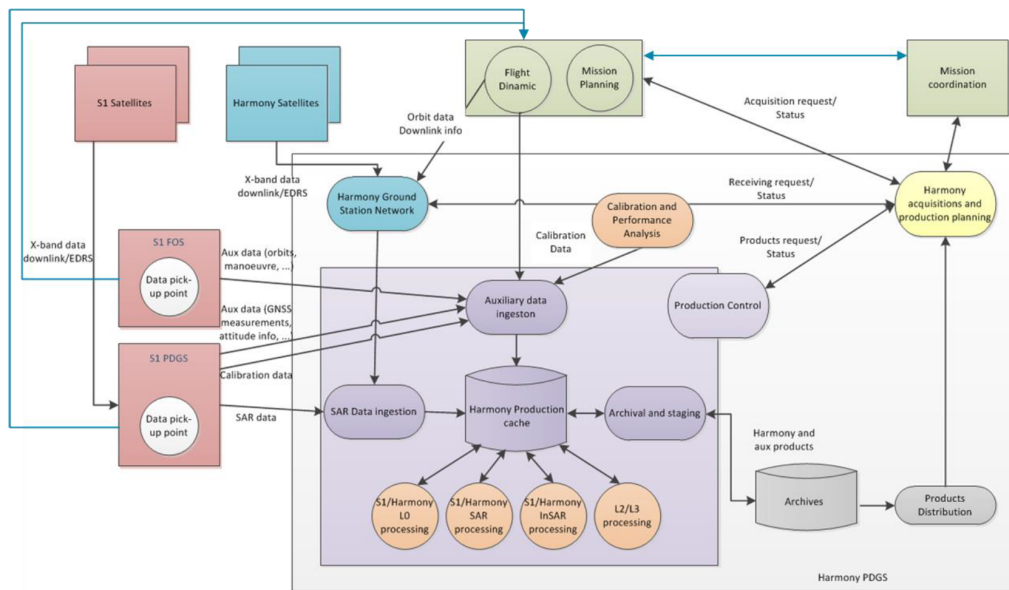


Figure 5.24: Functional diagram of the Harmony PDGS and its interfaces. (Concept A)

5.5.4 Data downlink strategy

Table 5.4 shows the data volumes produced by the payload over one orbit, for both concepts. The budgets assume that the optical instrument is always on over the ocean (no vignetting) and that wave mode is always on (with vignetting). In addition to the RoI to be imaged over the ocean, the profile for Concept A assumes all land areas are observed when S1 is observing them (including permafrost areas). The budget for Concept B assumes the mask shown in Figure 5.5 which equates to slightly lower duty cycles. On the other hand, Concept B has 3 phase centres in the SAR antenna. The reason that the WV data rate is not higher for Concept B is because single polarisation has been assumed. With those assumptions, the total data volume for Concept A is 1.4 Gbit/orbit and for Concept B it is 1.7 Gbit/orbit. These data volumes are produced when Harmony is flying in stereo configuration. When Harmony is in XTI configuration, only land targets are imaged, and the data volume is roughly halved. Both concepts have baselined a single-channel Ka-band Payload Data Handling and Transmission (PDHT) system and have assumed 1 or 2 high latitude ground stations. As described in 5.3.3.4, the PDHT in Concept B has the highest throughput. With this system all data can be downloaded to the Svalbard ground station if each Harmony could use the full duration of a pass. In stereo mode the Harmony satellites fly far enough apart so that with two dishes in Svalbard each can indeed use the full duration of a pass. The approach proposed for Concept A, which has a lower data rate, is to augment the ground segment so that three dishes are used, two in Svalbard and one in Inuvik. The dish in Inuvik is time-shared between the Harmony satellites: the station will communicate with the leading Harmony for half a pass, then stop, and wait for the second Harmony to come into view for the remaining part of the pass. In XTI mode, the Harmony satellites fly too close and they must either time-share the Svalbard station, use different ground stations, or use another multiplexing technique. Time-sharing a single dish in the Svalbard station reduces the average downlink time by approximately 38%. The reduction in data volume during the XTI phase is expected to be greater than that, so that for both stereo and XTI phases a satisfactory solution exists.

5.5.5 Mission timeline and disposal

Half a year of LEOP and commissioning is planned prior to start of nominal operations. For Concept A the baseline is to launch into a 400km orbit, and raise the orbit to that of S1. This strategy was chosen to maximise the available launch mass. For Concept B the baseline is to launch 20 km below the S1 orbit for safety reasons.

The baseline mission plan for Harmony is to spend one year in XTI formation, switch into stereo formation for a duration of three years, and switch back to XTI formation for one year. This plan has been assumed to calculate the performances for the various products. Since the plan will be fine-tuned in Phase A, and to allow more XTI observations, the system has been sized to allow for two XTI reconfigurations per year, during the three years of stereo formation.

The EOL phase will passivate the satellite and guarantee a safe re-entry compliant with ESA guidelines. The spacecraft will lower its perigee to guarantee an un-controlled re-entry within 25 years, requiring a delta-V of less than 30 m/s. The platform and the payload will be designed to demise in order to assure the casualty risk is maintained within the ESA space debris mitigation requirements.

6 DATA PRODUCTS AND USAGE

Table 6.1 provides a concise summary of the main products for the SAR instruments to be delivered by the Harmony PDGS. The products have also been defined to support the requirement definition, which has been outlined in Figure 4.1 in Chapter 4.

Table 6.1: Summary of Harmony main data products for the SAR instruments to be generated by the PDGS.

Level	Product	Short description
L0	Lo-SAR	Decompressed, reconstructed, unprocessed Instrument Source Packets (ISPs) after restoration of the chronological data sequence for the instrument with all supplementary information to be used in subsequent processing (e.g. orbital data, health, time conversion, etc.) appended, after removal of all communication artefacts (e.g., synchronisation frames, communications headers, duplicated data, compression coding...). Level 0 data are time-tagged. The precision and accuracy of the time-tag shall be such that the measurement data can be geo-located to an accuracy compatible with the mission requirements. The data shall include identification of the spacecraft, the observation mode and the sub-swath.
L1		Level-1 products are geo-referenced using orbit and attitude data from the satellite and time tagged with zero Doppler time at the centre of the swath. Geo-referencing is corrected for the azimuth bi-static bias by taking into account the pulse travel time delta between the centre of the swath and the range of each geo-referenced point.
L1a	L1-SLC	SLC products are images in the bistatic range by azimuth imaging plane, in the image plane of satellite data acquisition. Each image pixel is represented by a complex (I and Q) value and therefore contains both amplitude and phase information. The processing for all SLC products results in a single look in each dimension using the full available signal bandwidth. They contain two orthogonal polarisations. The data is radiometrically calibrated and synchronisation errors have been corrected.
L1b	Co-Registered SLCs	Single-pass pairs of co-registered Harmony SLC images. The data is radiometrically calibrated and synchronisation-related errors have been corrected. This product is relevant in close-formation phases as an entry point to single-pass InSAR processing.
L1c	L1-SPI	Multi-looked and interferometrically calibrated single-pass interferograms, coherences, and intensity images, thus all unique information-containing elements of the covariance matrix.

L1c	L1-USV	Geophysical equivalent surface velocity (see annex for detailed definition). Here systematic errors due to pointing uncertainties, synchronisation errors, etc, have been corrected. Residual uncertainties are annotated. This product will include geophysical biases such as wave bias. The L1- USV product contains two components of the surface velocity vector.
L2	L2-GRD	Sets of geolocated gridded calibrated intensity images, containing two polarisations, and 3 views (1 monostatic from Sentinel-1 and two bistatic).
L2	Single-pass DSM	Geocoded Digital Surface Model generated from L1-SPI product.
L2	L2-OCN-SCV	The SCV product contains the Total Surface Current Vector data for TBD polarimetric combinations. It is generated by combining observations from Sentinel-1 and the Harmony companion satellites. Geophysical biases will be annotated as separate correction terms.
L2	L2-OCN-SWV	Estimated Surface Wind vector combining observations from Sentinel-1 and the Harmony companion satellites. The product contains the horizontal 2D wind vector field U10S, as well as its divergence and vorticity.

There are a number of mission output products that may be produced more effectively through interaction with the users by using, e.g., a mission algorithm and analysis platform. The more relevant suited for these are listed in Table 6.2.

Table 6.2: Level-3 products for the SAR instruments envisaged to be produced outside the Harmony PDGS.

Level	Product name	Short description
L3	Combined Topography	Surface topography. Obtained after optimally combining (averaging) a TBD number of acquisitions, compensating for penetration depths and other geophysical biases.
L3	TOC	This can be seen as changes of the DSM height, which could be derived directly from the time-series of DSM produced by the PDGS. However, better results are achieved if application and location specific methods are used.
L3	TDV	Retrieval of 3D deformation velocity requires the combined use of Harmony and Sentinel-1 time series and specific adaptation depending on the thematic application.

Table 6.3 provides a concise summary of the main products for the TIR instruments to be delivered by the Harmony PDGS.

Table 6.3: Summary of Harmony main data products for the TIR instruments to be generated by the PDGS.

Level	Product name	Short description
Lo	Lo-TIR	Decompressed, reconstructed, unprocessed Instrument Source Packets (ISPs) after restoration of the chronological data sequence for the instrument – split for each view and band – with all supplementary information to be used in subsequent processing (e.g. orbital data, health, time conversion, etc.) appended, after removal of all communication artefacts (e.g., synchronisation frames, communications headers, duplicated data, compression coding...). Level 0 data are time-tagged. The precision and accuracy of the time-tag shall be such that the measurement data can be geo-located to an accuracy compatible with the mission requirements.
L1a	L1a-TIR	Level 0 data with corresponding radiometric, spectral and geometric (i.e. Earth location) correction and calibration computed and appended, but not applied.
L1b	L1b-TAR	Non-resampled Level-1a data, radiometrically calibrated, spectrally & geometrically characterised, annotated with satellite position and pointing, landmarks and preliminary pixel classification (e.g. cloud, water). The Level 1b product consists of Top of Atmosphere (TOA) brightness temperatures (K).
L1c	L1c-TAR	Level-1b data resampled to a specified grid.
L2	L2-SST	Sea Surface Temperature product including cloud-flagging
L2	L2-CMV	Altitude-dependent motion vectors derived from cloud tracking and multi-angle retrievals using both Harmony satellites. This product will deliver a cloud masking for the L2-SST product.

6.1 Data Processing

The Harmony data products are produced from data streams from both Harmony companions and Sentinel-1. Therefore, at all levels, the Harmony PDGS requires Sentinel-1 products as inputs. This leaves the choice to either ingest products from the S1 PDGS at levels 1 and 2, or to replicate the S1 processors inside the Harmony PDGS and only transferring Level-0 products from S1. This latter option would significantly reduce the required data volumes to be transferred and allow for a greater flexibility and consistency within the Harmony processing chain. This trade-off is in turn related to the chosen PDGS architecture and the level of integration with the S1 PDGS as described in Section 5.5.3, and will be further elaborated in Phase A. Regardless of the aforementioned architectural choices for the PDGS, the data products required from S1 can already be identified for both Land Ice / Solid Earth products and Ocean products. The SST and CMV products are generated from the Harmony optical payload and do not require any inputs from S1.

6.1.1 Ocean product data flow

The Harmony ocean products and processing will be based on combining L1 products from Harmony with the Sentinel-1 Level-2 Ocean (OCN) product from the S1 PDGS, as illustrated in Figure 6.1.

The OCN product is generated by the S1 Level-3 (L2) processor and contains three geophysical components: the Radial Velocity (RVL), the Ocean surface Wind field (OWI), and the Ocean Swell Wave spectra (OSW). The OSW component contains the cross spectra product similar to the Harmony Image Cross Spectra (ICS) product. The Harmony L1 COV and USV products require the combination of S1 and Harmony measurements of complex backscatter and radial velocities. The L2 processor requires from the S1 OCN product the OSW product and relevant ancillary data, and from the S1 L1 product the SLC product. The S1 OCN product includes collocated European Centre for Medium-Range Weather Forecasts (ECMWF) U10S wind vector as well as other ancillary data such as land masks and sea ice masks that are useful for the Harmony processor. Since S1 and Harmony are by construction collocated in space and time, there is no need to generate such information in the Harmony PDGS.

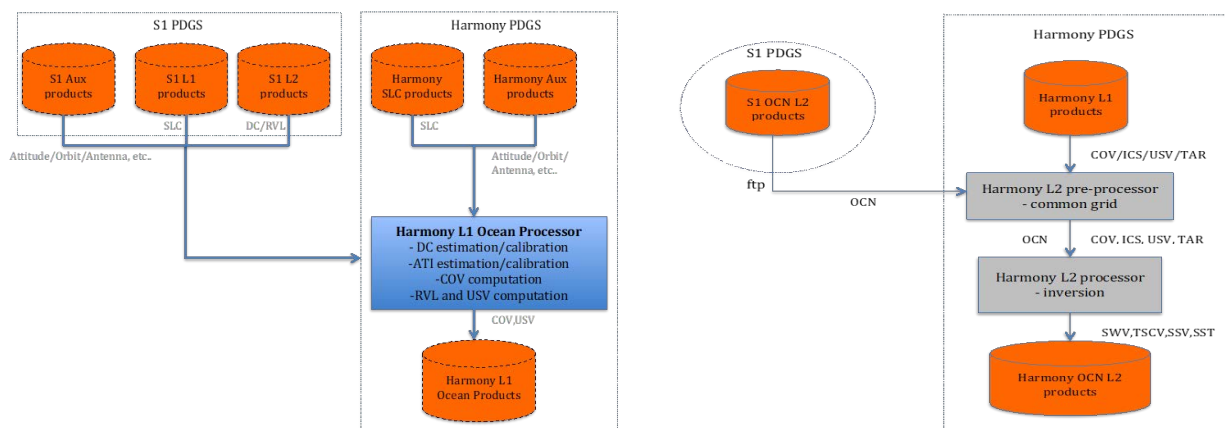


Figure 6.1: Data processing flow for ocean products at Level-1 (left) and Level-2 (right). (Concept A)

6.1.2 Land Ice / Solid Earth product data flow

In order to support the generation of TDV and TOC products, the Harmony L1 processor includes a Sentinel-1/Harmony joint bistatic processor and an interferometric (InSAR) processor (to be further detailed as RPI and SPI processors). Figure 6.2 shows a tentative data flow block diagram. The functional characteristics of the different stages can be summarised as follows:

- The LO processing is responsible for the processing of the instrument packets, e.g., sorting out the transmit or receive events, identification of corrupted echoes, and extraction of the different polarisations.
- The L1 processing involves internal calibration including time and phase synchronisation of the bistatic data sets, on-ground beam-forming stages of the bistatic data to improve the steering of the TOPS patterns, SAR processing, and interferometric SAR

processing, both in single-pass (e.g. for DEM generation) and in repeat-pass (e.g. for surface deformation).

- The L2/L3 processing involves the generation of the higher level products, such as DEM generation and calibration, topographic changes, or the estimation of LoS velocities and the inversion in the 3-D components for the areas of interest.

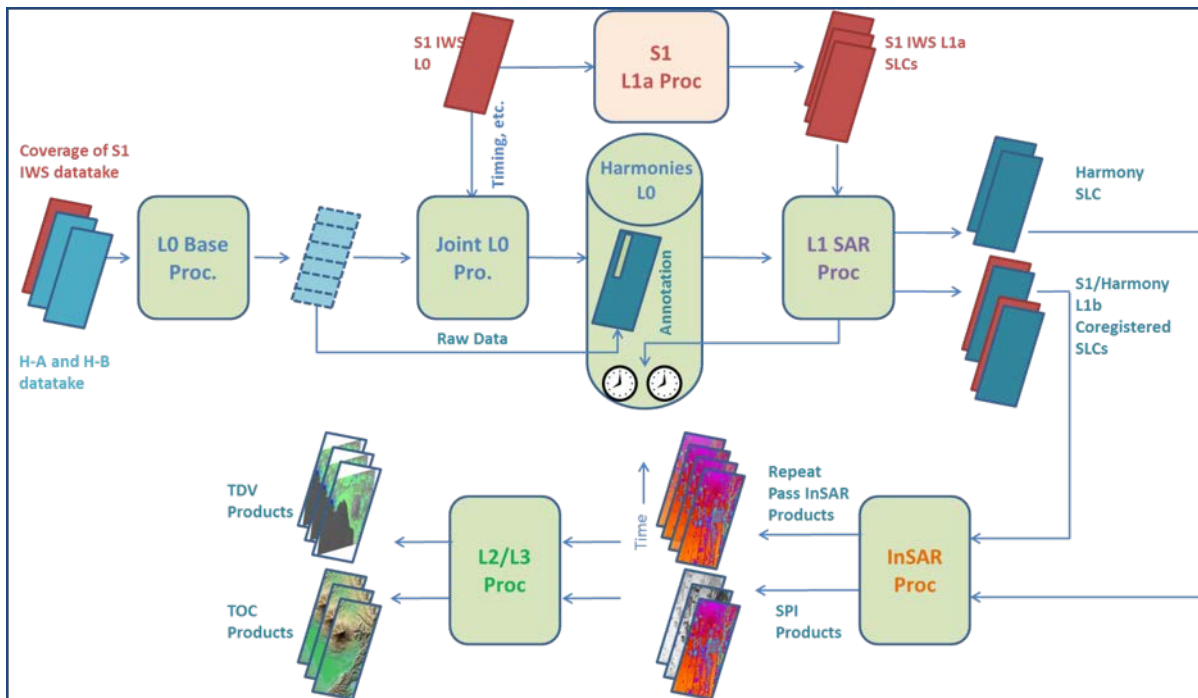


Figure 6.2: Data processing flow for land products. (Concept A)

6.2 Data product validation

For Harmony's ocean products, the validation approach could partly rely on the global array of surface drifters, moored buoys, oceanographic research cruises and coastal HF radars. Standard validation approaches used in the EUMETSAT Ocean and Sea Ice (OSI) SAF and Copernicus Marine Environment Monitoring Service (CMEMS), such as triple collocation and spectral analyses, may be used, in combination with scatterometer U10S products, such as from [HY-2B](#). In addition, satellite products from few available near-cotemporal passes from e.g. Sentinel-3 VNIR/TIR and high-resolution Sentinel-2 VNIR may allow under favorable illumination and cloud cover conditions to identify and to some extent quantify small-scale ocean processes of interest, thus aiding the scientific validation of Harmony products. Dedicated Harmony campaigns (e.g. WaddenSAR – experimental flights planned to be conducted within 2020) can mimic Harmony's observational concept together with necessary in-situ characterisation. In addition, large international campaigns (e.g. the recently conducted EUREC4A-OA campaign) with a clear focus on air-sea interaction mechanisms could further pave the way Harmony's product validation.

For Harmony's TOC (land) products, stereo-photogrammetry from space – in absence of cloud cover and with sufficient illumination conditions – would be able to provide an additional reference. Insufficient optical contrast due to snow cover and particularly rough to-

pography may limit its use for glaciers, but nevertheless there will be opportunities for cross-validation. In addition, scientific and operational airborne stereo-photogrammetric or laser-scanning repeat DEMs, from science projects or national mapping agencies, from manned aircraft or UAVs, could also play a role in the validation of Harmony's TOC products. As explained in Table 7.1, radar and laser altimeters can provide accurate TOC over the main parts of the ice-sheets and large glaciers, and could provide validation at selected points and assist in resolving the penetration bias for different land ice conditions at C-band. Also space or airborne photogrammetry and laserscanning can assist in resolving such bias. For TDV products, Harmony will be able to take advantage of existing GNSS station network that will be able to provide point reference measurements that can be directly related to the Harmony products.

6.3 Data user communities

Harmony is expected to provide a needed contribution in coupled ocean-atmosphere models, where its datasets can be used to describe and parameterise small-scale physical processes that are currently not well represented within these model environments. The enhanced ocean forcing, SST and motion measurements will be taken up by the CMEMS for more sophisticated products with specific requirements in coastal regions and for extremes. Met offices and hurricane forecasting centers will be interested to use Harmony observations to down-scale scatterometer winds, in particular in combination with SST data, and to better understand and correct for biases associated to unresolved variability. An important aspect to stress is that C-band measurements for maritime and ocean applications, including analyses during extreme conditions, have a long-standing history and heritage – starting from ERS-1 for both SAR and scatterometry in both operational and research contexts. Therefore, the added directionality and polarisation diversity at high-resolution provided by Harmony will consolidate and further attract existing user communities to make efforts for inclusion of the data within their existing frameworks, retrieval chains and processing environments.

For Harmony's land applications, it is clear that Harmony products will directly benefit the existing and mature InSAR geodesy user community, which has been requesting the Agency for many years to find a solution to address the large insensitivity to north-south displacements using classical monostatic InSAR techniques. The Harmony products related to glacier elevation changes and ice dynamics will serve a wide range of user communities, with many of them already used to work with this type of data, including research and applications within climate and climate impact modelling, sea-level change, water resources and hydropower, ecosystems, and cryospheric hazards to settlements and infrastructure.

7 SYNERGIES AND INTERNATIONAL CONTEXT

This section discusses the synergies to other existing, planned or, in some cases, proposed missions. The following sub-sections discuss the main synergies per domain, while Table 7.1 provides a broader overview.

7.1 Oceans and air-sea interactions: quantify and calibrate multi-scale processes

Improved predictions of weather, sea level, sea ice, ecosystem functioning, and many other components of the Earth system are increasingly critical for predictions across time and spatial boundaries. For the ocean-atmosphere system, no computer can encompass the interacting dynamics of all scales involved in upper ocean circulation – ranging from the scale of the Sun’s heating (~10,000 km) down to the turbulence dissipation scale (~1 mm). Computers can only simulate some of the scales. The unresolved scales of motion, must be observed, measured, and then parameterised for each type of rapidly fluctuating phenomenon (wave, eddy, current, clouds), in terms of its effects on the resolved scales. Parameterisation means that many of small-scale processes are represented by approximate laws (e.g. eddy-diffusivity), derived and calibrated from observations, also possibly limited in terms of capability/representativeness.

In concert with model developments, satellite remote sensing observations are thus essential components to help constrain initial boundary conditions or reveal the synthesis of all of these mostly unknown forces and non-linear interactions. Complemented with in-situ observing networks, goals have been first to ensure the precise monitoring of selected key sets of geophysical variables (e.g. sea surface height, temperature, salinity, colour, winds, waves), and/or advancing fundamental knowledge through development of empirical evidences and theoretical models (e.g. exchanges of momentum, heat and gas).

Key products now include merged global ocean surface topography using the different available altimeter missions, global and daily high-resolution sea surface temperature and ocean colour using multi-sensor and platform measurements, extending today to sea surface salinity products. Mapping high sea surface winds from combined radiometer and scatterometer observations can be performed, and more recently includes radar instruments for the fusion of sea state data (altimeters, SAR and RAR measurements). In parallel, simulation capabilities and numerical resolution have largely improved.

Still, these high quality data are too sparse or not sufficiently resolved. Moreover, strengths and weaknesses of the different observing methods are not always fully characterised under all environmental conditions, leaving questions about the use of the observations for predicting the intensity, the frequency and the tendency of particular events, especially extremes. Finally, although very short spatial scales largely contribute to horizontal and vertical fluxes of momentum, heat and tracers, most satellite observations do not resolve fine scale structures.

Accordingly, an area of unfulfilled promise is to improve the development of combined inversion via the ever-increasing complement of (passive/active) microwave and optical techniques. Intrinsic individual sensor limitations can be minimised using data synergies. For satellite oceanography, strategies are directed to address the so-called *altimetry-gap* and *scatterometry-gap*. Efforts are motivating technology solutions, a.k.a to develop new alti-

Table 7.1: Harmony in relation to other missions and observation concepts.

Missions	Harmony-related capabilities	Complementarity
Radar Altimeters (RA) and Laser Altimeters (LA)		
<p>RAs: Jason-2, Jason-3, Cryosat-2, HY-2, Sentinel-3</p> <p>LAs: ICESat-2</p>	<p>Radar-altimeter currents relate to the geostrophic equilibrium, i.e. mostly mesoscale currents with spatial scales O(50 km) or larger, with a global coverage.</p> <p>RAs and provide accurate TOC over the main parts of ice-sheets, but have large uncertainties over steep-terrain, leading to major coverage gaps.</p>	<p>Harmony will resolve much smaller scales (O(5 km) or less), to include components that are not in geostrophic balance, to study submesoscale processes as well as mesoscale eddies at high latitudes. Harmony will fill the TOC observational gaps in the often dynamic areas with steep terrain, and densify altimeter measurements elsewhere. Altimeters will be used as a reference for Cal/Val of Harmony's TOC products.</p>
Wide Swath Ocean Altimeters (WSOAs)		
SWOT	<p>WSOAs will extend the scales covered by traditional altimeters down to O(15 km), resolving the smaller SSH mesoscales and larger submesoscale features, not necessarily in quasi-geostrophy balance</p>	<p>Aside from reaching smaller scales, the combination of WSOA and Harmony observations will allow the decomposition of measured SCV between geostrophic and other dynamic components.</p>
Radar scatterometers		
<p>METOP-SG, HY-2, FY-3, Oceansat, Scatsat, CFOSAT, GCOM-W3</p>	<p>A growing number of wind-scatterometers provide operational stress-equivalent winds globally, several times per day, at resolution down to O(15 km).</p>	<p>Harmony measurements will be used to implement data-driven methods to down-scale scatterometer winds, to better understand and correct for biases associated to unresolved variability, in particular in combination with SST data, and SCV estimates. C-band scatterometers, on the other hand, will provide an extremely well-calibrated reference against which Harmony can be cross-calibrated.</p>
Doppler Radar scatterometers		
<p>SKIM (proposed, Arduin et al. (2019), WaCM (proposed Rodríguez et al. (2019)</p>	<p>Newly proposed Doppler scatterometer concept add SCV retrieval capabilities to traditional scatterometers, but focusing on (global) coverage than on high resolution.</p>	<p>By concentrating on different spatial scales, Harmony and the proposed medium resolution Doppler scatterometers concepts would be highly complementary, with the second providing the larger mesoscale and regional context, and Harmony resolving the small-scale processes.</p>

Synthetic Aperture Radars		
Sentinel-1 mission, Radarsat Constellation, NISAR, ALOS-(3,4), ROSE-L, Biomass	<p>Harmony extends Sentinel-1 by providing the needed directional capability to the measurements. The combination of Harmony with other SAR missions, most notably the other concurrently flying Copernicus SAR missions, will directly improve the combined ability to resolve processes in time. By building a dictionary of information-rich observations (or analogues) Harmony will provide a solid interpretation framework for the features observed by non-directional monostatic systems, also after the Harmony mission lifetime.</p> <p>The inversion of physical parameters based on DEM changes will also benefit from height measurements retrieved at different wavelengths, as it will the case with Biomass.</p> <p>Current polar-orbit SAR missions provide measurements of deformations projected on a latitude dependent position dependent oblique plane. Harmony will provide the additional line-of-sight needed to retrieve 3-D velocities.</p>	
Visual and Near Infrared (VNIR) & TIR missions		
Sentinel-2 and 3	<p>Under favorable illumination and cloud-cover conditions, high resolution VNIR/TIR can address, identify and to some extent quantify many of the small scale ocean processes of interest to Harmony. Ocean waves can be detected and their phase velocity estimated, which also allows an estimation of surface current gradients.</p>	<p>Harmony will benefit from high resolution VNIR observations as they provide, on a case study basis, and independent view of the same processes, aiding the scientific validation of Harmony products. High quality TIR systems will provide a calibration reference for Harmony's TIR payload.</p>
Stereophotogrammetry missions		
CO3D, Pleiades, Pleiades follow-on	<p>Stereophotogrammetric high-resolution optical missions provide high-resolution Digital Surface Model (DSM) but are typically obtained by the combination of image-pairs acquired over long periods of time and hampered by cloud cover.</p>	<p>Stereophotogrammetric DSMs will be used as a reference, for example for phase-unwrapping, and, on selected glaciers, as an ad-hoc Cal/Val reference.</p>

meters with multi-beam illumination patterns and/or interferometric capabilities, e.g. the SWOT instrument (Morrow et al., 2019), and the present solutions to augment the radar line of sight diversity, with the Harmony combined payloads. Also note, within the European Copernicus programme ensuring a long-term perspective, a new Copernicus Imaging Microwave Radiometer (CIMR, Kilic et al. (2018)) having improved resolution capability has now been accepted for implementation.

Building on high-quality highly-resolved observations (e.g. SWOT, Harmony), the development of new tools, geometric, spatial and temporal characteristics will be more systematically extracted, confronted to numerical simulations, and efficiently mined using objective data-driven and/or dynamically-driven methods.

Specifically, Harmony will provide multi-scale reference measurements to largely contribute

to fill in these observation gaps, altimetry, scatterometry, including anticipated future Doppler scatterometry (Rodríguez et al., 2019; Wineteer et al., 2020; Hoogeboom et al., 2018)) and passive radiometry (e.g. CIMR). Harmony azimuthal observation capabilities will directly extend the knowledge of the 2D co-spectra of surface stress, surface wind, surface currents, and SST, from the scatterometer and radiometer scale $O(25\text{km})$ down to $O(1\text{km})$ scales, covering all relevant conditions at the sea surface and in the MABL. Moreover, from the Harmony design point of view, Sentinel-1 is not only an illuminator, but a fundamental part of the system, providing one of the required line-of-sights. Accordingly, Harmony will directly enhance S1 products, but also will serve to enforce the interpretation of data acquired from the other S1 satellite(s) in its constellation. More particularly, Harmony shall trigger the development of innovative strategies or approaches for massive ocean S1 Wave Mode image analysis, to more quantitatively inform existing catalogues of environmental conditions (Wang et al., 2018, 2019). These efforts are anticipated to comfort improved directional surface wave analysis, with Harmony measurements improving upon the standard S1 products, in line with dedicated wave scatterometer instruments (i.e. SWIM/SKIM-like instrument, Arduin et al. (2019)).

From the ability to both study and fully quantify individual snapshots in detail and to composite results from many acquisitions, Harmony will extend the knowledge of the total ocean surface motion power spectrum, from currently resolved available mesoscales $O(50\text{km})$, and in near future 30 km down to submesoscales ($O(1-20\text{km})$), also capturing the regional variability and the seasonal cycle. Robust correlations with relevant controlling factors will be extracted, and these statistical properties will contribute to quantify the impact of unresolved scales, especially for wide-swath medium-resolution Doppler scatterometer instruments. Harmony directional measurements will also help more direct usage of uni-directional estimates from the other S1 satellite(s) in its constellation, including global S1 Wave Mode analysis (Moiseev et al., 2020).

7.2 Cryosphere

The Harmony surface elevation products will cover the complete global ensemble of glaciers, ice caps and outlet glaciers of ice sheets with the main objective to measure the surface elevation change in discrete, pre-determined time intervals at high spatial resolution in order to estimate the mass balance and to support studies on glacier dynamics. Satellite-based estimations of glacier and ice sheet mass balance are using 3 different approaches that are highly complementary and cover different spatial and temporal domains:

1. The geodetic method, based on measurements of surface elevation change (SEC) by means of altimeters or imaging sensors operating in the optical or microwave spectral region, using estimates of the density of snow and ice lost to convert the measured volume changes to changes in mass.
2. Satellite gravimetry, estimating changes in land ice mass by integrating measurements of gravity fluctuations occurring within a glacier or ice sheet region that is typically of the order of 10^4 to 10^5 km^2 in extent.
3. The input output method (IOM). The focus of the IOM is on calving glaciers and ice streams, quantifying the difference between estimates of the net surface mass balance (SMB) and the discharge of ice into the ocean or into lakes. A range of different optical

and SAR satellite images is used for deriving flow velocities and computing ice sheet discharge (output). Numerical models, driven by meteorological data, are used for estimating the net SMB.

The geodetic method is highly complementary to gravimetry and IOM, in particular if based on imaging sensors, as it delivers spatially detailed information on SEC and mass accumulation/ depletion. The complementarity and added value of the 3 methods has been proven in the Ice Sheet Mass Balance Intercomparison Experiment (IMBIE), delivering benchmark values of the Antarctic and Greenland Mass Balance for the IPCC (Shepherd et al., 2018, 2020). The geodetic mass balance estimates for the ice sheets are mainly based on altimetry. Spatially detailed data on SEC are available for a subset of the outlet glaciers. Whereas the main parts of ice sheets are well covered with geodetic repeat observations thanks to altimetry, there are still large gaps in the observations of mountain glaciers impeding efforts to quantify climate-induced trends and to calibrate and evaluate diagnostic and predictive mass balance and ice dynamic models. Satellite altimetry suffers from high uncertainty and large gaps in steep terrain. Gravimetry delivers bulk mass balance estimates for extended glacier regions, but high resolution data are needed to provide spatially detailed data as required for model input and validation and for consolidating the mass balance numbers. For some regions, e.g. Himalaya, gravimetry is complicated as the signal from glacier mass changes mixes with signals from large ground water changes and filling of inland lakes in the same regions. Table 7.1 provides an overview on current and planned satellite missions that are complementary to Harmony for measuring surface topography and topographic change.

7.3 Solid Earth

The line-of-sight diversity provided by Harmony will be a unique feature in the frame of space-borne interferometric SAR missions. The near-polar orbit of current SAR satellites results in a poor sensitivity to deformation in the north-south direction. Harmony will fill this gap by allowing, for the first time, millimeter-accuracy 3-D measurements of surface deformation from space by exploiting repeated interferometric acquisitions over the same area. The images acquired by the Harmony satellites will be combined with those acquired by Sentinel-1 under different ascending and descending geometries to allow for an accurate 3-D deformation retrieval. In addition, line-of-sight measurements of other SAR missions can be exploited together with the Harmony measurements to provide additional robustness and accuracy. A clear example of a potential synergy is given by the future European ROSE-L satellites, which will be operated by the Agency and provide high-resolution and wide-swath coverage following the same orbit as Sentinel-1. A further example is the NASA-ISRO SAR mission (NISAR) (Rosen et al., 2014), to be launched in 2022, which will provide measurements at L- and S-band with a wide swath (240 km), and will perform acquisitions in a left-looking geometry for better polar coverage. This can be also exploited to gain some sensitivity to the north-south deformation, but will still be far less accurate than what can be achieved with the Harmony geometry (Ansari et al., 2016; Prats-Iraola et al., 2018). Similar synergies can be achieved with other SAR missions like the Japanese L-band ALOS-2 (Okada et al., 2013), the Argentinian L-band SAOCOM, as well as the Italian X-band COSMO-SkyMed second generation (CSG), which in its ScanSAR mode will achieve a similar resolution and swath coverage as Sentinel-1. Needless to say, the line-of-sight diversity provided by Harmony will play a key role in the design of future multi-satellite SAR missions for the monitoring of deformation phenomena.

A MISSION PERFORMANCE

This annex provides a brief overview of the retrieval approaches, expected performances, and also of the tools or methods developed to estimate these performances. The annex is organized by family of products that share a common approach. For example, although the challenges associated to TOC retrieval on glaciers or on volcanoes can be significantly different, their retrieval share a common basic principle and most of the data processing steps.

For several products SSV, SWV, and SCV and cloud-top parameters a significant effort has been put in developing simplified end-to-end simulators. For the ocean products the reason is that it was important to verify that Harmony is capable of retrieving the fine-scale spatial structure of the variables of interest. For TDV and TOC over land an end-to-end was also deemed important in order to adequately assess the impact of atmospheric and system related spatially correlated errors in the final products. For TOC over ice-covered areas, the emphasis during Phase-0 was in correctly modeling uncertainties and, in particular, biases at resolution-cell level.

A.1 Oceans surface products

This section addresses mainly the radar derived ocean and air-sea interaction related surface products: SSV, SWV, and SCV.

Due to space constraints, we limit the discussion of the retrieval and the performance of SST products to the main findings, which are analyzed in detail in a dedicated technical report (Ciani et al., 2020). While high quality SST fields can be obtained by other sensors, the driver for having simultaneous TIR measurements of the ocean surface is to derive co-located SST gradients. The gradients of interest correspond to sharp features, with correlation lengths much shorter than the typical correlation length of atmospheric features. Therefore, while the use of split-band techniques is necessary for the retrieval of SST, this correction contributes little to the estimation of its gradients. In fact, since the correction implies the combination of two bands, errors due to noise are increased. Analysis using SLSTR TIR data show that the SST gradients can, therefore, be very well estimated using the panchromatic (PAN) TIR channel, which has better NE Δ T (< 0.1 K) and much better resolution than the 11 μ m and 12 μ m channels. In the case-studies analyzed, using the PAN channel allows the retrieval of the main SST features observed.

A.1.1 Retrieval Approach

Figure A.1 provides an overview of the processing flow envisioned to go from L1 products (radar SLCs, TAR data) to the main ocean and air-sea interaction products. Starting from the SLC data, the first steps would be to estimate the L1b multistatic and multi-polarized NRCS, the intensity cross spectra and higher level spectral parameters such as the azimuth cut-off or the MeAn Cross-Spectra (MACS) (Engen and Johnsen, 1995; Kerbaol et al., 1998; Collard et al., 2005; Li et al., 2019), and the geophysical Doppler centroids (USV).

Starting with these three sets of L1b product the processing can be divided in three interconnected branches. The central branch (in blue) will estimate swell and wind-wave spectra, extending the current SAR ocean wave inversion algorithms to the multistatic case.

On the left branch (in purple) the multi-directional NRCS will be used, following wind scatterometry principles (e.g. Stoffelen and Portabella (2006)) and extending on SAR-based wind

retrieval approaches (Horstmann et al., 2003; Horstmann and Koch, 2005; Mouche et al., 2012), to estimate the stress-equivalent surface wind vector (SSV). Note that this 1 km or better resolution surface stress is one of the key outputs of the mission. To convert SSV to SWV, first the motion of the ocean surface (SCV) needs to be added, and then the surface stress equivalent wind needs to be translated to a wind at a reference height (SWV) accounting for the state of the MABL (Smith, 1988). A characterization of MABL (by itself one of the goals of Harmony) will be done extending current approaches applied to monostatic SAR data (e.g. Young et al. (2000)) and including SST data (both Harmony measurements and data from other sensors) and, in cloud-topped marine boundary layers, the TIR retrieved cloud-top motion and cloud-top height.

In the right branch of the flow-chart (in red), the first step shown is the estimation of the so-called wave-Doppler, which results from the correlation between the wave-slope modulated NRCS and the wave-induced motion of the surface. The wave-Doppler, converted to velocity, amounts to 10 % to 20 % of the wind velocity (Chapron et al., 2005). The wave-Doppler is narrowly linked to the wind-wave spectrum. Therefore, it can be estimated using a theoretical or empirical Geophysical Model Function mapping wind directly to Doppler, derived from the estimated wave-spectrum, or estimated exploiting its dependence on polarization. A combination of all these methods is expected to give the best results.

The wave-Doppler corrected Doppler centroids can be projected to the surface, giving an estimate of the SCV. For mesoscale and submesoscale ocean processes the emphasis of the mission is on relative motions, which implies that remaining measurement of inversion biases (e.g. wave-Doppler compensation) can be accepted.

Although SCV gradients (and from there, for example, the vorticity or the divergence) can be calculated from the estimated SCV, higher resolutions can be obtained exploiting the signature of these gradients in the NRCS (Kudryavtsev et al., 2005, 2012a; Rascle et al., 2017).

A.1.2 Performance Estimation

This section discusses the expected performance for the radar-derived surface-stress and surface wind vector products, and for the (relative) total surface current product. The expected performances have been evaluated following two approaches:

1. a semi-analytic end-to-end performance estimator that computes the error-covariance matrices of the Least Mean Squares (LMS) estimator of the surface stress surface current vectors;
2. a L2 product-level simplified end-to-end simulator, where the L1b products are explicitly simulated and fed to a retrieval module.

In order to illustrate the analytical performance computations, Figure A.2 shows the uncertainty of the retrieved equivalent wind at 1 km² product resolution and an incidence angle of 35° as a function of the true equivalent wind vector. The uncertainties have been decomposed in the down-stream component (left) and the cross-stream component (right), and normalized by the true value. There are some narrow directional bands with, in relative terms, degraded performance, which is due to the limited azimuth diversity. The performance is dependent on the position in the swath, with worse performances near the edges of the sub-swathes due to the degraded system sensitivity and at very large incidence angles due

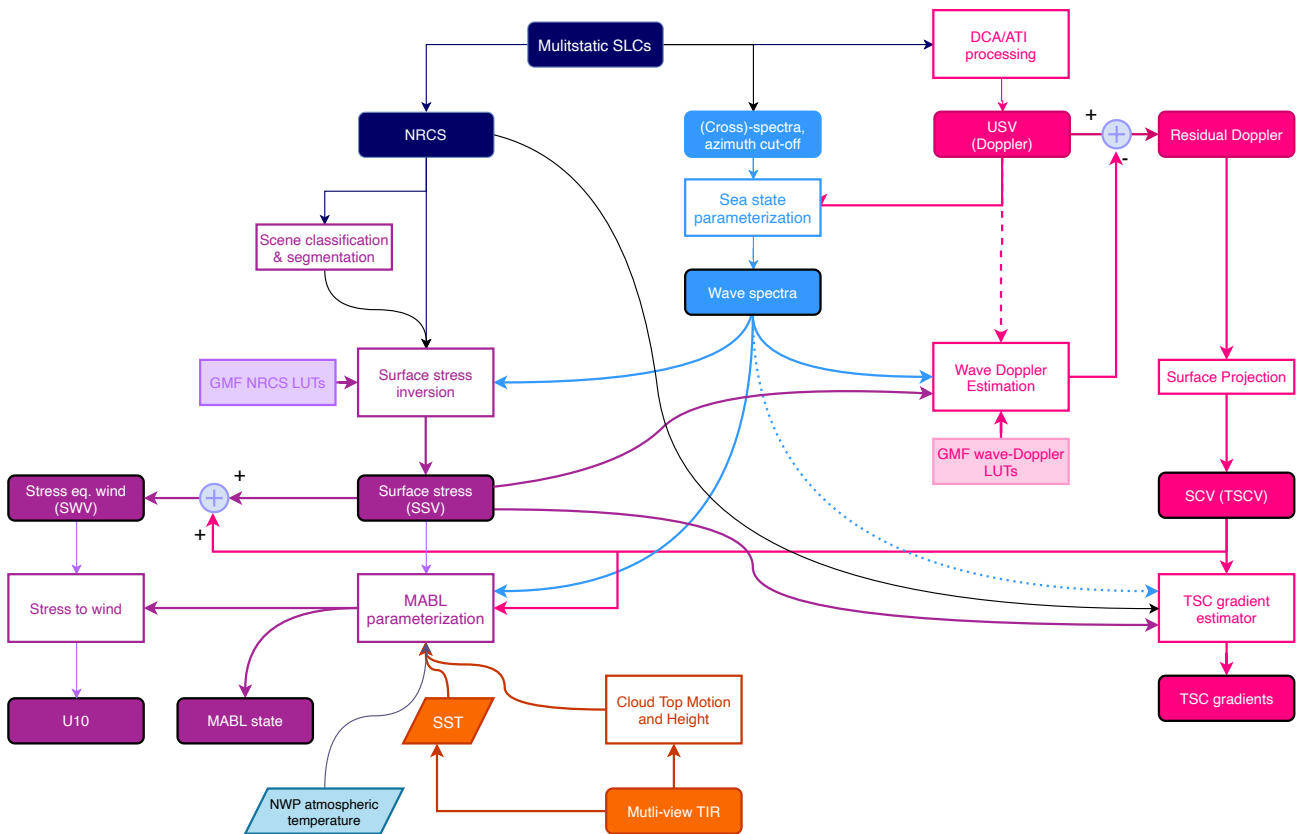


Figure A.1: Schematic flow-chart of the retrieval approach for oceans and air-sea interaction products.

to the rapid decrease of the Normalised Radar Cross-Section (NRCS). Nevertheless, across the swath and range of winds of interest, the errors are well below 7.5 %.

Figure A.3 shows the SCV retrieval errors as a function of the wind vector, resulting from combining Doppler velocity measurement uncertainties and the mapping of the stress-equivalent wind retrieval uncertainty in a wave-Doppler correction error. The cross-track SCV uncertainty remains below 3 cm s^{-1} to 4 cm s^{-1} . Due to the somewhat limited line-of-sight diversity, the along-track SCV uncertainty is significantly larger, but remains typically well below 10 cm s^{-1} . Systematic errors associated, for example, to spacecraft orientation errors or retrieval biases are not considered. This is justified as the requirements specify relative SCV uncertainties.

Figure A.4 shows a block diagram of the simplified end-to-end simulator, with several components used also for the semi-analytical performance tools. The simulator includes the following components:

- The **geometry module**, which determines the observation geometry as function of the position in the swath, the formation configuration, and the position along the orbit.
- The **forward model**, which provides the multi-static and polarization dependent NRCS and wave-Doppler as a function of the observation geometry and the input stress-equivalent surface wind and wave-age. The NRCS and wave-Dopplers are pre-computed and stored

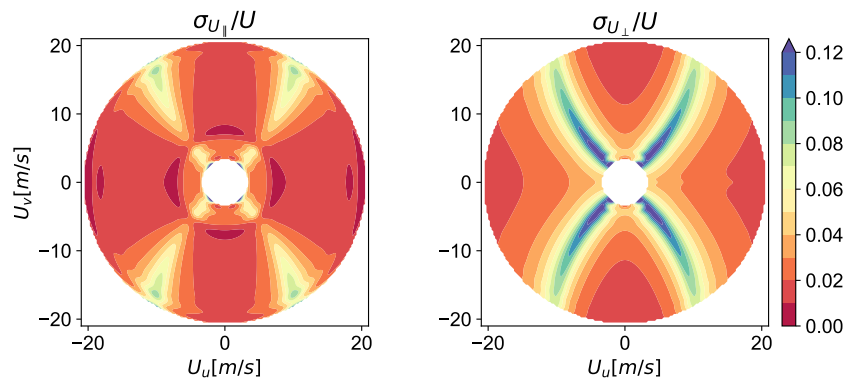


Figure A.2: Normalized surface-stress equivalent wind estimation errors as a function of the true wind vector for a 1 km² resolution product at 35° angle of incidence. The left and right panel show, respectively, the down-stream and cross-stream 1 σ uncertainties normalized by the true surface stress equivalent wind.

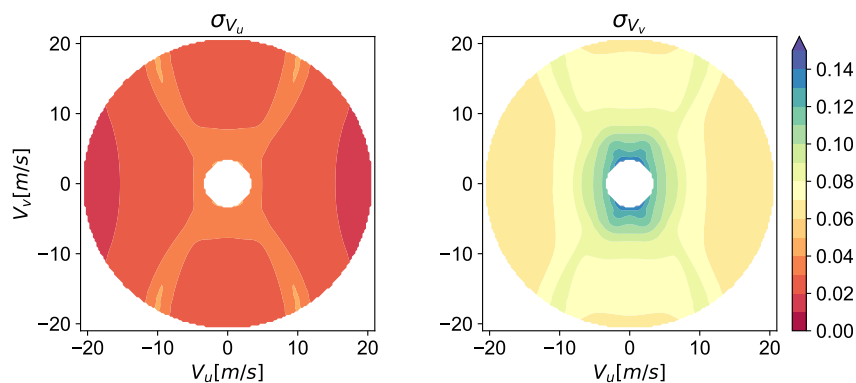


Figure A.3: SCV uncertainty (1 σ) as a function of the surface-stress equivalent wind vector at 2 km \times 2 km resolution and 35° incidence angle. Left: cross-track component. Right: along-track component.

in look-up tables for several electromagnetic scattering models.

- A **scene generation** module that, using the forward model, maps the input surface stress equivalent wind vector and surface current vector fields into the expected value of the L1b products (NRCS, Geophysical Doppler), taking into consideration the multi-static observation geometry, and adding some degree of *geophysical noise*;
- a **Radar module**, which uses the instrument performance computed from a parameterised instrument description to add the measurement noise.
- A **retrieval** module, which implements a simplified retrieval algorithm to estimate the stress equivalent wind and the SCV.

All components are openly available as open-source packages.

To illustrate the E2E chain and the the potential of Harmony we have simulated an ascending-

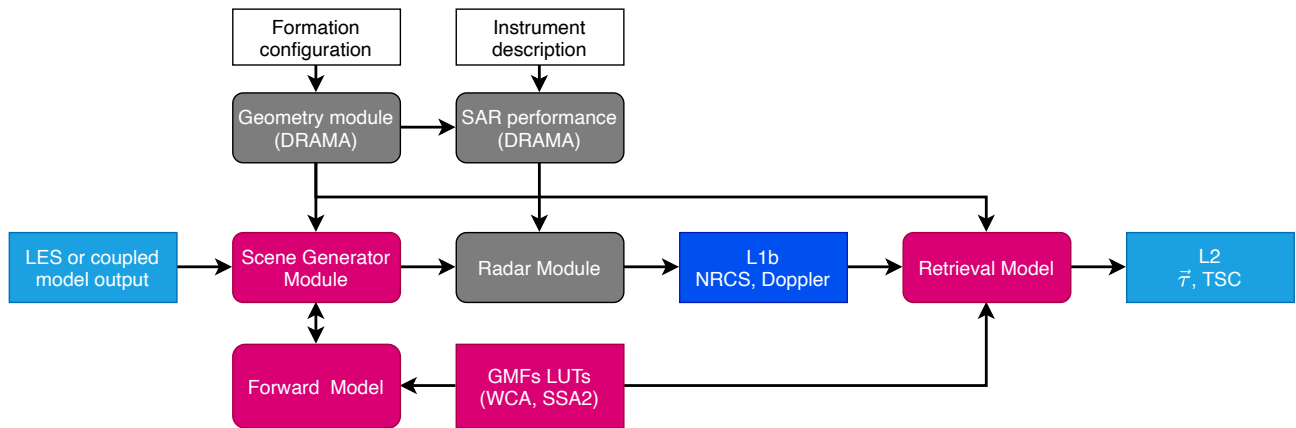


Figure A.4: Simplified product-level end-to-end simulator for ocean radar products

orbit acquisition of the coast of California, approximately matching the geometry of one of the Sentinel-1 tracks for which data is currently being acquired.

Figure A.5 shows the simulated NRCS at 1 km² resolution. The coupled model directly provides surface stress vectors, which are used as an input to the forward model. A stream plot of the surface-stress equivalent wind, \mathbf{U}_{eq} , is shown in the left panel of Figure A.6. Aside from the common modulation of the NRCS by the wind speed, which, for example, leads to low NRCS levels at the upper part of the image, the varying wind direction can be recognized in the changes of the NRCS differences between for the different observation geometries.

The center panel in Figure A.6 shows a stream plot of the estimated wind, $\hat{\mathbf{U}}_{eq}$, whereas the right panel shows the relative error,

$$\frac{|\delta \mathbf{U}_{eq}|}{\sqrt{2} |\mathbf{U}_{eq}|},$$

where the $\sqrt{2}$ term normalizes the error to make it representative of the vector components, and $\delta \mathbf{U}_{eq}$ is the vector-difference between the estimated stress equivalent wind and the input stress equivalent wind. The areas where the relative error exceeds 7.5 % are a result of the wind direction within those areas falling into the relative *blind spots* of the wind retrieval (see Figure A.2).

Finally, we want to illustrate the capability of Harmony to estimate SCV gradients, for example to retrieve the surface motion vorticity,

$$\omega = \nabla \times \mathbf{V} = \frac{\partial V_v}{\partial x} - \frac{\partial V_u}{\partial y}. \tag{1}$$

For the example, we estimate the gradients applying a Gaussian kernel with a circular resolution of approximately 5 km. The left panel in Figure A.7 shows the SCV vorticity computed from the model data at full resolution. The center panel shows the effect of applying the Gaussian gradient estimation kernel to the model data, with the obvious loss of detail and also loss of eddy-kinetic energy. The right panel shows the vorticity derived from the simulated data. In this case rather than using the estimated SCV, we use the ground-projected Doppler velocities, in other words, we do not attempt to remove the wave Doppler. In this

example, ignoring the wave-Doppler, would introduce biases in the surface motion vector in the order of 1 m s^{-1} , which is more than the actual surface current. However, the SCV Doppler gradients are much larger than the wave Doppler gradients, so the latter can be largely ignored in the retrieval of, for example, the vorticity.

For example, the standard deviation of the difference between the estimated Gaussian filtered true vorticity and the estimated vorticity without wave-Doppler correction is $4.8 \times 10^{-6} \text{ s}^{-1}$, an order of magnitude below the observed vorticities themselves.

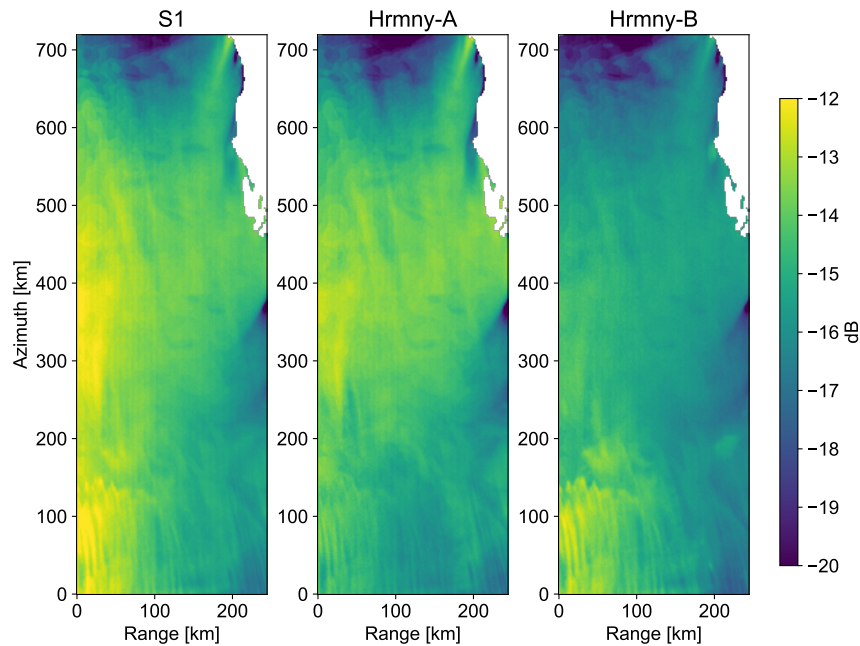


Figure A.5: Simulated NRCS measurements for Sentinel-1 and the two Harmony spacecraft.

A.2 Cloud-top motion and height

A.2.1 Retrieval Approach

Cloud Motion Vectors (CMV) Cloud Top Height (CTH)) will be retrieved from multi-angle Thermal IR (TIR) image views overlapping with the Sentinel-1 SAR-WV bistatic radar acquisitions using a combination of multi-image photogrammetry and computer vision. Such multi-angle retrievals have been previously demonstrated with time-delayed repeat multi-views for across-track cloud motion and along-track CTH using the ESA 2-view (A)ATSR(2) for visible, SWIR and TIR bands (Muller et al., 2007) as well as for the NASA 9-view red channels of the NASA MISR sensor (Moroney et al., 2002). The retrieval approach for the initial demonstration adopted here uses the M2 matcher (Muller et al., 2002) in a Jupyter notebook based on Python.

The difference here is that we will employ a simultaneous tandem acquisition of different views from the forward and aft satellite solely in the TIR to achieve consistent day and night coverage. Such a configuration has not been demonstrated in space previously with a polar-orbiting satellite. Previous satellites such as (A)ATSR(2) satellites have around 2 minutes between the subsatellite track nadir and forward pixel and MISR up to 7 minutes between

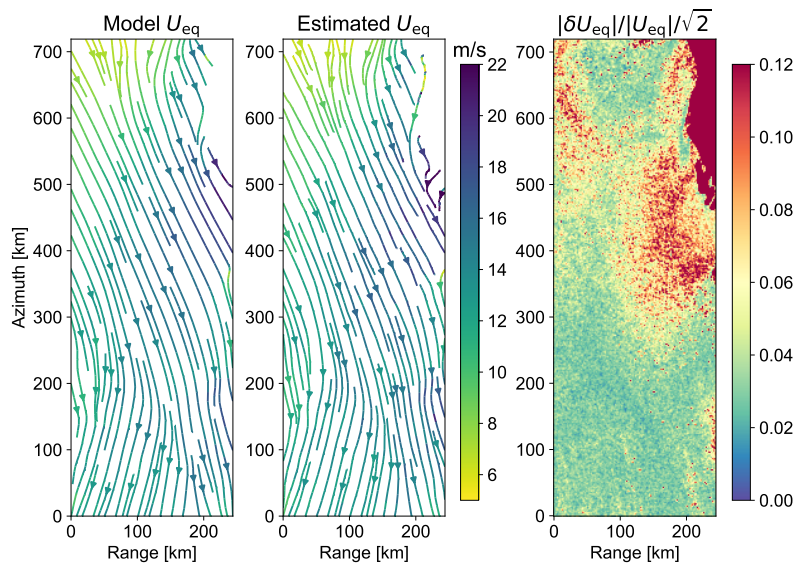


Figure A.6: Model input surface stress equivalent wind (left), simulated retrieved wind (center) and relative retrieval error.

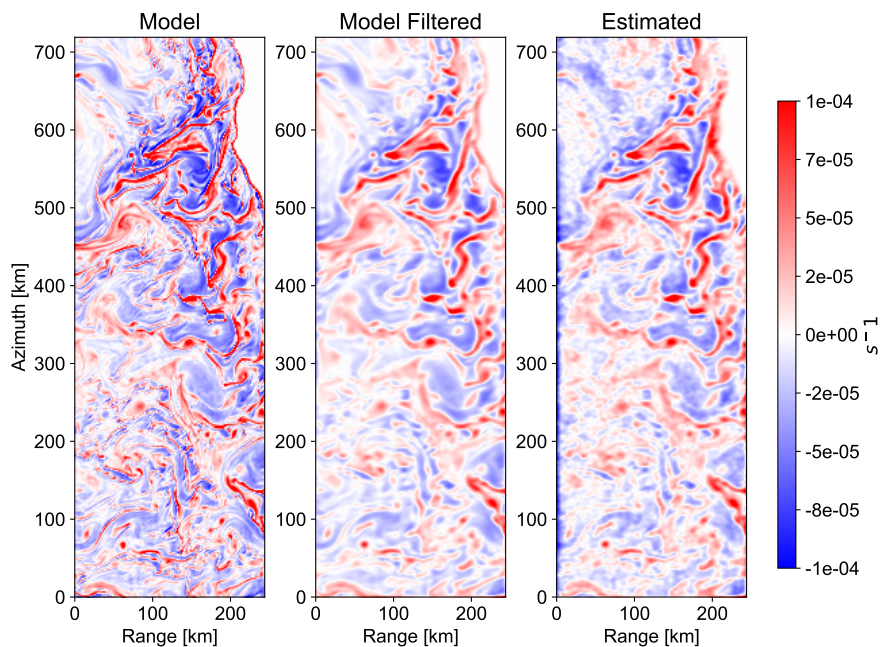


Figure A.7: Surface motion vorticity estimated using full resolution input model data (left panel), and applying a 5 km Gaussian gradient estimation kernel to the model data (center panel) and to the estimated surface motion without wave-Doppler cancellation.

the foremost 70° and aftmost -70° . This implies that for the former (A)ATSR(2) system one can only retrieve across-track winds with low precision whereas for MISR one has to employ extreme angles ($\pm 60^\circ$, $\pm 45^\circ$) to exploit the large time difference between the different looks to be able to unscramble cloud motion from the CTH (Horváth and Davies, 2001). Since clouds transform over 7 minutes, uncertainty in both CTH and CMV is best reduced by employing simultaneous views in a tandem satellite configuration. Full 3D radiative transfer simulations generated 4D cloud-fields are used for testing as described below.

A.2.2 Performance Estimation

In order to verify and evaluate the TIR mission concept, and to help the development of algorithms tuned to the particular configuration and geometry of Harmony, an advanced and realistic end-to-end simulator framework is required. The end-to-end framework proposed is based on the EarthCARE simulator framework (Voors et al., 2007), originally developed at KNMI to enable the development and evaluation of the EarthCARE level 2 algorithms. A central idea behind the simulator is to have clear separation between the atmospheric model fields, the radiative transfer simulations and the instrumental effects. This has facilitated the rapid adaptation of the simulation framework to the needs to Harmony. For each location in the 3D-atmosphere there is a description of a particle size distribution for the different clouds combined with scattering libraries ranging from the UV to the FAR-IR. Only after the radiative transfer calculations have been performed the instrument response functions are applied to calculate the satellite viewed signals. The models within ECSIM are organized in the following modules:

1. Scene creation models (3D atmospheric scene definition);
2. Orbit models (orbit and orientation of the platform as it overflies the scene)
3. Forward models (calculate the signal impinging on the telescope/antenna of the instrument(s) in question using a range of radiative transfer models from state-of-the-art 3D Monte Carlo codes to single column estimates (i.e. Disort), depending on the calculation needs and size of the domains;
4. Instrument models (calculate the instrument response to the signals calculated by the Forward models);
5. Retrieval models (invert the instrument signals to recover relevant geophysical information).

A realistic input atmospheric field is required for input. For the results discussed, DALES model outputs are ingested into the ECSIM scene creator. The Dutch Atmospheric Large-Eddy Simulation (DALES Heus et al. (2010)) is a large-eddy simulation code designed for studies of the physics of the atmospheric boundary layer, including convective and stable boundary layers as well as cloudy boundary layers. The Large Eddy Simulation (LES) model results were subsequently put through the ECSIM-Harmony simulator to yield a set of radiance and Brightness Temperature (Bt) fields as if viewed by an idealized Harmony TIR imaging system. The infrared imager information is calculated using the ECSIM 3D reverse-Monte Carlo forward and instrument module. Figure A.8 shows a flowchart of the simulator, starting with the LES model output and ending with the four TIR channels for each of the viewing angles.

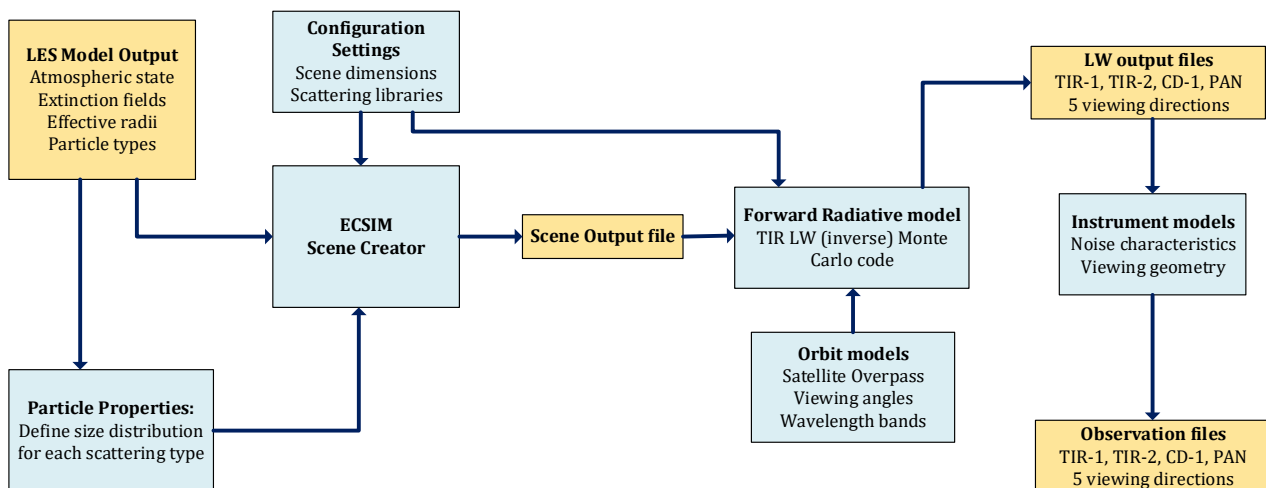


Figure A.8: EarthCARE simulator flow diagram. The blue boxes indicate modules, configuration files or scattering properties defining the ECSIM model calculations. The orange boxes indicate the data files starting with the LES model input fields and ending with the modelled signals for each of the channels for the five viewing directions.

Performance is difficult to estimate *ab initio* as stereo photogrammetric restitution relies on the image characteristics (e.g. contrast, SNR/dB) which cannot be pre-determined. In addition, we must specify a series of error terms concerning the imaging photogrammetric geometry, such as the so-called interior orientation (e.g. camera focal length location in the focal plane array known as the Principal Point (PP), the lens distortion as a function of distance away from this PP) and so-called exterior orientation elements such as the inter-camera distance, range to target and precision of the pointing vectors.

The image characteristics are driven primarily by the NEDT noise values and the degree of contrast in the scene. From experience, when the NEDT is as low as 0.2 K, images can still be employed for image matching although the accuracy can be significantly increased if TDI is employed, improving the NEDT by the square-root of the number of pixels/rows employed.

Two different DALES simulations have been used in this phase. In both simulations, the model output was sampled for a total of 7 minutes, with a time step of 1 minute, mimicking the case where a separation of 400 km between the individual satellites. The high-resolution information is converted to a Harmony-ECSIM scene after which the full 3D reverse-Monte Carlo infrared calculations are performed to simulate the TIR-1, TIR-2, CD-1 and PAN channels.

One of the scenes used simulates the atmospheric conditions found during the EUREC4A campaign, on February 6th, 2020. The model fields from DALES describe a low-level cumulus field with a relatively low cloud fraction. This represents a particularly challenging scenario for CMV retrieval, as many individual small clouds have lifetimes comparable with the lags between the different views acquired by the two satellites. The horizontal model grid resolution is 100 m with a 40 m vertical grid spacing. The model was run with an 8m/s rest frame velocity ($u_{10} = -8\text{m/s}$), which was compensated by adding a model grid horizontal shift

of 5 pixels per 60 second frame (-8.333m/s). ECSIM was run in a simplified flat-earth geometry and assuming a push-broom design. The resulting infrared images for the different angles are thereby collocated and the retrieval of cloud motion vectors is relatively straightforward.

The left panel in Figure A.9 shows a comparison of the vertical profile of cloud-top fraction, as output by DALES, and a histogram of the estimated cloud top-heights. While TIR retrieved cloud-top data cannot be expected to return a vertical profile, the figure shows that the MABL height (in this case around 2.1 km) can be well constrained using CTH estimates. The right panel in the figure shows a joint histogram of the retrieved CTHs and the main component of the CMVs, with the corresponding LES wind-velocity profile overlaid.

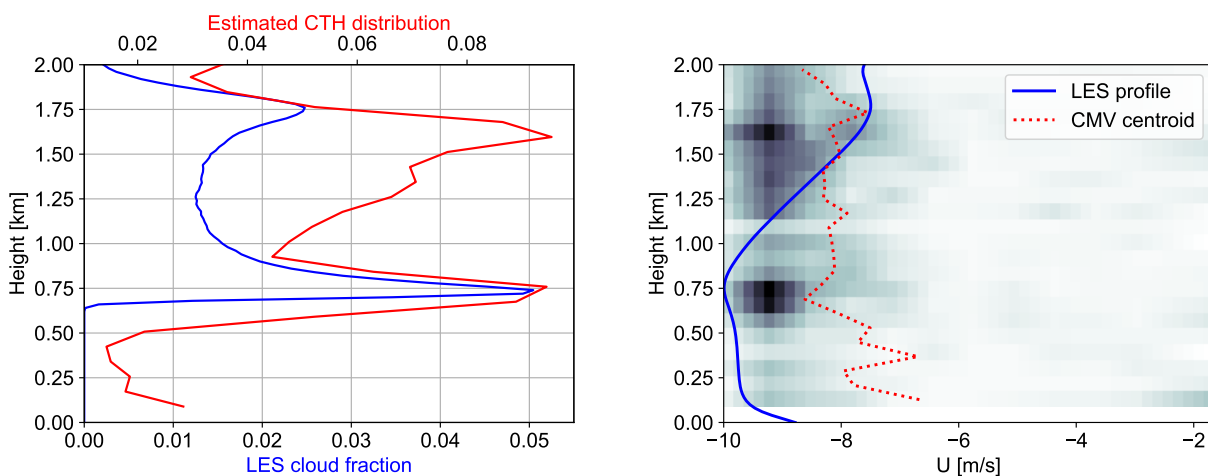


Figure A.9: Left: EUREC4A LES cloud-fraction vertical profile (blue line) compared to normalized histogram of retrieved cloud-top-height. Right: joint histogram of one component of the estimated cloud-top motion vector and corresponding cloud-top height. The blue line shows the LES wind-profile, while the red-dotted line shows the mean estimated velocity for each height bin.

A.3 Topography Change (TOC)

A.3.1 Retrieval Approach

TOC is estimated essentially by differencing sets of surface elevation models. The retrieval of DSMs using single-pass cross-track interferometry has been fully demonstrated by the Shuttle Radar Topography Mission (Farr et al., 2007) and the TanDEM-X mission (Krieger et al., 2007, 2013). DSMs generation will follow the same general approach as used in these missions.

The error of each DSM is comprised of a zero-mean noise-like component and by biases that may be due to the system (e.g. baseline errors) or of geophysical nature (e.g. penetration biases). The uncertainty due noise-like errors is discussed in Section A.3.2.

System-related errors will be highly spatially correlated, and can be mitigated using existing a priori DSMs. On the contrary, the elevation bias associated to penetration in snow or firn is a major point of attention. Whereas the C-band backscatter signal of wet snow and glacier ice is dominated by surface return, the apparent surface in dry snow and firn is shifted by several

metres. The magnitude of this bias depends on the scattering properties that are related to the snow microstructure. Because refrozen grains and grain clusters are efficient scattering sources, the phase centre in the percolation zone is closer to the surface than in the dry snow zone where the grain size is smaller. There are two complementary strategies to address these biases:

1. For inter-annual TOC, the main approach is to difference DSMs acquired under similar in-ice signal propagation conditions. If the polarimetric and interferometric signature of the SAR data is the same, it can be assumed that the offset of the scattering center versus the surface did not change. This requires repeat acquisitions in the same season. In case of stable conditions high accuracy can be achieved. This has been shown for glaciers on the Antarctic Peninsula where the comparison between TanDEM-X and NASA IceBridge airborne laser data shows over a 5-year period a mean bias of 0.08 m/yr and RMSD values for the data points on individual glaciers ranging from 0.14 m/yr to 0.35 m/yr (Rott et al., 2018).
2. Estimating the penetration from the multistatic multi-polarized and interferometric signatures. This can be done using empirical relations between these signatures and the InSAR elevation bias, which requires the use of training data sets (Abdullahi et al., 2019), or using analytical models. For example, for elevation biases that are small compared to the height of ambiguity, and assuming a simple exponential extinction model, the penetration bias is given by (Dall, 2007)

$$h_b = -\frac{H_{aVol}}{2\pi} \arctan \sqrt{\frac{1 - |\gamma_{Vol}|^2}{|\gamma_{Vol}|^2}}, \quad (2)$$

where H_{aVol} is the height ambiguity within the ice or firn, which accounts for the permittivity of the medium, and γ_{Vol} . This approach has been validated comparing TanDEM-X derived DSMs over Union Glacier in Antarctica with the Reference Elevation Model of Antarctica (REMA), obtaining a Root Mean Square Deviation (RMSD) of 0.74 m (Rott et al., 2020).

A.3.2 Performance Estimation

For a single DSM, the $1-\sigma$ uncertainty due to the noise-like term is typically expressed as

$$\sigma_h = \frac{H_a}{2\pi} \sigma_\phi, \quad (3)$$

with H_a the height of ambiguity, which is inversely proportional to the cross-track perpendicular baseline, and σ_ϕ the standard deviation of the interferometric phase error. The phase uncertainty is a function of the interferometric coherence and the number of independent samples (see, for example, Lee et al. (1994) for a derivation of the phase error statistics). There are many factors that contribute to a loss of interferometric coherence, but the dominant contributions in a single-pass setting are thermal and quantization noise, volume decorrelation and, to a lesser extent, decorrelation due to ambiguities. Volume decorrelation itself is a function of the vertical scattering profile (Hoen and Zebker, 2000) and the observation geometry: the volumetric coherence term, γ_{Vol} , decreases with increased penetration depth and with decreased height of ambiguity, as illustrated in the right panel of Figure A.10.

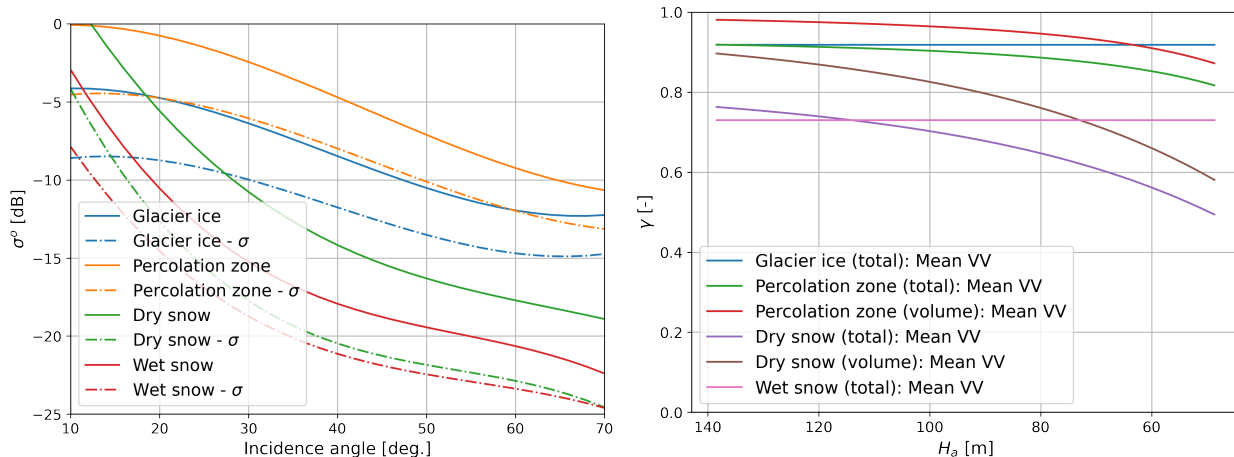


Figure A.10: Left: NRCS as a function of angle of incidence for various glacier facies. The solid lines represent the mean value, while the dashed lines represent the mean minus one standard deviation. Right: total (solid lines) and volumetric interferometric coherence (dashed lines) at C-band SAR as a function of H_a for different glacier facies, for an incident angle of 35° , assuming a SNR corresponding to the mean NRCS.

Therefore, while (3) suggests that the height error can be arbitrarily reduced by increasing the perpendicular baseline, when volume penetration plays a role the gain of geometric sensitivity is cancelled by the loss of coherence. The height of ambiguity is also lower-limited by the need to avoid phase unwrapping problems and spectral shift (Gatelli et al., 1994). Figure A.11 shows the expected uncertainty in the phase center heights for different surface types and as a function of the perpendicular baseline.

For the TOC product applied to Solid Earth, two different approaches have been implemented in order to evaluate the expected performance. The first approach is based on well-established formulae to derive the analytical performance (Krieger et al., 2007; DLR, 2020a), while the second approach is based on a simplified end-to-end simulator DLR (2020b). This is achieved by simulating SLC images at full resolution including the height and height change information for a desired number of pairs, as well as decorrelation and error sources. The simulator includes the processing and retrieval of the DEM, such that the difference between DEMs is evaluated and compared to the nominal performance based on the analytical models. The top row of Figure A.12(left) shows an example of topography change map (TOC) over Mt. Saint Helens. The TOC was obtained from real data by differencing DEMs acquired with 1 m-resolution lidar in October and April 2004, and shows topography changes ranging from around -13 m to 71 m. For the simulation, the TOC was subsampled to a 17 m posting grid and added to an upsampled SRTM DEM over the region. The resulting reference DEM is given as input to the TOC end-to-end simulator. For the results presented in this section, we assume a desired product resolution of 30 m x 30 m, a height of ambiguity of around 25 m and no vegetation. The backscatter is extracted from a Sentinel-1 image over the region, and no additional bistatic loss is considered, resulting in a mean SNR of around 11 dB over the region of interest. The plot in the middle of Figure A.12 shows the TOC map estimated by the end-to-end simulator, and the plot in the right shows the difference between input and estimated TOCs. An overall good agreement is achieved.

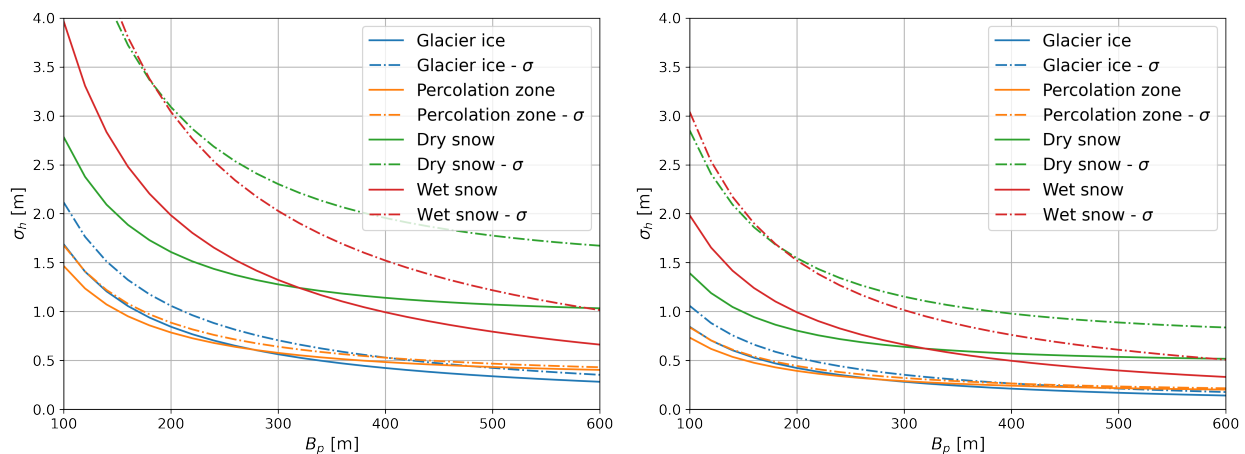


Figure A.11: Standard deviation of the interferometric height due to random phase errors as a function of the perpendicular baseline for a product size $100 \text{ m} \times 100 \text{ m}$, angle of incidence of 40° . The solid lines correspond to the mean σ_0 while the dashed lines correspond to mean σ_0 minus 1 standard deviation (broken lines). Left: Based on single acquisition. Right: Combination of 4 acquisitions.

The bottom row of Figure A.12 shows performance plots related to the whole processed area of around $3 \times 10 \text{ km}$. The plots correspond to the modeled performance, the performance obtained by directly comparing true and estimated TOC maps, and the 2D histogram relating modeled and estimated performances, respectively. The histogram shows that the predicted performance and the one obtained with the data agree. Over the valid TOC area, a predicted standard deviation of around 0.87 m and estimated standard deviation of around 0.93 m were obtained, hence fulfilling the requirement of 1 m (1σ). These results are also in line with the performance analysis shown in Section 5.4.3. If bistatic losses are expected or if larger heights of ambiguity are desired, a few DEMs before and after the event can be averaged prior to the DEM differencing. For example, similar performances are obtained averaging 2 DEMs (before and after) obtained with HoAs of around 40 m , or averaging 3 DEMs (before and after) obtained with HoAs of around 50 m . A smaller height of ambiguity, e.g., 15 m could be used in order to be more robust in relation to the unknown bistatic loss component, provided that abrupt changes are limited to 7 m per resolution cell. In this case, it is advisable to use DEMs computed prior to the event with a larger HoA to help with the phase unwrapping procedure.

A.4 3D Velocity vectors (TDV)

A.4.1 Retrieval Approach

For TDV, the retrieval is a conceptually straightforward extension of repeat-pass InSAR approaches, which have also reached a high level of maturity over the last decades. The so-called persistent scatterer interferometry (PSI) techniques are used in order to retrieve deformation maps of the Earth surface with sub-wavelength accuracy (Ferretti et al., 2001; Berardino et al., 2002; Mora et al., 2003; Ferretti et al., 2011). PSI approaches exploit a stack of images in order to mitigate error sources and in this way retrieve and accurate estimate of the deformation time series for the stable scatterers present in the scene. Error sources include the

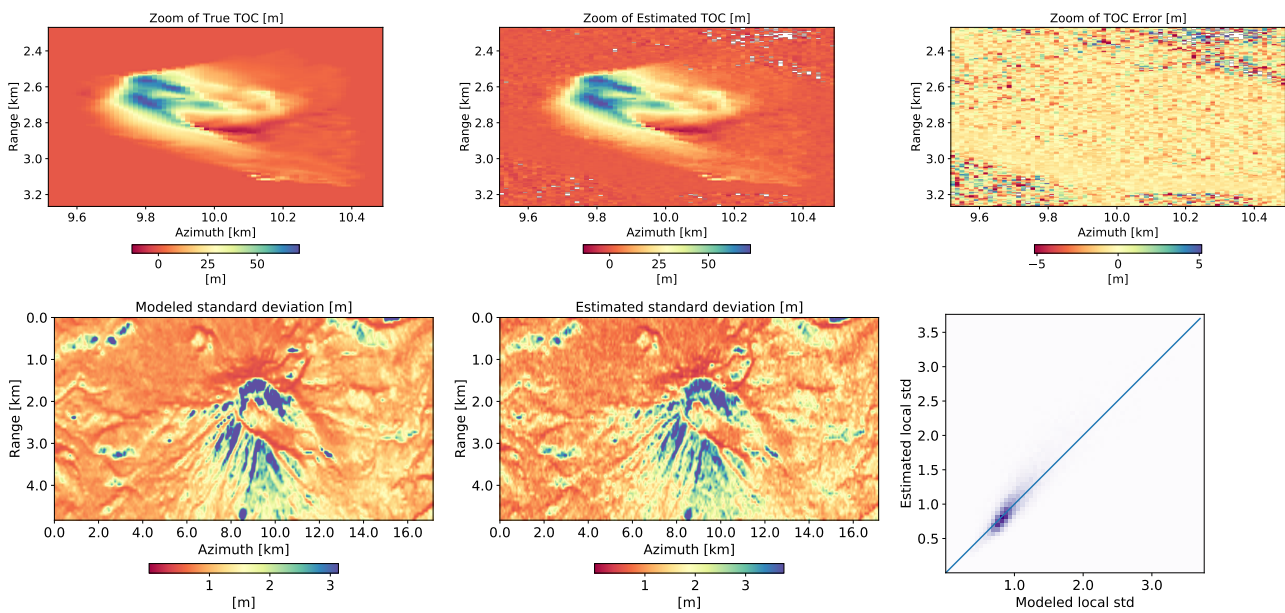


Figure A.12: (Top row) Zoom in of (left) input TOC given to the TOC forward model, (middle) Estimated TOC, and (right) difference between estimated and true TOC. (Bottom row) Performance plots related to (left) the modeled standard deviation, (middle) the standard deviation estimated from data, and (right) the resulting 2D histogram.

atmosphere, baseline errors or residual clock errors in the bistatic case, the latter only in case no synchronisation with the transmitter exists. Among the error sources, the atmosphere, and in particular the troposphere, is the dominant one.

Figure A.13 shows the flow-chart for the TDV product. The flow starts with the interferometric processing of the L1a data in order to obtain L1b coregistered products, a step that needs to consider the particular aspects related to the interferometric processing of TOPS data (Prats-Iraola et al., 2012; Yagüe-Martínez et al., 2016). The stacks are generated at slice level, following the convention of the L1a products. As part of this first processing step, existing techniques which exploit the large bandwidth of the transmitted signal can be applied in order to estimate and mitigate ionospheric artefacts (Gomba et al., 2016).

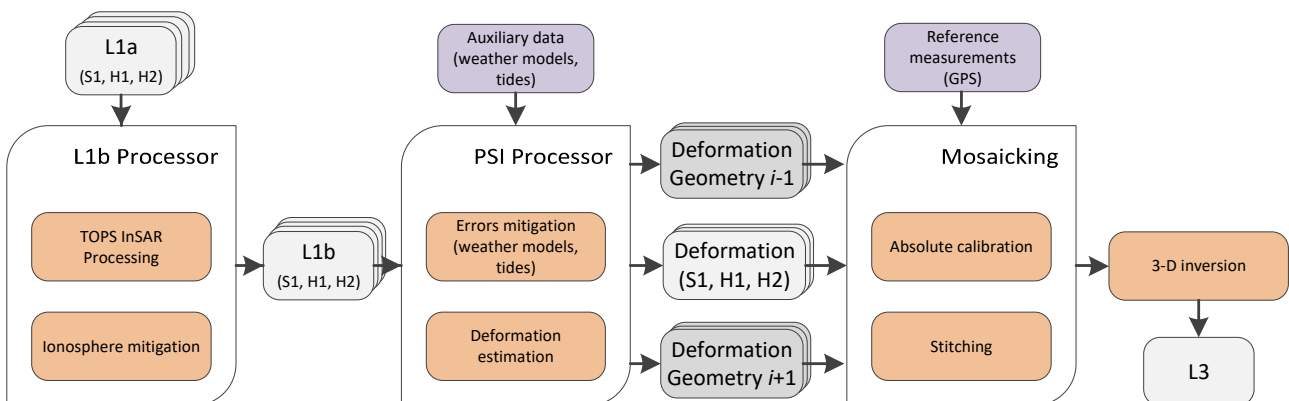


Figure A.13: Schematic flow-chart for the retrieval of the TDV product.

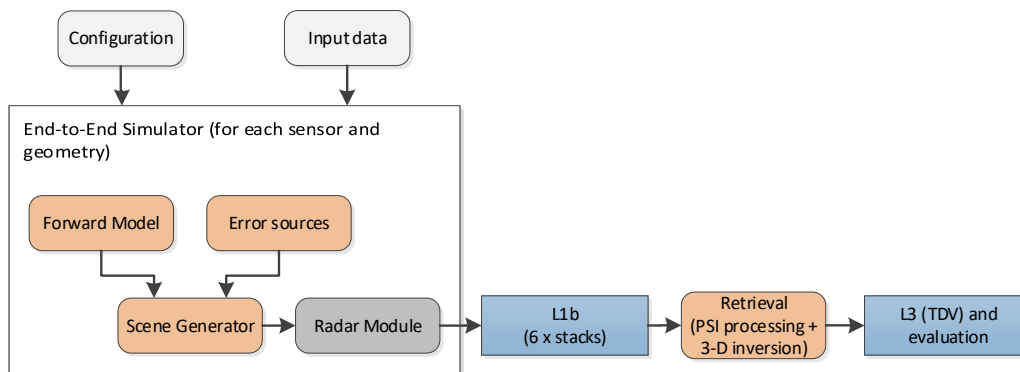


Figure A.14: End-to-end simulator high-level diagram for the simulation and evaluation of TDV products.

Each coregistered stack is then fed into the PSI processing chain to retrieve the deformation in line of sight for each satellite. Here, external information or models are used in order to mitigate external disturbances like the atmosphere (via atmospheric models like the ECMWF ERA-5 model), solid Earth tides, or even ocean tide loading close to coastal areas. The PSI processing chain retrieves the mean deformation velocity and eventually the deformation time series. Mosaicking is then performed to stitch together the retrieved deformation results from neighbouring slices. Absolute calibration is performed within this stage using external reference points like, e.g., GPS measurements. Once each geometry covering a given area of interest has been processed, it is necessary to geocode all geometries to the same geographical grid in order to perform the 3-D inversion.

A.4.2 Performance Estimation

Similar as for the previous applications, the performance for the TDV product has been computed based on analytical solutions (Monti Guarnieri and Tebaldini, 2008; Prats-Iraola et al., 2018) and on a simplified end-to-end simulator DLR (2020b). Figure A.14 shows a high-level diagram of this simplified end-to-end simulator for the TDV product. The input data are based on Sentinel-1 acquisitions in ascending and descending geometries, and also includes pre-computed geometric information in order to simplify the end-to-end simulator. The input data include the LUTs to geocode the information as well as the displacement vector in radar coordinates to allow for a straightforward computation of the LoS displacement. The configuration file includes parameters like the along-track baselines of the Harmonies w.r.t. Sentinel-1, the DTAR and NESZ values for both S1 and Harmony, as well as different configuration parameters for the error sources. A total of six L1b stacks are generated: Sentinel-1, Harmony 1 and Harmony 2, for both ascending and descending geometries. The different blocks are briefly described in the following:

- The **forward model** projects the deformation in line of sight for each acquisition taking into account the acquisition geometry.
- The **error sources** module generates realizations for different error sources, namely, the tropospheric delays by exploiting high resolution ECMWF data, clock errors based on a PSD derived from TanDEM-X clock realizations scaled to C band, baseline errors and ionospheric errors, where scintillations have been generated based on the Rino

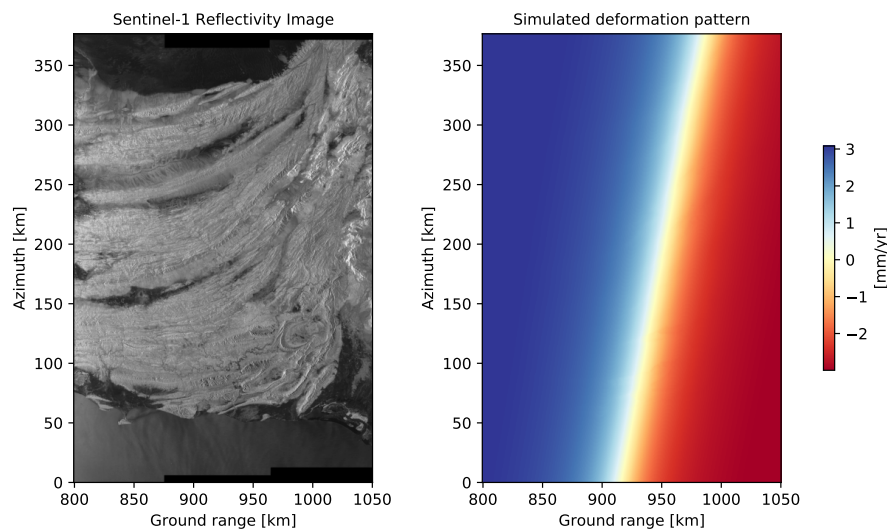


Figure A.15: (Left) Sentinel-1 reflectivity image and (right) simulated north-south mean deformation velocity projected onto the line of sight of the Harmony satellite trailing Sentinel-1, both used for the end-to-end simulation.

spectrum (Rino, 1979). All these errors are computed as 2-D phase screens.

- The **scene generator** module is responsible for the generation of the partially correlated single-look complex images based on a user-given temporal decorrelation model. The module also injects the deformation and error signals into the SLCs.
- The **radar module** includes additional instrument effects like the azimuth ambiguities and the instrument noise floor.
- The **retrieval** module performs a simplified PSI processing. The mean deformation velocity is retrieved for each of the six lines of sight individually, to finally perform the 3-D inversion. In a last step, the error variograms of the retrieved 3-D mean deformation velocity are finally computed and compared to the nominal performance.

Figure A.15 shows the Sentinel-1 reflectivity image for the ascending configuration and the simulated deformation pattern projected in the line of sight of the Harmony satellite trailing Sentinel-1, both projected in ground-range. The acquisition is over the Hoshab fault in Pakistan, and the deformation pattern has been simulated assuming a locked strike-slip fault aligned exactly in the north-south direction, with a slip rate of 2 cm/yr, which is not exactly the true deformation pattern in the area but serves the purpose of the simulation. As commented above, six 5-year stacks have been generated, i.e., one ascending pass and one descending pass. For the sake of the example, a stereo configuration has been assumed, with an along-track baseline of 350 km. Real data from the ECMWF model corresponding to the Sentinel-1 acquisition dates have been used and projected to the three different lines of sight. An aspect that has been carefully accounted for is the fact that the tropospheric component is strongly correlated for the simultaneous acquisitions, which benefits the retrieval of the north-south component of the deformation. Additional error sources have been simulated including clock errors, baseline errors and ionospheric scintillations.

The top row of Figure A.16 shows the retrieved mean deformation velocity in the line of sight for each satellite in the ascending geometry. The result is clearly affected by the most dominant error source, namely, the troposphere. However, most of the tropospheric signal cancels out in the N-S component when performing the 3-D inversion together with the measurements of the descending geometry. This occurs since the tropospheric signal, being the largest error source, is correlated between the three satellites and cancels out almost completely during the 3-D inversion (Prats-Iraola et al., 2018). This is shown in the middle row of Figure A.16, where the deformation pattern occurring only in the N-S direction can be clearly appreciated. Finally, it is interesting to observe in the error variogram how the error for the N-S component varies less than the other components as a function of the distance to the calibration point, due to the aforementioned cancellation of the tropospheric noise in this direction. Results show that the target accuracy of 2 mm/yr at 100 km is achieved. These results are similar to those shown in Section 5.4.4. The major difference lies on the predicted accuracy of the N-S component, which is worse for the analytical approach. This probably occurs because the autocorrelation function assumed for the turbulent troposphere is too pessimistic. Note also that the analytical solution simplifies the modelling of the error sources, while the simulator generates realizations based on realistic models and/or external data.

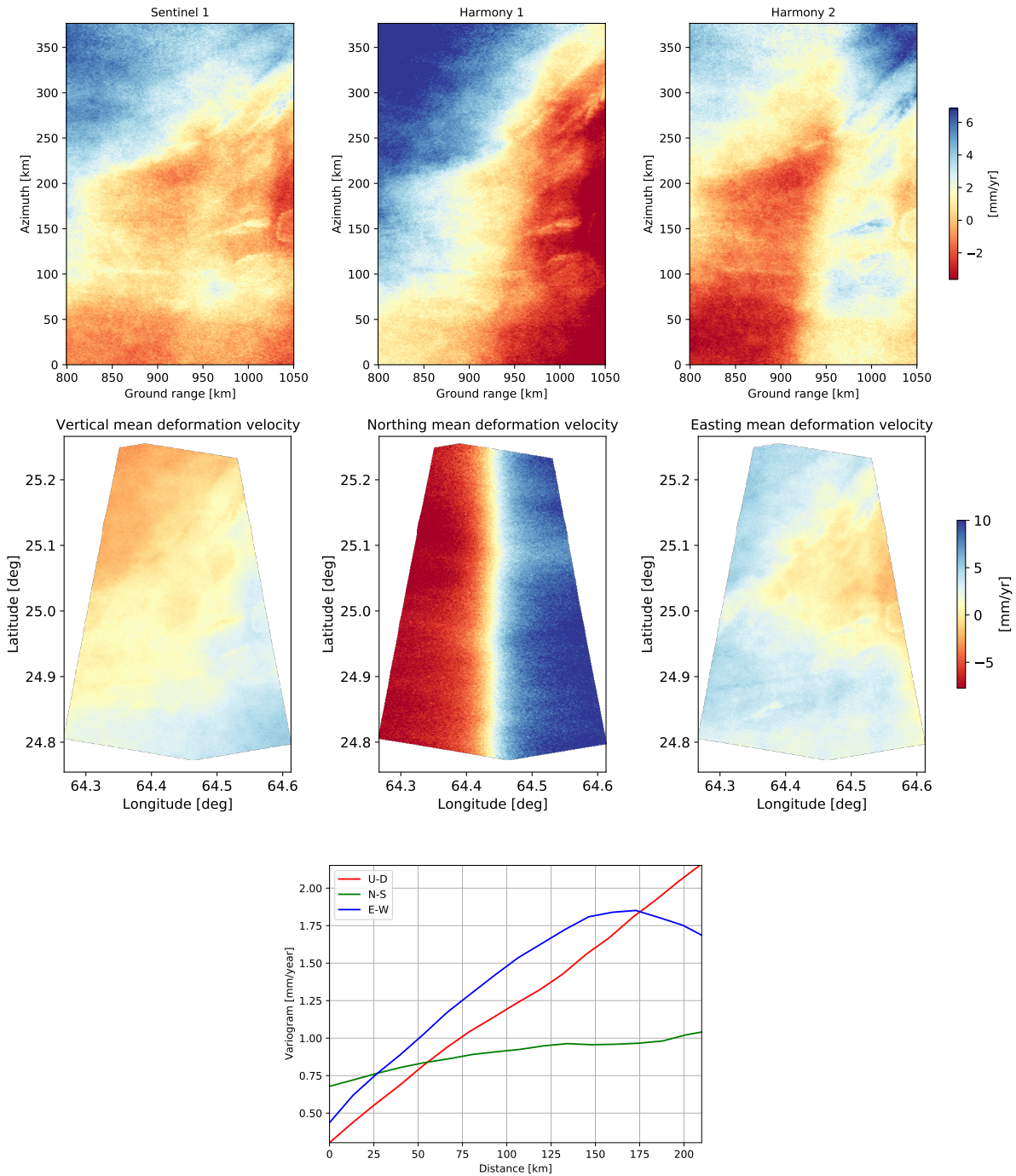


Figure A.16: (Top row) Retrieved mean deformation velocity in line of sight for the ascending geometry for (left) Sentinel 1, (middle) Harmony 1 and (right) Harmony 2. (Middle row) Retrieved mean deformation velocity after the 3-D inversion in a geographical grid, where only the overlap area between ascending and descending geometries is shown. (Bottom row) Error variogram for the three components (note the standard deviation instead of the variance is shown).

B RELEVANCE TO EVALUATION CRITERIA

Relevance to ESA Research Objectives for Earth Observation

As indicated already in Section 3.1, the science goals of Harmony are well embedded within ESA's EO science strategy, as outlined in (Rast and Kern (2015)).

For the *oceans*, Harmony will deliver unique high resolution and information-rich data sets, which are necessary to understand a wide range of submesoscale and mesoscale processes. In doing so, Harmony data, in combination with subsequently improved models and assimilation schemes, will yield a major contribution to addressing **Challenge O2**. Moreover, the joint observations of TSCV, surface winds, wave spectra, and SST are needed to further our scientific understanding of air-sea interactions, and their driving role in weather and climate (**Challenge O4**). In addition, predictions of the future impact of storm surges (part of **Challenge O5**) will benefit from an improved understanding of the underlying storms and associated coastal dynamics.

For the *cryosphere*, Harmony will deliver a fundamental contribution to address **Challenge C2**, by directly quantifying ice volume changes, which will be mapped into mass changes, over ice sheets and glaciers, and downscaling altimeter measurements over ice caps. Through one of its secondary science goals on sea ice deformation, Harmony will address **Challenge C1** by providing unique and necessary observations to understand and quantify sea ice dynamics and rheology, which are required inputs for coupled ice, sea and atmospheric models. For permafrost areas, another Harmony secondary science target, Harmony will address **Challenge C5** by enabling the quantification of both the vertical and lateral components of seasonal and long-term subsidence in these regions. These cryosphere challenges also relate to climate change (all) and sea-level rise (ice sheet dynamics in a warming climate), as expressed in **Challenge O5**. Moreover, mountain glaciers play a fundamental role in the fresh water supply.

For *solid Earth*, Harmony will address **Challenge G1** by providing high-resolution 3-D deformation fields, whose importance is illustrated by the extensive use of geodetic GPS measurements in active seismic and volcanic areas, and by directly measuring volume changes associated to volcanic activities and landslides. In addressing these challenges, Harmony will contribute to understand, monitor, and forecast Natural Hazards. Finally, by providing measurements of topographic change at actively erupting volcanoes, which is a Harmony secondary science goal, the mission contributes to **Challenge G2**.

Need, Usefulness and Excellence

As summarised in the previous section, Harmony's objectives are clearly framed within ESA's EO Strategy, directly addressing **5** of the challenges identified therein through its primary science goals, and yet another **3** through its secondary science goals. The Harmony Mission will provide critical data sets urgently needed for advancing the understanding, modelling and prediction of key processes of the ocean, cryosphere and solid Earth components of the Earth system. The cryosphere-related scientific goals will help quantifying the on-going changes in Earth's climate. The ocean-related and cryosphere-related objectives will provide qualitative and quantitative insight in some of the key physical processes that govern weather and climate, in particular addressing small-scale processes that remain unresolved in Earth System models. The development of high-resolution fully coupled models requires high resolution

observations of the couplings (e.g. ocean-atmosphere interactions) to drive the development and validation of the sub-grid parameterisations. Synergistic operation with Sentinel-1 eliminates one of the main cost drivers of an active mission: the RF power generation subsystems together with the large solar arrays, heavy batteries, and power management units required to feed them. In consequence, within the envelope of an Earth Explorer, Harmony will retain the performance levels of Sentinel-1 in terms of resolution, sensitivity, and coverage, while providing the geometric diversity specifically required together with the addition of multi-view Thermal Infra-Red observations. In summary, Harmony offers an excellent, cost-efficient solution for major advancements in spatially detailed observations of surface motion and deformation of key components of the ocean, atmosphere, cryosphere and solid Earth domains, representing a valuable, innovative add-on to the European Earth Observation Programme.

Uniqueness and Complementarity

For the ocean mission objectives, there is neither existing nor planned mission capable of simultaneously measuring surface currents, surface winds, and characterizing the wave spectra, in particular at kilometer or sub-kilometer resolution. The Earth Explorer 9 candidate mission SKIM was proposed to provide similar measurements, but targeting larger spatial scales associated to different physical phenomena. Harmony will complement wind scatterometers, which provide global low resolution ($O(25\text{ km})$) surface wind-stress observations, which represent wind velocities with respect to largely unknown surface currents. Harmony dynamic surface current information will also be complementary to the geostrophic currents derived from altimeter measurements. Another unique feature of Harmony is that, by operating at C-band, which unlike higher frequencies penetrates even through heavy rain, and by exploiting the multi-static cross-polarized return, it will be the first mission able to provide high resolution measurements of surface winds and currents within extreme weather events such as tropical cyclones.

The collocated SAR and TIR instruments will provide an unprecedented and unique view of the MABL, providing highly spatially resolved surface stress and surface wind and simultaneous motion vectors at the boundary layer top. This will allow a detailed characterization of the 3-D structure of the MABL that is currently only accessible through LES models.

Likewise, for solid Earth, it is notorious that current EO systems are extremely insensitive to North-South displacements. Harmony will fill a clear observational gap and complement point-measurements made by ground-based GNSS receivers. Volume changes have been measured from space with Harmony-like resolution by TanDEM-X. Harmony will allow to quantify changes over decades, by combining its measurements with those previously made by TanDEM-X and SRTM. Fueled by the vast imaging capabilities of Sentinel-1, Harmony will be able to generate DSMs of large regions of interest in matter of weeks, allowing for narrowly time-stamped global inventories of ice volumes, and also for sustained observations of changes over wide areas over a prolonged time.

Degree of Innovation and Contribution to the Advancement of European Earth Observation Capabilities

Harmony will contribute to the development of Earth Observation by implementing the first multi-static SAR mission. The mission combines several innovative concepts, several of which

bear similarities to concepts that have been proposed for previous Earth Explorer calls:

- Multi-static SAR observations
- Large-squint, stereo SAR observations of ocean currents
- Combination of optical and SAR observations from a single platform
- Observing clouds with multi-view TIR instrument from two satellites in stereo configuration

Companion SAR concepts have been an object of intense interest in recent years, as illustrated by the several companion studies funded by ESA, including SAOCOM-CS. Distributed Earth Observation (EO) concepts are also within the research priorities of the European Commission, as expressed in several Horizon 2020 calls and funded projects, such as S3NET (Satellite Swarm Sensor Network) and ONION (Operational Network of Individual Observation Nodes). Harmony would be the first demonstration of a companion satellite and consolidate Europe's leading position in radar-based EO. There is no doubt that there will be many challenges to be overcome in the design and implementation of such a system-of-systems. Once its unique abilities will have been demonstrated however, they could very likely pave the way towards a more widespread adoption of companion satellites in an operational context (Sentinel-1, ROSE-L).

Another innovation is the combination of TIR payload with a radar payload in order to offer simultaneous multi-sensor observations. This classically difficult combination of instruments is made possible by exploiting the steady miniaturisation of TIR payloads and the use of on-board processing techniques. Riding on the successes of ESA's cubesat programme, technologies developed in the new-space arena are now being proposed to augment a more classically developed Earth Explorer mission, to produce science that was until recently impossible to achieve within realistic budgetary constraints.

Feasibility and Level of Maturity

Summary

The Phase 0 concluded that the Harmony mission will enable a significant advance in the identified scientific domains. Each of the domains have clearly formulated scientific objectives that are organised as primary and secondary objectives, for which studies have confirmed all primary objectives can be fully met by the mission. The Phase 0 has successfully identified, for each consortium, a system concept capable to meet Harmony's mission objectives and requirements consisting of two spacecraft flying in formation with Sentinel 1 and embarking a Receive only C-band SAR and a 4-band thermal infrared imager. The two Harmony satellites will be launched in Vega-C either stacked in single or in dual configuration. Phase 0 has successfully identified the main technical risks and the critical aspects of the mission, which are detailed in this chapter.

Harmony is not considered to be a technologically risky mission since its technical concept is based on strong and long-lasting European heritage in both SAR and Infrared optical payloads and since its basic measurement principles and are well known and established. Nevertheless, the mission is not exempt of technical challenges such as the synchronisation with Sentinel 1 and between satellites, the high pointing knowledge accuracy required, the radiometric requirements for the optical payload, the adaptation of existing antenna sub-array

technology, the impact of synergistic SAR and optical observations into the mission design (e.g. co-registration) and the optimisation of the spacecraft design to fit into the Vega-C launcher. The latter is a critical risk for the mission, given the low mass margin at this early project stage.

Science

For the *solid Earth* and *cryosphere* domain applications, the observation techniques are natural extensions of proven techniques with current SRL of 4 or higher. Well-understood retrieval algorithms are readily available and can be easily adapted to Harmony's unique viewing geometry. This has allowed to already integrate - at Phase 0 stage - the retrieval algorithms in the performance analysis and take the end-to-end performances into account in the design of the system (as described in section 5.4). Retrieval of ocean products will be more challenging, due to the smaller amount of heritage and also due to complexity of the inversion, which depends on the development of robust models to separate the different contributions to the radar observables. A number of ongoing and finalised ESA studies, either related to bi- and multi-static SAR concepts or to other mission concepts (e.g. SKIM), have furthered the knowledge and state-of-the-art of microwave interaction mechanisms at interplay with a dynamical ocean surface (and associated retrieval algorithms) paving the way for allowing accurate end-to-end performance assessment tools for Harmony. From a retrieval point of view, Harmony will also directly benefit from studies and airborne campaigns done in the context of Wavemill and the Ocean Surface Current Airborne Radar Demonstrator (OSCAR) currently in development by ESA. Specific campaigns for Harmony are either ongoing (i.e. WaddenSAR) or being planned for 2021 – where it is to be noted that the observational concepts for these campaigns have a sufficient level of maturity. In addition, the downscaling and use of scatterometer methodologies for retrieval and validation will much benefit Harmony (Stoffelen, 2017). For *cryosphere* and *solid Earth* there is a solid user community that routinely uses Sentinel-1 and other SAR data, and with the expertise to develop and use the Level-2/-3 products that Harmony will produce.

Platform and mission

Harmony will fly in the same orbit as S1, which opens the possibility for re-use or adaptation of standard Low Earth Orbit (LEO) Earth Observation platforms with reduce re-qualification.

Consortium A is proposing a platform concept based on the full re-use with minor adaptation of the LSTM platform, currently in phase B2 and due for launch in 2028. All equipment of the platform are considered to be at Technology Readiness Level (TRL) 6 or higher with exception of the mass memory (which is TRL 5), the gyro (which will likely be replaced for Harmony) and the software which are at TRL 4. No major technical risks nor challenges are perceived at this moment.

Consortium B is proposing a custom-based platform concept, driven by the need to launch in stacked configuration, reusing existing platform subsystems and equipment. All equipment of the platform are at TRL 5 or higher. No major technical risks nor challenges are perceived at this moment with the exception of the specific development of the separation system between the two stacked spacecraft.

With respect to the current VEGA-C launcher user manual, the mass margin for both concepts is marginal. This is considered a risk for the mission since the options to reduce mass

at platform level are limited without compromising performance. Concept A is compatible with the VEGA-C dual launch configuration, using the standard VESPA adapter for VEGA. Concept B stacks both Harmony satellites and is compatible with a single launch configuration with standard launch adapter. Separation devices and mechanisms for Concept B will require specific design and qualification.

The SAR instrument on Harmony requires to be synchronised with that of S1. This risk has been reduced during Phase 0 activities to the smaller issue of fine-time synchronisation. Should this perform not as good as expected, it may have an affect on either the volume or the latency of the data to be transmitted to ground.

The mission is expected and assumed to be compatible with a non-controlled re-entry in the atmosphere. Controlled re-entry would not be compatible with the launch of both Harmony satellites on VEGA-C, posing considerable programmatic risk for the mission. A more detailed analysis will be carried out in Phase A.

The Technology Readiness Level (TRL) of the platform is considered to be 5 or above for all hardware units on both concepts. The software is considered at TRL 4.

Payload

The Harmony satellites carry two instruments: a receive-only C-band SAR and a 4-band, 5-cameras TIR optical imager. Both instruments build upon large European heritage from already flying missions or from missions currently under development.

The SAR instrument is similar in function to the Sentinel-1 antenna, except that it does not need the transmit function. Both consortia are favouring to upgrade to newer technology rather than re-using the technology used in the first generation of S1 satellites. The SAR has two main subsystems: the antenna or SAS and the central electronics or SES. Consortium A has highlighted the subarrays and the front-end Rx modules as TRL 3 items. Consortium B has highlighted the subarrays, the hinges and the Hold-down and Release Mechanism (HRM)s as TRL 3 items. All other elements are at TRL 5 or above for both concepts. For the SES, both consortia can benefit from parallel development activities outside the perimeter of the Harmony project. Concept A will use the Universal Processing module (UPM) standard product which is undergoing qualification with an EQM programme that will demonstrate the critical functions of the central electronics. Concept B relies on an ongoing development activity that is more specific to bistatic SAR (SAOCOM-CS heritage). Both Electronics are currently at TRL 3.

The optical instrument is a multi-band and multi-view thermal infrared imager. The baseline detector is a ULIS Pico1024 off-the-shelf component (TRL 9). The required radiometric performance of the ULIS Pico1024 microbolometer is however at the edge of what this technology can provide. Harmony will require further development and understanding on noise reduction techniques to increase the typical microbolometer performance. All elements of the instrument (cameras, control unit, mechanisms, calibration source, structure and thermal) are at TRL 4 or higher. The critical components are the calibration subsystem and the focal plane assembly, which have a TRL of 5 and 4 respectively. The latter assessment is based on the required modification to the filter mounting/packaging onto the detector.

The SAR sub-arrays, the front-end Receiving modules and the Central Electronic are considered to be at TRL 3 for concept A. For Concept B, the sub-arrays, the antenna hinges and the central electronics are considered to be at TRL 3. All units of the optical instrument are considered to be at TRL 4 or above for both concepts.

Plan to raise TRL to 5 by the end of Phase B1

Both consortia are proposing pre-development activities for all elements of the SAR antenna that are TRL 3, with the aim of reaching TRL 4 by end of Phase A and TRL 5 by end of phase B1. These are the subarrays (for both concept A and B), the Front End (FE) receive modules (concept A) and the mechanical support hardware (hinges, HRM, concept B). It can be noted that for both consortia the trade-off between subarray technologies is still open and will be closed in Phase A.

The development of the central electronics for concept A will rely on the ongoing generic UPM development, which is undergoing qualification with an EQM programme that will demonstrate the critical functions of the central electronics to TRL 7 by the end of the Harmony Phase A. The ongoing development targets missions that will operate in the same environment as Harmony. It is likely however that some modifications will be required to this generic development to customise the solution for the Harmony mission (class C heritage category). These modifications will not change the critical functions but mainly implemented through a firmware update. Therefore, it is reasonable to still assume that TRL 6 will be achieved by the end of phase B1. The timeline of this development is also driven by the ROSE-L mission and therefore considered robust with respect to the Harmony needs. Concept B relies on an ongoing development activity that is more specific to bistatic SAR (SAOCOM-CS heritage). This activity includes an Engineering Model (EM) and will demonstrate the critical functions of the central electronics to TRL 6. An additional pre-development activity specific for Harmony may need to be considered in Phase A to ensure that all Harmony specific requirements are covered.

A Phase A pre-development is being considered by both consortia for the Focal Plane Assembly (FPA) of the optical instrument, which includes the mounting of the spectral filters on the detector and the Front End Electronics (FEE).

The plan is considered technically adequate to raise the TRL of the critical instrument units/technology to TRL 5 at the end of Phase B1.

Timeliness

User perspective

The mission is timely because the topics addressed are pressing in view of open issues in Earth system science and global change research, as well as related societal issues. The mission will provide unique, spatially detailed observations of motion and deformation fields of the ocean surface, clouds, glaciers, ice sheets, and solid Earth. These observations are of particular relevance for advancing and validating numerical models in order to capture and predict detailed variations and trends in dynamic features of ocean, cryosphere and solid Earth processes. Advancing the observation of these processes is very timely because it provides essential data for further improvement of models on ocean circulation, ice/climate interactions and geohazard assessment that are currently lacking comprehensive information on spatially de-

tailed representation of motion and deformation fields. By 2027/28 the atmosphere-ocean-ice-land system will be viewed as a fully coupled system, modelled with improved spatio-temporal and model physics. Yet, the fine-scale Harmony measurements will play a crucial role in assessing uncertainties in model physics and overcome challenges in predictions for both research and stakeholders. Extreme weather, coastal and marginal-ice-zone studies will certainly remain strong drivers.

Technological perspective

The Harmony mission concept has been readied over the course of numerous ESA activities related to bistatic SAR. The mission can benefit from the extensive know-how and heritage that is currently available. From a technology point of view, there are no obstacles to implement Harmony within the timeframe of Earth Explorer 10 (EE-10). From the other hand, an interesting aspect to consider is that Harmony is conceived to fly with S1-D, the last of the current series of European C-band SAR satellites. The next generation of Sentinel-1 satellites (S1-NG) will enter phase A not long after EE-10. Thus, EE-10 provides the last window of opportunity to demonstrate the power of a SAR companion system within the envelope of the Earth Explorer programme to help steer the design of S1-NG in a companion-friendly direction.

Programmatics

Model Philosophy and Development approach

Harmony will follow a phased development process (Phase B1 and B2/C/D/E1), with reviews at the end of each phase, i.e. System Requirements Review SRR at end of Phase B1, Preliminary Design Review PDR at end of Phase B2, Critical Design Review CDR at the end of Phase C, etc. This will allow verifying the status of the system design, development, procurement and integration of development and flight models.

Both consortia are proposing a PFM/FM2 approach to build the first and second of the Harmony satellites. Before that, in phase C, the development approaches and model philosophies are quite different and reflect the different approaches for the platform (full re-use for consortium A and dedicated development for consortium B). Consortium A does not foresee a Structural Model (SM) or Structural and Thermal Model (STM) for mechanical qualification of the platform. Furthermore, the functional verification and EM can be simplified as not all units need to be tested with hardware in the loop. Consortium B proposes a SM including at least the primary structure of both Harmony satellites in order to mechanically test the stacking of the satellites.

At SAR payload level, both consortia propose a classic EQM-PFM-FM2 approach, although there are some differences. Consortium A proposes to reduce the EQM to have a single antenna panel, and includes a separate SM for structural qualification of the antenna.

For the optical payload, consortium A proposes a minimalist development with an Electrical and Functional Model (EFM), Proto-Flight Model (PFM) and Flight Model (FM), whereas consortium B is proposing to have in addition an STM and Qualification Model (QM).

Schedule

The Harmony schedule is driven by the development of the C-band SAR, and by the development and testing two satellites. The Harmony schedule assumes a phase B1 starting in Q3



2022 and a phase B2/C/D starting in Q3 2024. Under these assumptions, a launch in 2028 is not considered feasible. A launch within 2029 could be possible with appropriate schedule optimisation.

References

- Abdullahi, S., Wessel, B., Huber, M., Wendleder, A., Roth, A., and Kuenzer, C. (2019). Estimating Penetration-Related X-Band InSAR Elevation Bias: A Study over the Greenland Ice Sheet. *Remote Sensing*, 11(24):2903. Number: 24 Publisher: Multidisciplinary Digital Publishing Institute.
- Alford, M. H., MacKinnon, J. A., Simmons, H. L., and Nash, J. D. (2016). Near-Inertial Internal Gravity Waves in the Ocean. *Annual Review of Marine Science*, 8(1):95–123. _eprint: <https://doi.org/10.1146/annurev-marine-010814-015746>.
- Alpers, W. (1985). Theory of radar imaging of internal waves. *Nature*, 314(6008):245–247.
- Ansari, H., Zan, F. D., Parizzi, A., Eineder, M., Goel, K., and Adam, N. (2016). Measuring 3-D Surface Motion With Future SAR Systems Based on Reflector Antennae. *IEEE Geoscience and Remote Sensing Letters*, 13(2):272–276.
- Ardhuin, F., Brandt, P., Gaultier, L., Donlon, C., Battaglia, A., Boy, F., Casal, T., Chapron, B., Collard, F., Cravatte, S., Delouis, J.-M., De Witte, E., Dibarboure, G., Engen, G., Johnsen, H., Lique, C., Lopez-Dekker, P., Maes, C., Martin, A., Marié, L., Menemenlis, D., Nougier, F., Peureux, C., Rampal, P., Ressler, G., Rio, M.-H., Rommen, B., Shutler, J. D., Suess, M., Tsamados, M., Ubelmann, C., van Sebille, E., van den Oever, M., and Stammer, D. (2019). SKIM, a Candidate Satellite Mission Exploring Global Ocean Currents and Waves. *Frontiers in Marine Science*, 6.
- Ardhuin, F., Collard, F., Chapron, B., Girard□Ardhuin, F., Guitton, G., Mouche, A., and Stopa, J. E. (2015). Estimates of ocean wave heights and attenuation in sea ice using the SAR wave mode on Sentinel-1A. *Geophysical Research Letters*, 42(7):2317–2325. _eprint: <https://agupubs.onlinelibrary.wiley.com/doi/pdf/10.1002/2014GL062940>.
- Belmonte Rivas, M., Ootosaka, I., Stoffelen, A., and Verhoef, A. (2018). A scatterometer record of sea ice extents and backscatter: 1992–2016. *The Cryosphere*, 12:2941–2953.
- Belmonte Rivas, M. and Stoffelen, A. (2019). Characterizing ERA-Interim and ERA5 surface wind biases using ASCAT. *Ocean Science*, 15(3):831–852.
- Berardino, P., Fornaro, G., Lanari, R., and Sansosti, E. (2002). A new algorithm for surface deformation monitoring based on small baseline differential SAR interferograms. *IEEE Transactions on Geoscience and Remote Sensing*, 40(11):2375–2383.
- Biskaborn, B. K., Smith, S. L., Noetzli, J., Matthes, H., Vieira, G., Streletskiy, D. A., Schoeneich, P., Romanovsky, V. E., Lewkowicz, A. G., Abramov, A., Allard, M., Boike, J., Cable, W. L., Christiansen, H. H., Delaloye, R., Diekmann, B., Drozdov, D., Etzelmüller, B., Grosse, G., Guglielmin, M., Ingeman-Nielsen, T., Isaksen, K., Ishikawa, M., Johansson, M., Johansson, H., Joo, A., Kaverin, D., Kholodov, A., Konstantinov, P., Kröger, T., Lambiel, C., Lanckman, J. P., Luo, D., Malkova, G., Meiklejohn, I., Moskalenko, N., Oliva, M., Phillips, M., Ramos, M., Sannel, A. B. K., Sergeev, D., Seybold, C., Skryabin, P., Vasiliev, A., Wu, Q., Yoshikawa, K., Zheleznyak, M., and Lantuit, H. (2019). Permafrost is warming at a global scale. *Nature Communications*.
- Boccaletti, G., Ferrari, R., and Fox-Kemper, B. (2007). Mixed layer instabilities and restratification. *J. Physical Oceanography*, 37:2228–2250.

- Bolton, T. and Zanna, L. (2019). Applications of Deep Learning to Ocean Data Inference and Subgrid Parameterization. *Journal of Advances in Modeling Earth Systems*, 11(1):376–399. _eprint: <https://agupubs.onlinelibrary.wiley.com/doi/pdf/10.1029/2018MS001472>.
- Chapron, B., Collard, F., and Ardhuin, F. (2005). Direct measurements of ocean surface velocity from space: Interpretation and validation. *Journal of Geophysical Research: Oceans*, 110(C7):n/a–n/a.
- Chelton, D. B., DeSzoeke, R. A., Schlax, M. G., El Naggar, K., and Siwertz, N. (1998). Geographical variability of the first baroclinic Rossby radius of deformation. *Journal of Physical Oceanography*, 28(3):433–460.
- Chelton, D. B. and Xie, S.-P. (2010). Coupled Ocean-Atmosphere Interaction at Oceanic Mesoscales. *Oceanography*, 23(4):52–69. Publisher: Oceanography Society.
- Chiang, T.-L., Wu, C.-R., and Oey, L.-Y. (2011). Typhoon Kai-Tak: An Ocean's Perfect Storm. *Journal of Physical Oceanography*, 41(1):221–233. Publisher: American Meteorological Society.
- Ciani, D., Buongiorno Nardelli, B., and Liberti, G. (2020). Analysis of the L1 products & requirements for the Harmony TIR instrument. Technical Report.
- Collard, F., Ardhuin, F., and Chapron, B. (2005). Extraction of coastal ocean wave fields from SAR images. *IEEE Journal of Oceanic Engineering*, 30(3):526–533. Conference Name: IEEE Journal of Oceanic Engineering.
- Combot, C., Mouche, A., Knaff, J., Zhao, Y., Zhao, Y., Vinour, L., Quilfen, Y., and Chapron, B. (2020). Extensive high-resolution Synthetic Aperture Radar (SAR) data analysis of Tropical Cyclones: comparisons with SFMR flights and Best-Track. *Monthly Weather Review*, pages 1–67.
- Curlander, J. C., Holt, B., and Hussey, K. J. (1985). Determination of Sea Ice Motion Using Digital SAR Imagery. *IEEE Journal of Oceanic Engineering*.
- Dall, J. (2007). InSAR Elevation Bias Caused by Penetration Into Uniform Volumes. *IEEE Transactions on Geoscience and Remote Sensing*, 45(7):2319–2324. Conference Name: IEEE Transactions on Geoscience and Remote Sensing.
- Dare, R. A. and McBride, J. L. (2011). Sea Surface Temperature Response to Tropical Cyclones. *Monthly Weather Review*, 139(12):3798–3808. Publisher: American Meteorological Society.
- D'Asaro, E. A., Sanford, T. B., Niler, P. P., and Terrill, E. J. (2007). Cold wake of Hurricane Frances. *Geophysical Research Letters*, 34(15). _eprint: <https://agupubs.onlinelibrary.wiley.com/doi/pdf/10.1029/2007GL030160>.
- DLR (2020a). D2: Technical note on the observation scenarios, performance metrics and performance models. HMNY-DLR-TN-01, Issue 1.2.
- DLR (2020b). D3: Forward model algorithm theoretical baseline document. HMNY-DLR-TN-02, Issue 1.0.
- D'Asaro, E. A., Shcherbina, A. Y., Klymak, J. M., Molemaker, J., Novelli, G., Guigand, C. M.,

- Haza, A. C., Haus, B. K., Ryan, E. H., Jacobs, G. A., Huntley, H. S., Laxague, N. J. M., Chen, S., Judt, F., McWilliams, J. C., Barkan, R., Kirwan, A. D., Poje, A. C., and Özgökmen, T. M. (2018). Ocean convergence and the dispersion of flotsam. *Proceedings of the National Academy of Sciences*, 115(6):1162–1167. Publisher: National Academy of Sciences Section: Physical Sciences.
- Ebmeier, S., Andrews, B., Araya, M., Arnold, D., Biggs, J., Cooper, C., Cottrell, E., Furtney, M., Hickey, J., Jay, J., et al. (2018). Synthesis of global satellite observations of magmatic and volcanic deformation: implications for volcano monitoring & the lateral extent of magmatic domains. *Journal of Applied Volcanology*, 7(1):2.
- Eden, C. and Dietze, H. (2009). Effects of mesoscale eddy/wind interactions on biological new production and eddy kinetic energy. *Journal of Geophysical Research: Oceans*, 114(C5). _eprint: <https://agupubs.onlinelibrary.wiley.com/doi/pdf/10.1029/2008JC005129>.
- Elliott, J. R., Walters, R. J., and Wright, T. J. (2016). The role of space-based observation in understanding and responding to active tectonics and earthquakes. *Nature Communications*, 7:13844.
- Emanuel, K. (2002). A simple model of multiple climate regimes. *J. Geophys. Res.*, 107(O).
- Engen, G. and Johnsen, H. (1995). SAR-ocean wave inversion using image cross spectra. *IEEE Transactions on Geoscience and Remote Sensing*, 33(4):1047–1056.
- ESA (2020). Harmony working assumptions on sentinel-1 operations. EOP-ΦMP/2020-06-2206 issue 1.1.
- Farr, T. G., Rosen, P. A., Caro, E., Crippen, R., Duren, R., Hensley, S., Kobrick, M., Paller, M., Rodriguez, E., Roth, L., Seal, D., Shaffer, S., Shimada, J., Umland, J., Werner, M., Oskin, M., Burbank, D., and Alsdorf, D. (2007). The Shuttle Radar Topography Mission. *Reviews of Geophysics*, 45:33 PP.
- Ferretti, A., Fumagalli, A., Novali, F., Prati, C., Rocca, F., and Rucci, A. (2011). A New Algorithm for Processing Interferometric Data-Stacks: SqueeSAR. *IEEE Transactions on Geoscience and Remote Sensing*, 49(9):3460–3470.
- Ferretti, A., Prati, C., and Rocca, F. (2001). Permanent scatterers in SAR interferometry. *IEEE Transactions on Geoscience and Remote Sensing*, 39(1):8–20.
- Fox-Kemper, B., Ferrari, R., and Hallberg, R. (2008). Parameterization of Mixed Layer Eddies. Part I: Theory and Diagnosis. *Journal of Physical Oceanography*, 38(6):1145–1165. Publisher: American Meteorological Society.
- Frew, N. M., Goldman, J. C., Dennett, M. R., and Johnson, A. S. (1990). Impact of phytoplankton-generated surfactants on air-sea gas exchange. *Journal of Geophysical Research: Oceans*, 95(C3):3337–3352. _eprint: <https://agupubs.onlinelibrary.wiley.com/doi/pdf/10.1029/JC095iC03p03337>.
- Gall, R., Franklin, J., Marks, F., Rappaport, E. N., and Toepfer, F. (2013). The Hurricane Forecast Improvement Project. *Bulletin of the American Meteorological Society*, 94(3):329–343. Publisher: American Meteorological Society.

- Gatelli, F., Monti Guarnieri, A., Parizzi, F., Pasquali, P., Prati, C., and Rocca, F. (1994). The wavenumber shift in SAR interferometry. *Geoscience and Remote Sensing, IEEE Transactions on*, 32(4):855–865.
- Gaube, P., Chickadel, C. C., Branch, R., and Jessup, A. (2019). Satellite Observations of SST-Induced Wind Speed Perturbation at the Oceanic Submesoscale. *Geophysical Research Letters*, 46(5):2690–2695. _eprint: <https://agupubs.onlinelibrary.wiley.com/doi/pdf/10.1029/2018GL080807>.
- Geiger, C. A. and Drinkwater, M. R. (2001). Impact of Temporal-Spatio Resolution on Sea-Ice Drift and Deformation.
- Geiger, C. A. and Drinkwater, M. R. (2005). Coincident buoy- and SAR-derived surface fluxes in the western Weddell Sea during Ice Station Weddell 1992. *Journal of Geophysical Research C: Oceans*.
- Gentemann, C. L., Clayson, C. A., Brown, S., Lee, T., Parfitt, R., Farrar, J. T., Bourassa, M., Minnett, P. J., Seo, H., Gille, S. T., and Zlotnicki, V. (2020). FluxSat: Measuring the Ocean–Atmosphere Turbulent Exchange of Heat and Moisture from Space. *Remote Sensing*, 12(11):1796. Number: 11 Publisher: Multidisciplinary Digital Publishing Institute.
- Gilbert, A., Leinss, S., Kargel, J., Kääh, A., Gascoin, S., Leonard, G., Berthier, E., Karki, A., and Yao, T. (2018). Mechanisms leading to the 2016 giant twin glacier collapses, Aru Range, Tibet. *Cryosphere*.
- Glaciers-CCI (2019). Esa glaciers cci, user requirements document (urd).
- Gomba, G., González, F. R., and Zan, F. D. (2016). Ionospheric Phase Screen Compensation for the Sentinel-1 TOPS and ALOS-2 ScanSAR Modes. *IEEE Transactions on Geoscience and Remote Sensing*, PP(99):1–13.
- Gray, L. (2011). Using multiple RADARSAT InSAR pairs to estimate a full three-dimensional solution for glacial ice movement. *Geophysical Research Letters*.
- Gudmundsson, S., Sigmundsson, F., and Carstensen, J. M. (2002). Three-dimensional surface motion maps estimated from combined interferometric synthetic aperture radar and GPS data. *Journal of Geophysical Research: Solid Earth*.
- Heus, T., van Heerwaarden, C., Jonker, H., Siebesma, A., Axelsen, S., Dries, K., Geofroy, O., Moene, A., Pino Gonzalez, D., Roode, S., and Arellano, J. (2010). Formulation of and numerical studies with the Dutch Atmospheric Large-Eddy Simulation (DALES). *Geoscientific Model Development Discussions*, 3.
- Hirons, L. C., Klingaman, N. P., and Woolnough, S. J. (2018). The Impact of Air-Sea Interactions on the Representation of Tropical Precipitation Extremes. *Journal of Advances in Modeling Earth Systems*, 10(2):550–559.
- Hoen, E. W. and Zebker, H. A. (2000). Penetration depths inferred from interferometric volume decorrelation observed over the Greenland Ice Sheet. *IEEE Transactions on Geoscience and Remote Sensing*, 38(6):2571–2583. Conference Name: IEEE Transactions on Geoscience and Remote Sensing.
- Hoogeboom, P., Stoffelen, A., and Lopez-Dekker, P. (2018). DopSCA, Scatterometer-based

- Simultaneous Ocean Vector Current and Wind Estimation. In *2018 Doppler Oceanography from Space (DOFS)*, pages 1–9. ISSN: null.
- Horstmann, J. and Koch, W. (2005). Measurement of Ocean Surface Winds Using Synthetic Aperture Radars. *IEEE Journal of Oceanic Engineering*, 30(3):508–515.
- Horstmann, J., Schiller, H., Schulz-Stellenfleth, J., and Lehner, S. (2003). Global wind speed retrieval from SAR. *IEEE Transactions on Geoscience and Remote Sensing*, 41(10):2277–2286. Conference Name: IEEE Transactions on Geoscience and Remote Sensing.
- Horváth, □ and Davies, R. (2001). Feasibility and Error Analysis of Cloud Motion Wind Extraction from Near-Simultaneous Multiangle MISR Measurements. *Journal of Atmospheric and Oceanic Technology*, 18(4):591–608. Publisher: American Meteorological Society.
- Howell, S. E., Komarov, A. S., Dabboor, M., Montpetit, B., Brady, M., Scharien, R. K., Mahmud, M. S., Nandan, V., Geldsetzer, T., and Yackel, J. J. (2018). Comparing L- and C-band synthetic aperture radar estimates of sea ice motion over different ice regimes. *Remote Sensing of Environment*.
- Hsu, M.-K., Liu, A. K., and Liu, C. (2000). A study of internal waves in the China Seas and Yellow Sea using SAR. *Continental Shelf Research*, 20(4):389–410.
- Hutchinson, D. K., Hogg, A. M. C., and Blundell, J. R. (2010). Southern Ocean Response to Relative Velocity Wind Stress Forcing. *Journal of Physical Oceanography*, 40(2):326–339. Publisher: American Meteorological Society.
- IPCC, editor (2014). *Climate Change 2013 - The Physical Science Basis: Working Group I Contribution to the Fifth Assessment Report of the Intergovernmental Panel on Climate Change*. Cambridge University Press, Cambridge.
- Ivanov, A. Y. and Ginzburg, A. I. (2002). Oceanic eddies in synthetic aperture radar images. *Journal of Earth System Science*, 111(3):281.
- Jansen, M. and Ferrari, R. (2009). Impact of the latitudinal distribution of tropical cyclones on ocean heat transport. *Geophysical Research Letters*, 36(6). _eprint: <https://agupubs.onlinelibrary.wiley.com/doi/pdf/10.1029/2008GLO36796>.
- Joughin, I., E. Shean, D., E. Smith, B., and Floricioiu, D. (2020). A decade of variability on Jakobshavn Isbræ: Ocean temperatures pace speed through influence on mélange rigidity. *Cryosphere*.
- Joughin, I. R., Kwok, R., and Fahnestock, M. A. (1998). Interferometric estimation of three-dimensional ice-flow using ascending and descending passes. *IEEE Transactions on Geoscience and Remote Sensing*, 36(1):25–37.
- Kääb, A., Leinss, S., Gilbert, A., Bühler, Y., Gascoïn, S., Evans, S. G., Bartelt, P., Berthier, E., Brun, F., Chao, W. A., Farinotti, D., Gimbert, F., Guo, W., Huggel, C., Kargel, J. S., Leonard, G. J., Tian, L., Treichler, D., and Yao, T. (2018). Massive collapse of two glaciers in western Tibet in 2016 after surge-like instability. *Nature Geoscience*.
- Karvonen, J. (2012). Operational SAR-based sea ice drift monitoring over the Baltic Sea.

Ocean Science, 8:473–483.

- Kerbaol, V., Chapron, B., and Vachon, P. W. (1998). Analysis of ERS-1/2 synthetic aperture radar wave mode images. *Journal of Geophysical Research: Oceans*, 103(C4):7833–7846. _eprint: <https://agupubs.onlinelibrary.wiley.com/doi/pdf/10.1029/97JC01579>.
- Kilic, L., Prigent, C., Aires, F., Boutin, J., Heygster, G., Tonboe, R. T., Roquet, H., Jimenez, C., and Donlon, C. (2018). Expected Performances of the Copernicus Imaging Microwave Radiometer (CIMR) for an All-Weather and High Spatial Resolution Estimation of Ocean and Sea Ice Parameters. *Journal of Geophysical Research: Oceans*, 123(10):7564–7580. _eprint: <https://agupubs.onlinelibrary.wiley.com/doi/pdf/10.1029/2018JC014408>.
- King, M. D., Howat, I. M., Candela, S. G., Noh, M. J., Jeong, S., Noël, B. P. Y., van den Broeke, M. R., Wouters, B., and Negrete, A. (2020). Dynamic ice loss from the Greenland Ice Sheet driven by sustained glacier retreat. *Communications Earth & Environment*.
- Klein, S. A., Hartmann, D. L., and Norris, J. R. (1995). On the Relationships among Low-Cloud Structure, Sea Surface Temperature, and Atmospheric Circulation in the Summer-time Northeast Pacific. *Journal of Climate*, 8(5):1140–1155. Publisher: American Meteorological Society.
- Krieger, G., Moreira, A., Fiedler, H., Hajnsek, I., Werner, M., Younis, M., and Zink, M. (2007). TanDEM-X: A Satellite Formation for High-Resolution SAR Interferometry. *IEEE Transactions on Geoscience and Remote Sensing*, 45(11):3317–3341.
- Krieger, G., Zink, M., Bachmann, M., Bräutigam, B., Schulze, D., Martone, M., Rizzoli, P., Steinbrecher, U., Walter Antony, J., De Zan, F., Hajnsek, I., Papathanassiou, K., Kugler, F., Rodriguez Cassola, M., Younis, M., Baumgartner, S., López-Dekker, P., Prats, P., and Moreira, A. (2013). TanDEM-X: A radar interferometer with two formation-flying satellites. *Acta Astronautica*, 89:83–98.
- Kudryavtsev, V., Akimov, D., Johannessen, J., and Chapron, B. (2005). On radar imaging of current features: 1. Model and comparison with observations. *Journal of Geophysical Research: Oceans*, 110(C7).
- Kudryavtsev, V., Monzikova, A., Combot, C., Chapron, B., and Reul, N. (2019a). A Simplified Model for the Baroclinic and Barotropic Ocean Response to Moving Tropical Cyclones: 2. Model and Simulations. *Journal of Geophysical Research: Oceans*, 0(0).
- Kudryavtsev, V., Monzikova, A., Combot, C., Chapron, B., Reul, N., and Quilfen, Y. (2019b). A Simplified Model for the Baroclinic and Barotropic Ocean Response to Moving Tropical Cyclones: 1. Satellite Observations. *Journal of Geophysical Research: Oceans*, 124(5):3446–3461.
- Kudryavtsev, V., Myasoedov, A., Chapron, B., Johannessen, J. A., and Collard, F. (2012a). Imaging mesoscale upper ocean dynamics using synthetic aperture radar and optical data. *Journal of Geophysical Research: Oceans*, 117(C4).
- Kudryavtsev, V., Myasoedov, A., Chapron, B., Johannessen, J. A., and Collard, F. (2012b). Joint sun-glitter and radar imagery of surface slicks. *Remote Sensing of Environment*, 120:123–132.

- Kwok, R., Cunningham, G. F., and Hibler, W. D. (2003). Sub-daily sea ice motion and deformation from RADARSAT observations. *Geophysical Research Letters*.
- Kwok, R., Schweiger, A., Rothrock, D. A., Pang, S., and Kottmeier, C. (1998). Sea ice motion from satellite passive microwave imagery assessed with ERS SAR and buoy motions. *Journal of Geophysical Research: Oceans*.
- Lavergne, T., Eastwood, S., Teffah, Z., Schyberg, H., and Breivik, L.-A. (2010). Sea ice motion from low-resolution satellite sensors: An alternative method and its validation in the Arctic. *Journal of Geophysical Research: Oceans*, 115(C10):C10032.
- Le Quéré, C., Andrew, R. M., Friedlingstein, P., Sitch, S., Hauck, J., Pongratz, J., Pickers, P. A., Korsbakken, J. I., Peters, G. P., Canadell, J. G., Arneeth, A., Arora, V. K., Barbero, L., Bastos, A., Bopp, L., Chevallier, F., Chini, L. P., Ciais, P., Doney, S. C., Gkritzalis, T., Goll, D. S., Harris, I., Haverd, V., Hoffman, F. M., Hoppema, M., Houghton, R. A., Hurtt, G., Ilyina, T., Jain, A. K., Johannessen, T., Jones, C. D., Kato, E., Keeling, R. F., Goldewijk, K. K., Landschützer, P., Lefèvre, N., Lienert, S., Liu, Z., Lombardozzi, D., Metzl, N., Munro, D. R., Nabel, J. E. M. S., Nakaoka, S.-i., Neill, C., Olsen, A., Ono, T., Patra, P., Peregon, A., Peters, W., Peylin, P., Pfeil, B., Pierrot, D., Poulter, B., Rehder, G., Resplandy, L., Robertson, E., Rocher, M., Rödenbeck, C., Schuster, U., Schwinger, J., Séférian, R., Skjelvan, I., Steinhoff, T., Sutton, A., Tans, P. P., Tian, H., Tilbrook, B., Tubiello, F. N., van der Laan-Luijkx, I. T., van der Werf, G. R., Viovy, N., Walker, A. P., Wiltshire, A. J., Wright, R., Zaehle, S., and Zheng, B. (2018). Global Carbon Budget 2018. *Earth System Science Data*, 10(4):2141–2194. Number: 4.
- Lee, J.-S., Hoppel, K., Mango, S., and Miller, A. (1994). Intensity and phase statistics of multilook polarimetric and interferometric SAR imagery. *IEEE Transactions on Geoscience and Remote Sensing*, 32(5):1017–1028.
- Lévy, M., Franks, P. J. S., and Smith, K. S. (2018). The role of submesoscale currents in structuring marine ecosystems. *Nature Communications*, 9(1):4758.
- Li, H., Chapron, B., Mouche, A., and Stopa, J. E. (2019). A New Ocean SAR Cross-Spectral Parameter: Definition and Directional Property Using the Global Sentinel-1 Measurements. *Journal of Geophysical Research: Oceans*, 124(3):1566–1577.
- Liang, J.-H., D’Asaro, E. A., McNeil, C. L., Fan, Y., Harcourt, R. R., Emerson, S. R., Yang, B., and Sullivan, P. P. (2020). Suppression of CO₂ Outgassing by Gas Bubbles Under a Hurricane. *Geophysical Research Letters*, 47(18):e2020GL090249. _eprint: <https://agupubs.onlinelibrary.wiley.com/doi/pdf/10.1029/2020GL090249>.
- Lodise, J., Özgökmen, T., Gonçalves, R. C., Iskandarani, M., Lund, B., Horstmann, J., Poulain, P.-M., Klymak, J., Ryan, E. H., and Guigand, C. (2020). Investigating the Formation of Submesoscale Structures along Mesoscale Fronts and Estimating Kinematic Quantities Using Lagrangian Drifters. *Fluids*, 5(3):159. Number: 3 Publisher: Multidisciplinary Digital Publishing Institute.
- Lu, Z., Wang, G., and Shang, X. (2020). Strength and Spatial Structure of the Perturbation Induced by a Tropical Cyclone to the Underlying Eddies. *Journal of Geophysical Research: Oceans*, 125(5):e2020JC016097. _eprint: <https://agupubs.onlinelibrary.wiley.com/doi/pdf/10.1029/2020JC016097>.

- Lundgren, P., Nikkhoo, M., Samsonov, S. V., Milillo, P., Gil-Cruz, F., and Lazo, J. (2017). Source model for the Copahue volcano magma plumbing system constrained by InSAR surface deformation observations. *Journal of Geophysical Research: Solid Earth*, 122(7):5729–5747.
- Ma, Z., Fei, J., Lin, Y., and Huang, X. (2020). Modulation of clouds and rainfall by tropical cyclone's cold wakes. *GRL*, 47.
- Magnússon, E., Björnsson, H., Rott, H., and Pálsson, F. (2010). Reduced glacier sliding caused by persistent drainage from a subglacial lake. *Cryosphere*.
- Magnússon, E., Rott, H., Björnsson, H., and Pálsson, F. (2007). The impact of jökulhlaups on basal sliding observed by SAR interferometry on Vatnajökull, Iceland. *Journal of Glaciology*.
- Marzeion, B., Cogley, J. G., Richter, K., and Parkes, D. (2014). Glaciers. Attribution of global glacier mass loss to anthropogenic and natural causes. *Science (New York, N.Y.)*.
- Marzeion, B., Kaser, G., Maussion, F., and Champollion, N. (2018). Limited influence of climate change mitigation on short-term glacier mass loss. *Nature Climate Change*.
- Mastin, L. G., Lisowski, M., Roeloffs, E., and Beeler, N. (2009). Improved constraints on the estimated size and volatile content of the Mount St. Helens magma system from the 2004–2008 history of dome growth and deformation. *Geophysical Research Letters*, 36(20):L20304.
- Mayer, C., Schaffer, J., Hattermann, T., Floricioiu, D., Krieger, L., Dodd, P. A., Kanzow, T., Licciulli, C., and Schannwell, C. (2018). Large ice loss variability at Nioghalvfjærdsfjorden Glacier, Northeast-Greenland. *Nature Communications*, 9(1):1–11.
- McMillan, M., Shepherd, A., Sundal, A., Briggs, K., Muir, A., Ridout, A., Hogg, A., and Wingham, D. (2014). Increased ice losses from Antarctica detected by CryoSat-2. *Geophysical Research Letters*.
- Mei, W. and Pasquero, C. (2012). Restratification of the Upper Ocean after the Passage of a Tropical Cyclone: A Numerical Study. *Journal of Physical Oceanography*, 42(9):1377–1401. Publisher: American Meteorological Society.
- Mei, W. and Pasquero, C. (2013a). Spatial and temporal characterization of sea surface temperature response to tropical cyclones. *Journal of Climate*, 26(11):3745–3765.
- Mei, W. and Pasquero, C. (2013b). Spatial and Temporal Characterization of Sea Surface Temperature Response to Tropical Cyclones. *Journal of Climate*, 26(11):3745–3765. Publisher: American Meteorological Society.
- Mei, W., Primeau, F., McWilliams, J. C., and Pasquero, C. (2013). Sea surface height evidence for long-term warming effects of tropical cyclones on the ocean. *Proceedings of the National Academy of Sciences*, 110(38):15207–15210.
- Meroni, A. N., Giurato, M., Ragone, F., and Pasquero, C. (2020). Observational evidence of the preferential occurrence of wind convergence over sea surface temperature fronts in the Mediterranean. *Quarterly Journal of the Royal Meteorological Society*, 146(728):1443–1458. [_eprint: https://rmets.onlinelibrary.org/doi/10.1002/qj.3844](https://rmets.onlinelibrary.org/doi/10.1002/qj.3844)

rary.wiley.com/doi/pdf/10.1002/qj.3745.

- Meroni, A. N., Miller, M. D., Tziperman, E., and Pasquero, C. (2017). Nonlinear Energy Transfer among Ocean Internal Waves in the Wake of a Moving Cyclone. *Journal of Physical Oceanography*, 47(8):1961–1980. Publisher: American Meteorological Society.
- Mogensen, K. S., Magnusson, L., and Bidlot, J.-R. (2017). Tropical cyclone sensitivity to ocean coupling. *ECMWF Technical Memoranda*, (794):1–51. ECMWF, Shinfield Park, Reading, UK.
- Moiseev, A., Johnsen, H., Johannessen, J. A., Collard, F., and Guitton, G. (2020). On Removal of Sea State Contribution to Sentinel-1 Doppler Shift for Retrieving Reliable Ocean Surface Current. *Journal of Geophysical Research: Oceans*, 125(9):e2020JC016288. [_eprint: https://agupubs.onlinelibrary.wiley.com/doi/pdf/10.1029/2020JC016288](https://agupubs.onlinelibrary.wiley.com/doi/pdf/10.1029/2020JC016288).
- Montgomery, M. and Smith, R. (2014). Paradigms for tropical cyclone intensification. *Australian Meteorological and Oceanographic Journal*, 64(1):37–66.
- Monti Guarnieri, A. and Tebaldini, S. (2008). On the Exploitation of Target Statistics for SAR Interferometry Applications. *IEEE Transactions on Geoscience and Remote Sensing*, 46(11):3436–3443.
- Mora, O., Mallorqui, J. J., and Broquetas, A. (2003). Linear and nonlinear terrain deformation maps from a reduced set of interferometric SAR images. *IEEE Transactions on Geoscience and Remote Sensing*, 41(10):2243–2253.
- Moroney, C., Davies, R., and Muller, J. (2002). Operational retrieval of cloud-top heights using MISR data. *IEEE Transactions on Geoscience and Remote Sensing*, 40(7):1532–1540. Conference Name: IEEE Transactions on Geoscience and Remote Sensing.
- Morrow, R., Fu, L.-L., Arduin, F., Benkiran, M., Chapron, B., Cosme, E., d’Ovidio, F., Farrar, J. T., Gille, S. T., Lapeyre, G., Le Traon, P.-Y., Pascual, A., Ponte, A., Qiu, B., Raschle, N., Ubelmann, C., Wang, J., and Zaron, E. D. (2019). Global Observations of Fine-Scale Ocean Surface Topography With the Surface Water and Ocean Topography (SWOT) Mission. *Frontiers in Marine Science*, 6. Publisher: Frontiers.
- Mouche, A. A., Chapron, B., Zhang, B., and Husson, R. (2017). Combined Co- and Cross-Polarized SAR Measurements Under Extreme Wind Conditions. *IEEE Transactions on Geoscience and Remote Sensing*, 55(12):6746–6755. Conference Name: IEEE Transactions on Geoscience and Remote Sensing.
- Mouche, A. A., Collard, F., Chapron, B., Dagestad, K., Guitton, G., Johannessen, J. A., Kerbaol, V., and Hansen, M. W. (2012). On the Use of Doppler Shift for Sea Surface Wind Retrieval From SAR. *IEEE Transactions on Geoscience and Remote Sensing*, 50(7):2901–2909. Conference Name: IEEE Transactions on Geoscience and Remote Sensing.
- Mouginot, J., Rignot, E., Bjørk, A. A., van den Broeke, M., Millan, R., Morlighem, M., Noël, B., Scheuchl, B., and Wood, M. (2019a). Forty-six years of Greenland Ice Sheet mass balance from 1972 to 2018. *Proceedings of the National Academy of Sciences of the United States of America*.
- Mouginot, J., Rignot, E., and Scheuchl, B. (2019b). Continent-Wide, Interferometric SAR

Phase, Mapping of Antarctic Ice Velocity. *Geophysical Research Letters*.

- Muller, J., Mandanayake, A., Moroney, C., Davies, R., Diner, D. J., and Paradise, S. (2002). MISR stereoscopic image matchers: techniques and results. *IEEE Transactions on Geoscience and Remote Sensing*, 40(7):1547–1559. Conference Name: IEEE Transactions on Geoscience and Remote Sensing.
- Muller, J.-P., Denis, M.-A., Dundas, R. D., Mitchell, K. L., Naud, C., and Mannstein, H. (2007). Stereo cloud top heights and cloud fraction retrieval from ATSR-2. *International Journal of Remote Sensing*, 28(9):1921–1938. Publisher: Taylor & Francis _eprint: <https://doi.org/10.1080/01431160601030975>.
- Nardelli, B. B. (2013). Vortex waves and vertical motion in a mesoscale cyclonic eddy. *Journal of Geophysical Research: Oceans*, 118(10):5609–5624. _eprint: <https://agupubs.onlinelibrary.wiley.com/doi/pdf/10.1002/jgrc.20345>.
- Nurser, A. and Bacon, S. (2014). The rossby radius in the arctic ocean. *Ocean Science*, 10(6):967–975.
- Oerder, V., Colas, F., Echevin, V., Masson, S., and Lemarié, F. (2018). Impacts of the Mesoscale Ocean-Atmosphere Coupling on the Peru-Chile Ocean Dynamics: The Current-Induced Wind Stress Modulation. *Journal of Geophysical Research: Oceans*, 123(2):812–833. _eprint: <https://agupubs.onlinelibrary.wiley.com/doi/pdf/10.1002/2017JC013294>.
- Okada, Y., Nakamura, S., Iribe, K., Yokota, Y., Tsuji, M., Tsuchida, M., Hariu, K., Kankaku, Y., Suzuki, S., Osawa, Y., and Shimada, M. (2013). System design of wide swath, high resolution, full polarimetric L-band SAR onboard ALOS-2. In *Geoscience and Remote Sensing Symposium (IGARSS), 2013 IEEE International*, pages 2408–2411.
- Palmer, T. and Stevens, B. (2019). The scientific challenge of understanding and estimating climate change. *Proceedings of the National Academy of Sciences*, 116(49):24390–24395.
- Pasquero, C. and Emanuel, K. (2008). Tropical Cyclones and Transient Upper-Ocean Warming. *Journal of Climate*, 21(1):149–162. Publisher: American Meteorological Society.
- Pilo, G. S., Oke, P. R., Coleman, R., Rykova, T., and Ridgway, K. (2018). Patterns of Vertical Velocity Induced by Eddy Distortion in an Ocean Model. *Journal of Geophysical Research: Oceans*, 123(3):2274–2292. _eprint: <https://agupubs.onlinelibrary.wiley.com/doi/pdf/10.1002/2017JC013298>.
- Prats-Iraola, P., Lopez-Dekker, P., De Zan, M., Yague-Martinez, N., Zonno, M., and Rodriguez-Cassola, M. (2018). Performance of 3-D Surface Deformation Estimation for Simultaneous Squinted SAR Acquisitions. *IEEE Transactions on Geoscience and Remote Sensing*, pages 1–12.
- Prats-Iraola, P., Scheiber, R., Marotti, L., Wollstadt, S., and Reigber, A. (2012). TOPS interferometry with TerraSAR-X. *IEEE Transactions on Geoscience and Remote Sensing*, 50(8):3179–3188.
- Price, J. (1981). Upper ocean response to a hurricane. *Journal of Physical Oceanography*, 11:153–175.

- Price, J., Morzel, J., and Niiler, P. (2008). Warming of sst in the cool wake of a moving hurricane. *J. Geophys. Res.*, 113(c7):C07010.
- Rampal, P., Bouillon, S., Ólason, E., and Morlighem, M. (2016). neXtSIM: a new Lagrangian sea ice model. *The Cryosphere*, 10(3):1055–1073.
- Rankl, M. and Braun, M. (2016). Glacier elevation and mass changes over the central Karakoram region estimated from TanDEM-X and SRTM/X-SAR digital elevation models. *Annals of Glaciology*, 57(71):273–281.
- Rascle, N., Chapron, B., Molemaker, J., Nougulier, F., Ocampo-Torres, F. J., Cañedo, J. P. O., Marié, L., Lund, B., and Horstmann, J. (2020). Monitoring Intense Oceanic Fronts Using Sea Surface Roughness: Satellite, Airplane, and In Situ Comparison. *Journal of Geophysical Research: Oceans*, 125(8):e2019JC015704. _eprint: <https://agupubs.onlinelibrary.wiley.com/doi/pdf/10.1029/2019JC015704>.
- Rascle, N., Molemaker, J., Marié, L., Nougulier, F., Chapron, B., Lund, B., and Mouche, A. (2017). Intense deformation field at oceanic front inferred from directional sea surface roughness observations. *Geophysical Research Letters*, 44(11):2017GL073473.
- Rast, M. and Kern (2015). ESA’s Living Planet Programme: Scientific Achievements and Future Challenges – Scientific Context of the Earth Observation Science Strategy for ESA. Technical Report ESA SP-1329/2, ESA Communications.
- Reichstein, M., Camps-Valls, G., Stevens, B., Jung, M., Denzler, J., Carvalhais, N., and Prabhat (2019). Deep learning and process understanding for data-driven Earth system science. *Nature*, 566(7743):195–204. Number: 7743 Publisher: Nature Publishing Group.
- Renault, L., McWilliams, J. C., and Masson, S. (2017). Satellite Observations of Imprint of Oceanic Current on Wind Stress by Air-Sea Coupling. *Scientific Reports*, 7(1):17747. Number: 1 Publisher: Nature Publishing Group.
- Renault, L., Molemaker, M. J., McWilliams, J. C., Shchepetkin, A. F., Lemarié, F., Chelton, D., Illig, S., and Hall, A. (2016a). Modulation of wind work by oceanic current interaction with the atmosphere. *Journal of Physical Oceanography*, 46(6):1685–1704.
- Renault, L., Molemaker, M. J., McWilliams, J. C., Shchepetkin, A. F., Lemarié, F., Chelton, D., Illig, S., and Hall, A. (2016b). Modulation of Wind Work by Oceanic Current Interaction with the Atmosphere. *Journal of Physical Oceanography*, 46(6):1685–1704. Publisher: American Meteorological Society.
- Renfrew, I. A. and Moore, G. W. K. (1999). An Extreme Cold-Air Outbreak over the Labrador Sea: Roll Vortices and Air–Sea Interaction. *Monthly Weather Review*, 127(10):2379–2394. Publisher: American Meteorological Society.
- Rignot, E., Mouginot, J., Scheuchl, B., Van Den Broeke, M., Van Wessem, M. J., and Morlighem, M. (2019). Four decades of Antarctic ice sheet mass balance from 1979–2017. *Proceedings of the National Academy of Sciences of the United States of America*.
- Rino, C. L. (1979). A power law phase screen model for ionospheric scintillation. I - Weak scatter. II - Strong scatter. *Radio Science*, 14:1135–1145.
- Robertson, J. E. and Watson, A. J. (1992). Thermal skin effect of the surface ocean and its

- implications for CO₂ uptake. *Nature*, 358(6389):738–740. Number: 6389 Publisher: Nature Publishing Group.
- Rodríguez, E., Bourassa, M., Chelton, D., Farrar, J. T., Long, D., Perkovic-Martin, D., and Samelson, R. (2019). The Winds and Currents Mission Concept. *Frontiers in Marine Science*, 6. Publisher: Frontiers.
- Romanovsky, V. E., Smith, S. L., and Christiansen, H. H. (2010). Permafrost thermal state in the polar northern hemisphere during the international polar year 2007-2009: A synthesis. *Permafrost and Periglacial Processes*.
- Romero, L., Hypolite, D., and McWilliams, J. C. (2020). Submesoscale current effects on surface waves. *Ocean Modelling*, 153:101662.
- Rosen, P. A., Kim, Y., Hensley, S., Shaffer, S., Veilleux, L., Hoffman, J., Chuang, C.-L., Chakraborty, M., Sagi, V., Satish, R., Putrevu, D., and Bhan, R. (2014). An L- and S-band SAR Mission Concept for Earth Science and Applications. In *EUSAR 2014; 10th European Conference on Synthetic Aperture Radar; Proceedings of*, pages 1–4.
- Rott, H., Abdel Jaber, W., Wuite, J., Scheiblauer, S., Floricioiu, D., Wessem, J. M. v., Nagler, T., Miranda, N., and Broeke, M. R. v. d. (2018). Changing pattern of ice flow and mass balance for glaciers discharging into the Larsen A and B embayments, Antarctic Peninsula, 2011 to 2016. *The Cryosphere*, 12(4):1273–1291.
- Rott, H., Scheiblauer, S., Wuite, J., Krieger, G., Floricioiu, D., Rizzoli, P., Libert, L., and Nagler, T. (2020). Penetration of Interferometric Radar Signals in Antarctic Snow. To be submitted to.
- Sanford, T. B., Price, J. F., Girton, J. B., and Webb, D. C. (2007). Highly resolved observations and simulations of the ocean response to a hurricane. *Geophysical Research Letters*, 34(13). [_eprint: https://agupubs.onlinelibrary.wiley.com/doi/pdf/10.1029/2007GL029679](https://agupubs.onlinelibrary.wiley.com/doi/pdf/10.1029/2007GL029679).
- Schneider, T., Lan, S., Stuart, A., and Teixeira, J. (2017). Earth System Modeling 2.0: A Blueprint for Models That Learn From Observations and Targeted High-Resolution Simulations. *Geophysical Research Letters*, 44(24):12,396–12,417.
- Schuur, E. A., McGuire, A. D., Schädel, C., Grosse, G., Harden, J. W., Hayes, D. J., Hugelius, G., Koven, C. D., Kuhry, P., Lawrence, D. M., Natali, S. M., Olefeldt, D., Romanovsky, V. E., Schaefer, K., Turetsky, M. R., Treat, C. C., and Vonk, J. E. (2015). Climate change and the permafrost carbon feedback.
- Seo, H. (2017). Distinct Influence of Air–Sea Interactions Mediated by Mesoscale Sea Surface Temperature and Surface Current in the Arabian Sea. *Journal of Climate*, 30(20):8061–8080. Publisher: American Meteorological Society.
- Shepherd, A., Ivins, E., Rignot, E., Smith, B., van den Broeke, M., Velicogna, I., Whitehouse, P., Briggs, K., Joughin, I., Krinner, G., Nowicki, S., Payne, T., Scambos, T., Schlegel, N., A. G., Agosta, C., Ahlstrøm, A., Babonis, G., Barletta, V. R., Bjørk, A. A., Blazquez, A., Bonin, J., Colgan, W., Csatho, B., Cullather, R., Engdahl, M. E., Felikson, D., Fettweis, X., Forsberg, R., Hogg, A. E., Gallee, H., Gardner, A., Gilbert, L., Gourmelen, N., Groh, A., Gunter, B., Hanna, E., Harig, C., Helm, V., Horvath, A., Horwath, M., Khan, S., Kjeldsen, K. K.,

- Konrad, H., Langen, P. L., Lecavalier, B., Loomis, B., Luthcke, S., McMillan, M., Melini, D., Mernild, S., Mohajerani, Y., Moore, P., Mottram, R., Mougnot, J., Moyano, G., Muir, A., Nagler, T., Niell, G., Nilsson, J., Noël, B., Ootosaka, I., Pattle, M. E., Peltier, W. R., Pie, N., Rietbroek, R., Rott, H., Sandberg Sørensen, L., Sasgen, I., Save, H., Scheuchl, B., Schrama, E., Schröder, L., Seo, K.-W., Simonsen, S. B., Slater, T., Spada, G., Sutterley, T., Talpe, M., Tarasov, L., van de Berg, W. J., van der Wal, W., van Wessem, M., Vishwakarma, B. D., Wiese, D., Wilton, D., Wagner, T., Wouters, B., Wuite, J., and The IMBIE Team (2020). Mass balance of the Greenland Ice Sheet from 1992 to 2018. *Nature*, 579(7798):233–239. Number: 7798 Publisher: Nature Publishing Group.
- Shepherd, A., Ivins, E., Rignot, E., Smith, B., van den Broeke, M., Velicogna, I., Whitehouse, P., Briggs, K., Joughin, I., Krinner, G., Nowicki, S., Payne, T., Scambos, T., Schlegel, N., Geruo, A., Agosta, C., Ahlstrom, A., Bobonis, G., Barletta, v., Blazquez, A., Bonin, J., Csatho, B., Cullather, R., Felikson, D., Fettweis, X., Forsberg, R., Gallee, H., Gardner, A., Gilbert, L., Groh, A., Gunter, B., Hanna, E., Harig, C., Helm, V., Horvath, A., Horwath, M., Khan, S., Kjeldsen, K. K., Konrad, H., Langen, P., Lecavalier, B., Loomis, B., Luthcke, S., McMillan, M., Melini, D., Mernild, S., Mohajerani, Y., Moore, P., Mougnot, J., Moyano, G., Muir, A., Nagler, T., Niell, G., Nilsson, J., Noel, B., Ootosaka, I., Pattle, M. E., Peltier, W. R., Pie, N., Bietbroek, R., Rott, H., Sandberg-Sorensen, L., Sasgen, I., Save, H., Scheuchl, B., Schrama, E., Schroder, L., Seo, K.-W., Simonsen, S., Slater, T., Spada, G., Sutterley, T., Talpe, M., Tarasov, L., van de Berg, W., van der Wal, W., van Wessem, M., Vishwakarma, B., Wiese, D., and Wouters, B. (2018). Mass balance of the Antarctic Ice Sheet from 1992 to 2017. *Nature*, 558:219–222.
- Siegelman, L., Klein, P., Rivière, P., Thompson, A. F., Torres, H. S., Flexas, M., and Mene-menlis, D. (2020). Enhanced upward heat transport at deep submesoscale ocean fronts. *Nature Geoscience*, 13(1):50–55.
- Smith, B., Fricker, H. A., Gardner, A. S., Medley, B., Nilsson, J., Paolo Nicholas Holschuh, F. S., Adusumilli, S., Brunt, K., Csatho, B., Harbeck, K., Markus, T., Neumann, T., Siegfried, M. R., and Jay Zwally, H. (2020). Pervasive ice sheet mass loss reflects competing ocean and atmosphere processes. *Science*.
- Smith, R. K. and Montgomery, M. T. (2015). Toward Clarity on Understanding Tropical Cyclone Intensification. *Journal of the Atmospheric Sciences*, 72(8):3020–3031. Publisher: American Meteorological Society.
- Smith, S. D. (1988). Coefficients for sea surface wind stress, heat flux, and wind profiles as a function of wind speed and temperature. *Journal of Geophysical Research: Oceans*, 93(C12):15467–15472. _eprint: <https://agupubs.onlinelibrary.wiley.com/doi/pdf/10.1029/JC093iC12p15467>.
- Srifer, R. L., Goes, M., Mann, M. E., and Keller, K. (2010). Climate response to tropical cyclone-induced ocean mixing in an Earth system model of intermediate complexity. *Journal of Geophysical Research: Oceans*, 115(C10). _eprint: <https://agupubs.onlinelibrary.wiley.com/doi/pdf/10.1029/2010JC006106>.
- Stoffelen, A. and Portabella, M. (2006). On Bayesian scatterometer wind inversion. *IEEE Transactions on Geoscience and Remote Sensing*, 44(6):1523–1533.

- Stoffelen, A., e. a. (2017). Scientific developments and the eps-sg scatterometer. *J. Sel. Topics in Appl. Earth Observ. Rem. Sens.*, 10(5):2086–2097.
- Thorndike, A. S. and Colony, R. (1982). Sea ice motion in response to geostrophic winds. *J. Geophys. Res.*, 87:5845–52.
- Trenberth, K. E. and Stepaniak, D. P. (2004). The flow of energy through the earth's climate system. *Quarterly Journal of the Royal Meteorological Society*, 130(603):2677–2701.
_eprint: <https://rmets.onlinelibrary.wiley.com/doi/pdf/10.1256/qj.04.83>.
- Trindade, A., Portabella, M., Stoffelen, A., Lin, W., and Verhoef, A. (2020). Erastar: A high-resolution ocean forcing product. *IEEE Trans. Geosc. Rem. Sens.*, 58(2):1337–1347.
- Tschudi, M. A., Meier, W. N., and Scott Stewart, J. (2020). An enhancement to sea ice motion and age products at the National Snow and Ice Data Center (NSIDC). *Cryosphere*.
- van Zadelhoff, G.-J., Stoffelen, A., Vachon, P. W., Wolfe, J., Horstmann, J., and Belmonte Rivas, M. (2014). Retrieving hurricane wind speeds using cross-polarization C-band measurements. *Atmospheric Measurement Techniques*, 7(2):437–449.
- Vihma, T. (2014). Effects of Arctic Sea Ice Decline on Weather and Climate: A Review. *Surveys in Geophysics*, 35(5):1175–1214.
- Voors, R., Donovan, D., Acarreta, J., Eisinger, M., Franco, R., Lajas, D., Moyano, R., Pirondini, F., Ramos, J., and Wehr, T. (2007). ECSIM: the simulator framework for EarthCARE. In *Sensors, Systems, and Next-Generation Satellites XI*, volume 6744, page 67441Y. International Society for Optics and Photonics.
- Wang, C., Mouche, A., Tandeo, P., Stopa, J., Longépé, N., Erhard, G., Foster, R., Vandemark, D., and Chapron, B. (2018). Labeled SAR imagery dataset of ten geophysical phenomena from Sentinel-1 wave mode (TenGeoP-SARwv). type: dataset.
- Wang, C., Mouche, A., Tandeo, P., Stopa, J. E., Longépé, N., Erhard, G., Foster, R. C., Vandemark, D., and Chapron, B. (2019). A labelled ocean SAR imagery dataset of ten geophysical phenomena from Sentinel-1 wave mode. *Geoscience Data Journal*, 0(0).
- Watson, A. J., Schuster, U., Shutler, J. D., Holding, T., Ashton, I. G. C., Landschützer, P., Woolf, D. K., and Goddijn-Murphy, L. (2020). Revised estimates of ocean-atmosphere CO₂ flux are consistent with ocean carbon inventory. *Nature Communications*, 11(1):4422. Number: 1 Publisher: Nature Publishing Group.
- Wendt, A., Mayer, C., Lambrecht, A., and Floricioiu, D. (2017). A Glacier Surge of Bivachny Glacier, Pamir Mountains, Observed by a Time Series of High-Resolution Digital Elevation Models and Glacier Velocities. *Remote Sensing*, 9(4):388.
- Wicks, C., de la Llera, J. C., Lara, L. E., and Lowenstern, J. (2011). The role of dyking and fault control in the rapid onset of eruption at Chaitén volcano, Chile. *Nature*, 478(7369):374–377.
- Wineteer, A., Perkovic-Martin, D., Monje, R., Rodríguez, E., Gál, T., Niamsuwan, N., Nicaise, F., Srinivasan, K., Baldi, C., Majurec, N., and Stiles, B. (2020). Measuring Winds and Currents with Ka-Band Doppler Scatterometry: An Airborne Implementation and Progress towards a Spaceborne Mission. *Remote Sensing*, 12(6):1021. Number: 6 Publisher: Mul-

tidisciplinary Digital Publishing Institute.

- Woolf, D. K. (1997). Bubbles and their role in gas exchange. *The Sea Surface and Global Change*, pages 173–206. Publisher: Cambridge University Press.
- Xu, Y. and Scott, R. B. (2008). Subtleties in forcing eddy resolving ocean models with satellite wind data. *Ocean Modelling*, 20(3):240–251.
- Yagüe-Martínez, N., Prats-Iraola, P., Rodríguez González, F., Brcic, R., Shau, R., Geudtner, D., Eineder, M., and Bamler, R. (2016). Interferometric processing of sentinel-1 tops data. *IEEE Transactions on Geoscience and Remote Sensing*, 54(4):2220–2234.
- Young, G. S., Sikora, T. D., and Winstead, N. S. (2000). Inferring Marine Atmospheric Boundary Layer Properties from Spectral Characteristics of Satellite-Borne SAR Imagery. *MONTHLY WEATHER REVIEW*, 128:15.
- Yu, L. (2019). Global Air–Sea Fluxes of Heat, Fresh Water, and Momentum: Energy Budget Closure and Unanswered Questions. *Annual Review of Marine Science*, 11(1):227–248.
- Zemp, M., Huss, M., Thibert, E., Eckert, N., McNabb, R., Huber, J., Barandun, M., Machguth, H., Nussbaumer, S. U., Gärtner-Roer, I., Thomson, L., Paul, F., Maussion, F., Kutuzov, S., and Cogley, J. G. (2019). Global glacier mass changes and their contributions to sea-level rise from 1961 to 2016. *Nature*, 568(7752):382–386. Number: 7752 Publisher: Nature Publishing Group.
- Zhang, Y., Zhang, Z., Chen, D., Qiu, B., and Wang, W. (2020). Strengthening of the Kuroshio current by intensifying tropical cyclones. *Science*, 368(6494):988–993. Publisher: American Association for the Advancement of Science Section: Research Article.

ACRONYMS

AASR	Azimuth Ambiguity to Signal Ratio
ACT	Across-Track
ATI	Along-Track Interferometry
CD	Cloud Detection band
CE	Central Electronics
CFRP	Carbon Fibre Reinforced Polymer
CMV	Cloud Motion Vectors
COV	Covariance matrices of normalized radar scattering coefficients
CTH	Cloud Top Height
DCA	Doppler Centroid Anomaly
DTAR	Distributed Total Ambiguity Ratio
DTE	Digital Twin Earth
DSM	Digital Surface Model
DTAR	Distributed Total Ambiguity Ratio
EC	European Commission
ECMWF	European Centre for Medium-Range Weather Forecasts
EE-10	Earth Explorer 10
EFM	Electrical and Functional Model
EM	Engineering Model
EO	Earth Observation
EOL	End of Life
ESA	European Space Agency
ETC	Extra Tropical Cyclone
EW	Sentinel-1 Extra Wide swath mode
FE	Front End
FEE	Front End Electronics
FM	Flight Model
FOCC	Flight Operations Control Centre
FOS	Flight Operation Segment
FPA	Focal Plane Assembly
FPGA	Field Programmable Gate Array

FWHM	Full Width at Half Maximum
GNSS	Global Navigation Satellite System
G/S	Ground Segment
H1	Harmony-1
H2	Harmony-2
HDRM	Hold-down and Release Mechanism
HoA	Height of Ambiguity
HRM	Hold-down and Release Mechanism
ICS	Image Cross Spectra
InSAR	Interferometric Synthetic Aperture Radar
ISP	Instrument Source Packets
ITU	International Telecommunication Union
IW	Sentinel-1 Interferometric Wide swath mode
LA	Laser Altimeter
L0	Level-0
L1	Level-1
L2	Level-2
L2	Level-3
LEO	Low Earth Orbit
LEOP	Launch and Early Orbit Phase
LES	Large Eddy Simulation
LO	Local Oscillator
LoS	Line of Sight
LSTM	Copernicus Land Surface Temperature Monitoring mission
MABL	Marine Atmospheric Boundary Layer
MATER	Mission and Technical Requirements Document
MGA	Medium gain Antenna
MISR	Multi-angle Imaging spectroradiometer
MIZ	Marginal Ice Zone
MLI	Multi-Layer Insulation
ML	Mixed Layer
MRD	Mission Requirements Document

NEdT	Noise Equivalent delta Temperature
NESZ	Noise Equivalent Sigma Zero
NORCE	Norwegian Research Centre
NRCS	Normalised Radar Cross-Section
OCN	Sentinel-1 Level-2 Ocean
OCS	Orbit Control System
OLE	Organized Large Eddy
OSW	Ocean Swell Wave spectra
OWI	Ocean surface WInd field
OWS	Ocean Wave Spectra
PAN	Panchromatic band
PDGS	Payload Data Ground Segment
PDHT	Payload Data Handling and Transmission
PL	Polar Low
POD	Precise Orbit Determination
PFM	Proto-Flight Model
PRF	Pulse Repetition Frequency
PSF	Point Spread Function
QM	Qualification Model
RA	Radar Altimeter
RCS	Reaction Control System
RF	Radio-Frequency
RI	Rapid Intensification
RMSD	Root Mean Square Deviation
RoI	Region of Interest
RPE	Relative Performance Error
RPE	Relative Performance Error
RPI	Repeat Pass Interferometry
RRN	Routing and Redundancy Network
RVL	Radial Velocity
SADM	Solar Array Drive Mechanism
S1	Sentinel-1

S1-A	Sentinel-1A
S1-B	Sentinel-1B
S1-C	Sentinel-1C
S1-D	Sentinel-1D
S1-NG	next generation of Sentinel-1 satellites
SA	Solar Array
SAR	Synthetic Aperture Radar
SAS	SAR Antenna Subsystem
SCV	(Total) Surface Current Velocity vectors
SES	SAR Electronic Subsystem
σ_0	See NRCS
SLC	Single Look Complex SAR image
SM	Structural Model
SSA	Small Slope Approximation
STM	Structural and Thermal Model
SNR	Signal to Noise Ratio
SPI	Single Pass Interferometry
SSO	Sun Synchronous Orbit
SST	Sea Surface Temperature
SSV	Surface Stress Vectors
SWV	Surface Wind Vectors
TAR	Top of Atmosphere Radiances
TC	Tropical Cyclone
TDI	Time Delay and Integration
TDV	3D Velocity Vectors
TED	Thermo-Elastic Distortion
TIR	Thermal Infra-Red
TOC	Topography Changes
TOPS	Terrain Observation by Progressive Scans
TRL	Technology Readiness Level
TSC	Total Surface Current
TSCV	Total Surface Current Vector



TT&C	Telemetry Tracking and Command
TWTA	Travelling Wave Tube Amplifier
UPM	Universal Processing module
USO	Ultra Stable Oscillator
USV	Geophysically equivalent surface velocities
VCM	Variable Coding and Modulation
VNIR	Visual and Near Infrared
WSOA	Wide Swath Ocean Altimeter
WV	Sentinel-1 Wave mode
XTI	Across-Track Interferometry
InSAR	Interferometric synthetic aperture radar
N-S	North-south
3-D	Three-dimensional